Analysis and Control of Subsynchronous Resonance in the Presence of Thyristor Controlled Series Compensation

by:

KHOSRO KABIRI

B.Sc., Sharif University of Technology, Tehran, 1995
M.Sc., Sharif University of Technology, Tehran, 1998

A THESIS SUBMITTED IN PARTIAL FULFILLMENT OF
THE REQUIREMENTS FOR THE DEGREE OF

DOCTOR OF PHILOSOPHY

in

THE FACULTY OF GRADUATE STUDIES
(Department of Electrical and Computer Engineering)

We accept this thesis as conforming
to the required standard

.....

.....

.....

.....

The University of British Columbia
May 2004

Abstract

In this thesis, the problem of subsynchronous mechanical oscillations in the shaft assembly of a turbo-generator with its steam turbine stages is studied, when the generator is connected to a Thyristor Controlled Series Capacitor (TCSC) compensated transmission line.

The first three-phase thyristor controlled series capacitor was installed in 1992. The usefulness of this device for mitigating subsynchronous resonance has been established. There are, however, issues remaining to be investigated. A point of contention is the nature of the behaviour of TCSC towards subsynchronous frequencies. Although TCSC does not have resistive components as such, it puts up significant resistance to the subsynchronous current flow when in open-loop operation. This characteristic, known as passive damping, has been observed both on network analyzers and in simulations. Here, with the aid of analytical relations and discrete Fourier analysis, a physical explanation is provided for this behaviour.

The average steady-state linearization, although an efficient method for obtaining linear models for switching circuits, fails to capture the passive damping of TCSC. The Poincaré mapping technique, on the other hand, provides the state matrix of the discrete linear time-invariant system that is equivalent to the linearized time-periodic model of the switching circuit in the sense of Lyapunov. Therefore it is accurate in the eigenvalue analysis for stability studies.

Poincaré mapping together with a perturbation method is used here to find a linearized discrete model for a TCSC compensated system, in which the small signal variation of the state is explicitly given in terms of the small signal variation of the TCSC firing angles. The model is used first for the eigenvalue analysis and then for the design of an all-stabilizing closed-loop controller for small signal control of the thyristor firing angles in order to damp subsynchronous mechanical oscillations.

In the past, Poincaré mapping has been used to derive continuous dynamic models for the TCSC alone, by first finding the discrete advance map, and then by converting the equations to the continuous domain.

Here, we discretize the generator, line and TCSC equations together to arrive at a state space model for the entire system. The First IEEE Subsynchronous Resonance Benchmark Model is our case study. The method is general enough, however, to be used for other configurations as well.

Finally, the steady-state relations of TCSC in non-equidistant firing are developed, and its dynamic behaviour with the new open-loop firing scheme is studied using transient simulation.

Contents

List of Tables

List of Figures

List of Symbols

Uppercase boldface upright letters are used to indicate matrices, for example $\mathbf{A}, \mathbf{B}$. Lowercase boldface upright letters are used to indicate vectors, for example $\mathbf{x}, \mathbf{y}$. Uppercase boldface italic letters indicate phasors, for example $\boldsymbol{V}$. In the following list, the less commonly used variables are referred to the page where they appear in the text.

Scalars & Phasors

α	TCSC firing angle, calculated from the capacitor voltage zero crossing
β	TCSC advance angle
Δ	small signal change
δ	synchronous machine torque angle, Page 88
κ	ratio of the TCSC natural frequency to the synchronous frequency
λ	eigenvalue
μ_0	magnetic constant, $4\pi 10^{-7}$ Hm^{-1}, Page 37
ω	angular frequency
ϕ	turn-on time of a TCSC thyristor
ψ	flux linkage
σ	TCSC conduction angle
τ	turn-off time of a TCSC thyristor
θ	rotor angular position
φ	TCSC deviation angle
a_g	air gap length, Page 37
B	susceptance, the imaginary part of admittance $\boldsymbol{Y} = G + jB$, Page 15
C	capacitor, capacitance
E_k	kinetic energy, Page 43
f	frequency
g_0	gravitation acceleration constant, 9.807 $\mathrm{m/s}^2$, Page 35
H	inertia constant
H	transfer function, Page 86
i	instantaneous current
J	moment of inertia
K	rotational spring constant
k	linear spring constant, Page 35

k_{nom}	nominal degree of line compensation, Page 88
L	inductor, inductance
l	pendulum length, Page 35
ℓ	axial length of the rotor, Page 37
M	mutual inductance
m	mass, Page 35
md	modal damping decrement
N	number of winding turns, Page 37
n	discrete time
p	instantaneous power, Page 56
p	number of machine poles, Page 10
r	radius of the rotor, Page 37
S	apparent power, Page 143
s	Laplace transform variable
T	period, time step
t	continuous time
t_q	torque
v	instantaneous voltage
X	reactance, the imaginary part of impedance $\boldsymbol{Z} = R + jX$
x	linear pendulum position, Page 35
X_1, X_0	positive sequence reactance, zero-sequence reactance
z	z transform variable
$\boldsymbol{Y}$	admittance, Page 15
$\boldsymbol{E}_q$	phasor of the internal EMF, Page 89
$\boldsymbol{I}$	current phasor, Page 88
$\boldsymbol{V}$	voltage phasor, Page 88
$\boldsymbol{V}_\infty$	phasor of the infinite bus voltage, Page 88
$\boldsymbol{Z}$	impedance

Matrices & Vectors

$\boldsymbol{\omega}$	vector of rotor angular speeds
$\boldsymbol{\theta}$	vector of rotor angular positions
$\boldsymbol{\Gamma}$	participation matrix, Page 153
$\boldsymbol{\Phi}$	state transition matrix
$\boldsymbol{\Psi}$	fundamental matrix, Page 25
$\mathbf{A}, \mathbf{B}, \mathbf{C}, \mathbf{D}$	linear system matrices
$\mathbf{D}$	matrix of self dampings, Page 143
$\mathbf{g}$	derivative vector, Page 72
$\mathbf{H}$	matrix of inertia constants
$\mathbf{J}$	Jacobian, Page 76

$\mathbf{J}$	matrix of inertias, Page 49
$\mathbf{K}$	matrix of spring constants
$\mathbf{k}$	feedback controller gain, Page 29
$\mathbf{L}_{Kl}$	Kalman observer gain, Page 31
$\mathbf{L}_{ob}$	observer gain, Page 29
$\mathbf{M}_{Kl}$	Kalman observer innovation gain, Page 31
$\mathbf{P_j}, \mathbf{Q_j}$	projection matrix, injection matrix
$\mathbf{P}, \mathbf{Q}$	Park's transformation matrix, inverse of Park's transformation
$\mathbf{P}_{eq}$	equivalence transformation, Page 24
$\mathbf{P}_{mod}$	modal equivalence transformation, Page 50
$\mathbf{Q_w}$	process noise covariance matrix, Page 31
$\mathbf{R_v}$	measurement noise covariance matrix, Page 31
$\mathbf{t_q}$	vector of torques
$\mathbf{u}$	input vector
$\mathbf{v}$	input or process noise random vector, Page 31
$\mathbf{v}_i$	right eigenvector associated with eigenvalue λ_i, Page 152
$\mathbf{w}$	output or measurement noise random vector, Page 31
$\mathbf{w}_i$	left eigenvector associated with eigenvalue λ_i, Page 152
$\mathbf{x}$	state vector
$\mathbf{x}_z$	a zero or fixed point of a Poincaé map, Page 27
$\mathbf{y}$	output vector
$\mathbf{y}_{ob}$	observer output, Page 31

Subscripts

$0, d, q$	0-axis, d-axis, q-axis
∞	infinite bus, Page 144
a, b, c	phases of a three-phase system
B	Base quantity
c	continuous, Page 86
d	discrete, Page 87
e	electrical, Page 10
eq	equivalence, equivalent, Page 24
F, D	rotor windings along the d-axis
Gen	Generator, Page 103
h	subsynchronous, Page 56
Kl	Kalman, Page 31
$Line$	Line
m	mechanical, Page 10
mod	modal, Page 50
N	Natural, used to indicate natural resonance

n	negative, Page 78
n_m	number of rotating masses, Page 51
Ny	Nyquist, Page 85
ob	observer, Page 31
p	positive, Page 78
Q, G	rotor windings along the q-axis
R	Rotor, Page 144
S	Stator, Page 144
s	synchronous
Sys	System, Page 103
tc	TCSC
$Tran$	Transformer
W_i	Winding i, Page 37

Superscripts

$\breve{\lambda}$	complex conjugate of λ, Page 85
$\mathbf{P}^{-1}$	inverse of $\mathbf{P}$
$\mathbf{P}^t$	transpose of $\mathbf{P}$
$\bar{t}$	steady-state value of t
$\dot{\mathbf{x}}$	time derivative of $\mathbf{x}$
$\hat{\mathbf{x}}$	observation of the state, Page 29
$\mathbf{x}^*(t)$	steady-state waveforms of $\mathbf{x}(t)$
X''	generator subtransient reactance, Page 10

Special Mathematical Symbols

$< p(t) >_T$	Time average of $p(t)$ over a period T, Page 56
$\angle$	angle, Page 37
$\exp(\mathbf{A})$	exponential of $\mathbf{A}$, Page 76
γ	periodic orbit, Page 27
$\hat{\mathbf{x}}(n\|n-1)$	state estimation at n given the measurement at $n-1$, Page 31
$\in$	a member of
$\mathbb{R}$; $\mathbb{R}^{n_x}$; $\mathbb{R}^{n_x \times n_u}$	real numbers; real n_x-space; real $(n_x \times n_u)$-space, Page 12
$\mathcal{H}_\infty$	$\mathcal{H}_\infty$ control, Page 113
$\mathcal{N}(\mathbf{0}, \mathbf{Q_w})$	Normal distribution with mean $\mathbf{0}$ and covariance $\mathbf{Q_w}$, Page 31
$\mid x \mid$	the absolute value of x, Page 25
$\partial\mathbf{x}/\partial t$	partial derivative of $\mathbf{x}$ with respect to t
Σ	a cross section or hypersurface in the n_x space, Page 27
$\triangleq$	equal by definition, Page 20
$\mathbf{diag}(L_0, L_d, L_q)$	diagonal matrix with elements L_0, L_d, and L_q, Page 146
$\text{pdf}(\mathbf{w})$	probability density function of the random vector $\mathbf{w}$, Page 31
$\text{PM}(p_0)$	Poincaré map of the point p_0, Page 27

$\mathrm{Re}\{\boldsymbol{V}\}$	the real part of $\boldsymbol{V}$, Page 61
$\mathbb{1}$	identity matrix
ϑ	a subset of a cross section Σ, Page 27
p_0, p_1	points in the n_x space, Page 27
$t \to \infty$	t approaches infinity, Page 27
$\det(\mathbf{A})$	determinant of $\mathbf{A}$

Acronyms & Abbreviations

ABB	Asea Brown Bovery, Page 9
AC	Alternating Current
BPA	Bonneville Power Administration
DC	Direct Current
EMF	Electromotive Force, Page 88
EMTP	Electromagnetic Transients Program, Page 12
EPRI	Electric Power Research Institute, Page 14
FACTS	Flexible AC Transmission System
FBM	First IEEE Subsynchronous Resonance Benchmark Model
FFT	Fast Fourier Transform, Page 61
IEEE	Institute of Electrical and Electronics Engineers
KVL	Kirchoff's voltage law, Page 39
LTI	Linear Time Invariant
MATLAB	Matrix Laboratory
MOV	Metal Oxide Varistor, Page 14
NETOMAC	Network Torsion Machine Control, Page xvi
NSERC	Natural Sciences and Engineering Council of Canada, Page xvi
ODE	Ordinary Differential Equation, Page 105
SSR	Subsynchronous Resonance
TCSC	Thyristor Controlled Series Capacitor or Compensation
UBC	University of British Columbia
USA	United States of America, Page 18
WAPA	Western Area Power Administration

Acknowledgement

I would like to express my deep gratitude to my supervisors, Prof. Hermann W. Dommel and Prof. José R. Martí. I have learnt so much from both of them. Prof. Dommel's attitude will continue to inspire me throughout my professional career. Prof. Marti's course on the transient simulation of power systems first enabled me to appreciate the intricacies of this interesting field. Dr. Sebastian Henschel made it possible for me to work in Germany with the highly competent network consulting group at Siemens, AG. He was always there to lend a hand with my technical and programming problems. I owe him an apology as well for the many interruptions I gave him.

While in Germany, I enjoyed help from several individuals. I particularly would like to thank Dr. Ronald Völzke and Dr. Olaf Ruhle for help in setting up subsynchronous resonance cases with NETOMAC. Dr. Völzke also provided me with the opportunity to have a meeting with Prof. Stefan Kulig of the Dortmund University. Here, I also have to thank Dr. Gerhard Thumm for fruitful discussions on the passive damping characteristic of TCSC, Dr. Dietmar Retzmann for putting me in contact with Mr. Stephan Weiss and Dr. Johann Jäger for arranging a visit to the Universität Erlangen-Nürnberg.

It has been a wonderful experience for me to know Purang Abolmaesumi and Shahin Sirouspour. My friendship with Purang started at the onset of our efforts to get to a graduate school in North America, and actually it was Purang who introduced me to Prof. Dommel. Fruitful discussions with Shahin have clarified many delicate points on control systems for me.

This work was made possible by funding from the Natural Sciences and Engineering Council of Canada (NSERC) through the "NSERC/BC Hydro Industrial Chair in Advanced Techniques for Power Systems Analysis, Simulation and Control", and by financial assistance from the Power Transmission and Distribution Department of the Siemens, AG in Erlangen, Germany through Mr. Wolfgang Braun.

Many thanks to my friends in the Power Group for their friendship and constant support. The friendly atmosphere in the Power Group has made it an extremely pleasant working environment, where people feel very welcome and there are always hands to reach out to help when needed. While every one of them is dear to me, I would especially like to mention Daniel Lindenmeyer, Mazana Lukic and Awad Ibrahim, the first people on a list that has grown constantly through my years at UBC. My special thanks also go to Prof. Takahide Niimura for his encouragement and support.

No words can express my gratitude to my parents Turan and Mohammad, and to my sister Maryam for their unlimited love and support. I have been blessed to have a family like this.

Finally, I have enjoyed many happy moments over the past few years among my friends in Canada and Germany. Naming them all would make a long list. However, I would especially like to mention Gerlinde, Florian, Shiva, Ahmadreza and Farhad.

Vancouver, B.C., Canada — Khosro Kabiri
May, 2004

Chapter 1

Introduction

Reactive compensation in alternating current electric power systems is used for power factor correction, load balancing, improvement of voltage regulation, and increase of the transfer capacity.

Compensators are generally divided into shunt and series types. Compensation of a load is always shunt, since the compensating device is connected in parallel with the load at the supply point. Compensation of a transmission or distribution system, on the other hand, can be shunt or series.

Compensation becomes necessary when a transmission line is very long. In theory, a lossless line which is a quarter wavelength long is impossible to operate because in open circuit, the receiving end voltage becomes infinity (for the lossy line, the voltage would not be exactly infinity, but still extremely high). Lines are much shorter in practice, yet need to be compensated to improve their voltage regulation.

Series compensation is essentially a set of capacitor banks installed in series with the transmission line. The effective inductive reactance of the line is reduced by the amount of the capacitive reactance of the compensator. Series compensation improves the steady-state, the transient, and the voltage stability of the system. However, it potentially gives rise to a serious instability problem that needs careful study.

The problem occurs in the range of frequencies below the synchronous frequency of the

network, and hence is labeled *subsynchronous*. A three-phase capacitor bank in series with the inductances in each phase forms three oscillators. Also, the mechanical shaft of a large turbo-generator has natural oscillators with frequencies below the synchronous frequency of the network. Under a *subsynchronous resonance* (SSR) condition, a mechanical oscillator in the shaft interacts with the electrical oscillators formed in the three-phase network. As a result, excessively distorted currents and voltages at frequencies below the rated frequency, and large torsional torques on the shaft assembly of the turbo-generator develop.

In a power system prone to subsynchronous resonance, small disturbances trigger the interplay between the mechanical and electrical subsystems and cause a gradual increase of the energy of the oscillations, which takes several seconds (up to a minute) to reach dangerous levels. For example this can happen at the time of synchronizing a generator with an energized network. Following a major disturbance, such as a short circuit, energy is forcibly absorbed into the oscillators, and the process speeds up to a few seconds or even less.

An unwanted phenomenon leading to damage, subsynchronous resonance must be diagnosed, and prevented by implementing counter-measures.

Several methods in the time and frequency domain have been applied to study subsynchronous oscillations in power systems. From a physical point of view, the system under study is nonlinear. The connection between the electrical network and the mechanical shaft assembly happens through the air gap of the synchronous machine where the electromagnetic torque develops. This torque is described by a nonlinear relationship among the currents flowing in the windings of the rotor and the stator. Moreover, advanced power systems of today have many power electronic devices that switch branches in and out of the network periodically, and are highly nonlinear. Therefore, in order to make a rigorous judgment about the risk of a scenario or the effectiveness of a proposed solution, detailed nonlinear modelling becomes necessary. However, in order to apply the powerful linear control design techniques, linear models of the system around an operating point are needed.

The increasing use of high-power electronic devices in power transmission, has led to the recent development of the "Flexible AC Transmission System" (FACTS) concept, a

technology that enables the power grid to be utilized closer to its theoretical thermal capacity. FACTS is not a single, high-power electronic controller, but rather a collection of controllers, which can be applied individually or collectively in a specific power system [1].

One of the FACTS devices used for series compensation is the Thyristor Controlled Series Capacitor (TCSC). A major advantage of TCSC is that it significantly reduces the subsynchronous resonance problem.

1.1 Thesis Motivation

This work was motivated by the realization that TCSC shows a behaviour towards subsynchronous frequencies that, although recognized, is not fully understood. The first researchers to report on this characteristic, known as "passive damping", were Ron Hedin and Stephen Weiss who published a paper comparing the subsynchronous damping of different series compensation methods. Although TCSC does not have main resistive components, it poses a significant resistive behaviour towards subsynchronous frequencies.

The switches used for implementing TCSC are thyristors which rely on natural zero-crossings of the current to turn off. Therefore, no energy loss can be attributed to their commutation specially when thyristors are considered ideal. However, the passive damping still shows itself in simulations with ideal switches.

The initial question posed to us was the origin of this effect, and whether it is enough to rely on for all cases to damp subsynchronous oscillations. Is there a way to increase the damping in TCSC compensated systems?

It has to be emphasized that TCSC, by virtue of its special structure that resembles that of an LC filter, is already expected to reduce the risk of subsynchronous resonance. However, this structural similarity, does not explain passive damping, because this effect has a resistive nature, while a parallel combination of a linear capacitor and inductor, does not have any resistance.

1.2 Thesis Objectives

Based on the understanding of the situation as depicted above, the need for a thorough study of the damping in TCSC compensated systems was recognized. The immediate goal is to shed light on the resistive behaviour of TCSC, and to find out where it is rooted. Then, equipped with this understanding, the next aim is to find ways to increase the damping of TCSC towards subsynchronous disturbances to arrive at a more reliable means of series compensation.

In order to control the TCSC, a proper dynamical model is needed. Therefore, in the quest for better control of the switching of the TCSC thyristors, one naturally has to obtain a model that is able to characterize the behaviour of the system in an efficient way. In short, *in this thesis we seek to analyze the behaviour of TCSC with regards to subsynchronous oscillations, and to increase the damping effect of TCSC on subsynchronous disturbances by controlling the firing of the thyristors.*

1.3 Thesis Organization

In this chapter, after a general description of the problem of subsynchronous resonance, the motivation for the work and the goals of the research are stated. The remaining chapters contain the work that was done in order to achieve the goals of the thesis. These are organized as follows:

Chapter 2 presents the background material and contains the literature overview on the topic of subsynchronous oscillations, with emphasis on the use of thyristor controlled series capacitors. A chronological account of events and developments related to this topic is presented.

The theory of Floquet and the Poincaré map are two key concepts that are used in this work. They are in essence equivalent, with the former arising from linear systems theory and the latter from a geometrical point of view. These concepts and the relation between them are explained in detail. Finally the theory of observer-based stabilizing controllers is

briefly reviewed.

In Chapter 3, first a comparison is made between a system of two linear coupled oscillators and a simplified power system in which subsynchronous instability occurs. The comparison is aimed at gaining more insight into the problem of subsynchronous resonance by avoiding the complexity of detailed models needed for realistic situations. The machine in the study is a two-phase synchronous machine with a magnetic core of infinite permeability and a shaft consisting of two masses. With all the measures taken to simplify the system, there is a certain amount of modeling that is unavoidable.

Then, the First IEEE Subsynchronous Resonance Benchmark Model with fixed series compensation is studied using transient simulation and eigenvalue analysis. This will form the basis for the treatment of thyristor controlled compensation in later chapters.

In Chapter 4, a physical explanation is provided for the passive damping or resistive behaviour of TCSC at low frequencies using analytical calculations and discrete Fourier transformation. The resistance is then obtained for a typical TCSC for the range of subsynchronous frequencies in three different synchronization schemes. The study yields the frequency response of TCSC in open loop operation. This response varies considerably with the synchronization scheme.

Two linearization techniques have been applied in the past to obtain linear dynamical models for TCSC. These techniques, namely the average steady-state and the Poincaré map linearization are compared with regards to their treatment of the passive damping. The Poincaré map modelling is chosen for its accuracy in portraying this characteristic.

Chapter 5 explains in detail the steps taken in order to complete the linear model previously developed for TCSC compensated systems based on the Poincaré mapping concept. That model was aimed at assessing the stability of the system by obtaining the eigenvalues. In order to make it suitable for damping controller design, the missing part is the coefficient set that gives the dependence of the model on the changes in the firing angles of the thyristors. A general method to calculate these coefficients is presented, where the parameters of the model are obtained by calculating the perturbation from the periodic orbit of the circuit.

The First IEEE Subsynchronous Resonance Benchmark Model with TCSC is linearized at different operating points, and the effect of changing the steady-state conduction angle on the stability of the subsynchronous modes is studied by eigenvalue analysis.

Chapter 6 discusses the control and damping of the subsynchronous oscillations. Using the model developed in chapter 5, an all-stabilizing firing controller based on pole placement technique is designed for the TCSC to damp subsynchronous mechanical oscillations. The controller is made to work with two different sampling rates to determine the effect on the damping of subsynchronous modes. Also a comparison is made between our model and the models developed by other research groups. The comparison is qualitative, however, since an exact quantitative comparison requires data that is not available in the publications.

Chapter 7 is a discussion on the steady state theory of TCSC. This is a result obtained as a byproduct of the damping controller design, but it is a separate subject. We develop relations that describe the steady state of the TCSC, and yield its compensation level with an open-loop firing scheme more general than the equidistant firing strategy. A dynamical study with respect to subsynchronous instability is included.

Finally in Chapter 8 the work is concluded by highlighting the obtained results and making suggestions towards future research.

The contributions of this thesis are summarized as follows:

- Analytical explanation of the resistive behaviour of TCSC at subsynchronous frequencies, and deriving the frequency response of TCSC with respect to the subsynchronous oscillations.

- Development of a linear discrete state-space representation of a TCSC compensated system and its use in the design of a closed-loop SSR-damping controller for TCSC.

- Introduction of deviation angle in the open loop firing of TCSC, and deriving the analytical relations describing the fundamental reactance, the capacitor voltage, and the inductor current of TCSC with deviated firing.

Chapter 2

Background

While the installation of series capacitors on transmission lines started as early as the 1920s [2], subsynchronous resonance caused by series capacitors was detected in 1970 at the Mohave power plant [3, 4] only after it had actually happened. The interaction of the electrical and mechanical subsystems causing oscillations between the rotors of a turbo-generator shaft assembly was rarely studied, because the shaft was usually assumed to be one rigid body. By 1937, three types of problems associated with series capacitor applications were already known and thoroughly investigated [5]:

1. Distorted and excessively large transformer exciting currents, due to saturation.
2. Hunting of synchronous machines.
3. Self-excitation of induction motors.

The first effect, called *ferroresonance*, happens when an unloaded or very lightly loaded transformer is energized through a series capacitor, resulting in abnormally large and distorted exciting currents. These transient may currents persist for a long time, and may settle into a steady state with harmonic content.

Hunting is a periodic variation in speed of a synchronous machine from its rated speed at low frequencies (in the order of 1 Hz). During hunting the *rigid body mode* of the machine is excited. That is, the rotor oscillates as one mass around the rated mechanical speed. This

effect can arise even without a series capacitor, but the presence of a capacitor may make it worse.

Consider an induction motor connected through a series capacitor bank to a line. Since the inductance in the series path is large, the natural frequency of the resonance between the capacitor and the equivalent inductance is less than the synchronous frequency of the network. A disturbance in the system causes currents at this lower frequency to flow in the line and in the armature windings. These currents see the induction machine as a generator. The impedance of the circuit is low at the resonance frequency due to the cancellation of the inductive and capacitive reactances. Therefore, these currents become sustained and may reach relatively large values. The induction motor is said to be self-excited in this condition.

In 1941, Concordia and Carter presented a theoretical work [6] to show that hunting and self-excitation are two aspects or special cases of a single, more general, characteristic which they called *negative damping* of electrical machinery. The equations presented there are one step short of incorporating subsynchronous oscillations between rotor masses, although with the limited computational power of those days, calculating the response of a system of differential equations was much more of a problem than forming the equations themselves.

During the years to follow, while some utilities in North America became heavily involved in compensating their transmission systems using series capacitors, others refrained because of inherent risks [7]. In 1970, a little before the incident at the Mohave plant, Rustebakke and Concordia [7] published yet another paper drawing attention to the problem of self-excited oscillations in series compensated transmission lines, but subsynchronous resonance was again missed. Finally, in 1973 a sound analysis of the self-excited torsional oscillations [8] was presented and the foundations for the more advanced analysis methods of today were laid.

SSR phenomena are divided into three types: *Induction Generator Effect*, *Torsional Interaction*, and *Torque Amplification*. Induction generator effect is very similar to the self-excitation of induction machines. The latter two, during which a shaft torque starts increasing until it reaches destructive levels, are more similar to hunting in principle. However, torque amplification, which follows a major disturbance, is the more severe of the two. The

modelling detail needed to study torsional interaction and torque amplification is the same. In the next section these three types are described from a physical point of view.

Although the serious damage which occurred in two extreme cases in 1970 and 1971 [9] has been avoided since then (for example, by using SSR relays to trip a turbo-generator), the SSR problem still remains a field open to more investigation.

First, it has been discovered that if such oscillations are present, fatigue in the shaft material reduces its life expectancy [10]. Second, this type of interaction arises not only with series capacitor compensation, but also with other power system components such as power system stabilizers, high voltage DC converter controls, static var compensators, high speed governor controls, and variable speed drive converters [3].

The thyristor controlled series capacitor (TCSC) has been found to be effective in damping subsynchronous oscillations [11]. This characteristic is so important to system planners that the first prototypes of TCSC are installed in locations where it is possible to perform SSR tests in order to verify theoretical studies.

Table 2.1 lists some dates of events and developments related to subsynchronous resonance and TCSC.

Table 2.1: Chronological History

First practical induction machine	1890	
First production of power capacitors	1914	
First usage of capacitor for series compensation	1928	At Ballston, N.Y. [12]
Two-reaction theory for synchronous machines	1929	By R. H. Park
Two-reaction theory applied for analysis of series capacitor in the armature circuit	1937	By S. B. Crary
Analysis of hunting and self-excitation as two aspects of a more general nature	1941	By C. Concordia & G. K. Carter
First occurrence of subsynchronous torsional instability	1970	At Mohave Power Plant
First theoretical analysis of self-excited torsional oscillations with series capacitors	1973	By C. E. J. Bowler, D. N. Ewart & C. Concordia
First demonstration of thyristor-controlled series capacitor	1991	By ABB, Sweden
First three-phase TCSC	1993	At Kayenta Substation

2.1 Physical Nature of SSR

Fig. 2.1 shows a diagram of a synchronous generator connected to a series compensated transmission line.

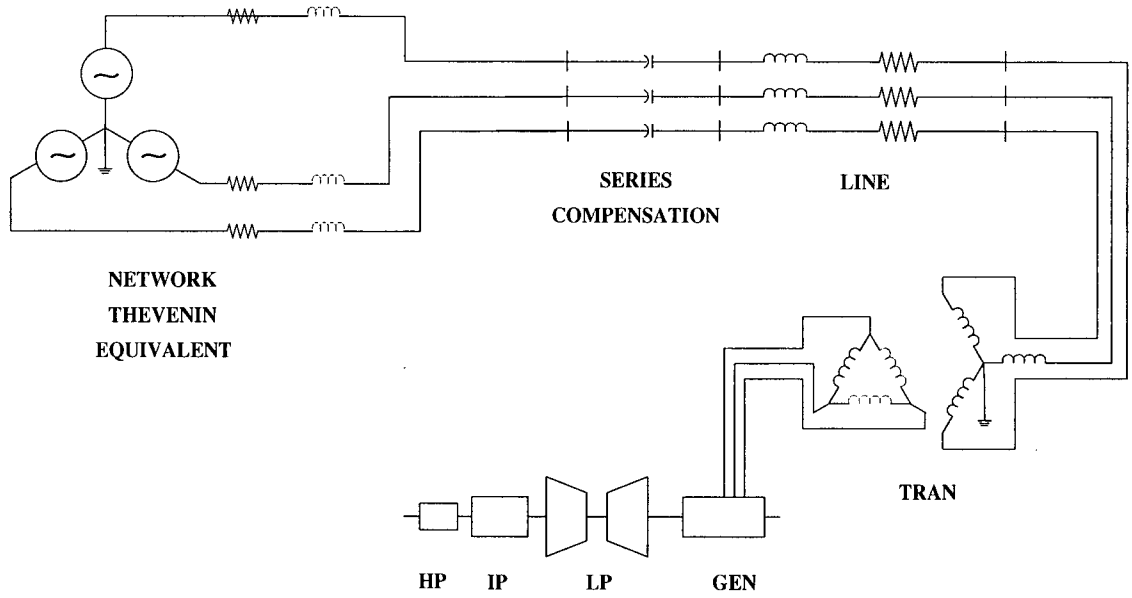

Figure 2.1: Synchronous generator connected to a series compensated line

The system inductances, together with the series capacitor in each phase, form a resonance circuit with the natural frequency

$$f_{Ne} = f_s \sqrt{\frac{X_C}{X_{tot} + X''}} \qquad \text{Hz} \tag{2.1}$$

where f_s is the rated electrical frequency of the network. X_{tot} is the sum of the reactances of the Thevenin equivalent circuit, the line, and the transformer, and X'' is the generator subtransient reactance. $X_C = 1/(2\pi f_s C)$ is the reactance of the capacitor. The value of f_{Ne} is less than f_s.

For any disturbance, three-phase currents at frequency f_{Ne} Hz flow in the armature [3]. The positive sequence components of these currents produce a magnetic field which rotates at an angular mechanical speed of $(\frac{2}{p})2\pi f_{Ne}$ rad/s, p being the number of machine poles. In the rest of this discussion, for the sake of clarity, the number of poles is assumed to be 2, so there is no need to distinguish between the electrical and the mechanical radians.

Since the speed of the rotor is higher than $2\pi f_{Ne}$ rad/s, the rotor circuits turn faster than this rotating magnetic field. In this situation an induction generator is formed, and mechanical energy is converted to electrical energy at the corresponding subsynchronous frequency. During this time, the machine acts as a synchronous generator at f_s Hz and as an induction generator at f_{Ne} Hz (Induction generator effect).

Torsional interaction is the interplay between the mechanical shaft system and a series capacitor compensated electrical network. Small signal disturbances in a power system result in simultaneous excitation of all the natural electrical and mechanical modes. The turbine-generator shaft responds to disturbances with oscillations at torsional natural frequencies.

The oscillation of the generator rotor at the frequency f_{Nm} Hz causes modulation of the terminal voltage. This modulation results in a subsynchronous voltage component at frequency $f_s - f_{Nm}$ Hz and a supersynchronous voltage component at frequency $f_s + f_{Nm}$ Hz. When the subsynchronous frequency is close to a network natural frequency f_{Ne} Hz, the resulting armature currents produce a magnetic field which is phased to produce a torque which reinforces the aforementioned generator rotor oscillations. This phenomenon is termed torsional interaction. One way of perceiving torsional interaction, is the insertion of negative resistance in the generator armature as viewed from the terminals, and the insertion of a negative damping torque on the generator rotor as viewed from the mechanical system.

Following a significant disturbance in a series capacitor compensated system, large electromagnetic torques that oscillate at a frequency $f_s - f_{Ne}$ Hz develop. If this frequency is near any mechanical mode f_{Nm} Hz of the shaft, the resulting shaft torques are much larger than those produced by faults in a system without series capacitors and the mechanical oscillations are forced to increase rapidly. This effect is referred to as shaft torque amplification.

2.2 Analysis Methods of Subsynchronous Resonance

This section is a short account of the methods that are used to study subsynchronus resonance. For a comprehensive list of publications on the analysis methods, field tests and other related studies, see [13, 14, 15, 16, 17].

The most common tools for the study of SSR are [18]:

1. Frequency scanning
2. Eigenvalue analysis
3. Torque per unit velocity method
4. EMTP analysis

Frequency scanning is a cost-effective method applied as a preliminary analysis to roughly locate problematic frequencies. This technique computes the equivalent resistance and reactance, seen by looking into the network from a point behind the stator winding of a particular generator, as a function of frequency [19].

If a linearized time-invariant state space description of the system is available, eigenvalue analysis can be performed to determine whether the natural modes of the system are stable or not. The state space model is either continuous

$$\dot{\mathbf{x}}(t) = \mathbf{A}\mathbf{x}(t) + \mathbf{B}\mathbf{u}(t) \tag{2.2a}$$

$$\mathbf{y}(t) = \mathbf{C}\mathbf{x}(t) + \mathbf{D}\mathbf{u}(t) \tag{2.2b}$$

or discrete

$$\mathbf{x}(n+1) = \mathbf{A}\mathbf{x}(n) + \mathbf{B}\mathbf{u}(n) \tag{2.3a}$$

$$\mathbf{y}(n) = \mathbf{C}\mathbf{x}(n) + \mathbf{D}\mathbf{u}(n) \tag{2.3b}$$

where $\mathbf{x} \in \mathbb{R}^{n_x}$ is the state vector, $\mathbf{u} \in \mathbb{R}^{n_u}$ is the input vector, and $\mathbf{y} \in \mathbb{R}^{n_y}$ is the vector of outputs. $\mathbf{A} \in \mathbb{R}^{n_x \times n_x}$, $\mathbf{B} \in \mathbb{R}^{n_x \times n_u}$, $\mathbf{C} \in \mathbb{R}^{n_y \times n_x}$ and $\mathbf{D} \in \mathbb{R}^{n_y \times n_u}$ are the system constants. For eigenvalue analysis, only the $\mathbf{A}$-matrix is needed. On the other hand, to design feedback controllers, the full model has to be available.

The eigenvalues are the solutions of the equation

$$\det(\lambda \mathbb{1} - \mathbf{A}) = 0 \tag{2.4}$$

In the continuous domain, if an eigenvalue lies on the right-hand side of the $j\omega$-axis in the s-plane, then it is unstable. In the discrete domain, if an eigenvalue lies outside the unit circle in the z-plane, it is unstable.

Eigenvalue analysis is an attractive method since it provides the frequency and the damping of all the modes for the entire modelled system. However, power systems are nonlinear and time-varying. Their linearization about the steady state may result in a linear *time-periodic* system, especially if electronic switching is present. Care must be taken when trying to study the stability of time-varying systems using eigenvalue analysis. It is tempting to suggest that if for each n, all the eigenvalues of $\mathbf{A}(n)$ lie inside the unit circle, then the zero state, $\mathbf{0}$, of $\mathbf{x}(n+1) = \mathbf{A}(n)\mathbf{x}(n)$ is asymptotically stable (a similar statement can be made about the continuous system). However, this is not always the case [20]. In Section 2.7, some results from the linear systems theory that enable eigenvalue analysis to be safely applied to time-periodic systems are reviewed.

The torque per unit velocity method is another frequency domain approach commonly used to estimate damping of SSR modes. Its basic idea is to trace the effect of a small sinusoidal mechanical disturbance through the electrical network [21].

EMTP simulations take care of several nonlinearities and imbalances which are difficult to deal with by other methods. The differential equations are solved numerically step by step in discrete time. As SSR phenomena are relatively slow transients, it may be necessary to run EMTP simulations for many seconds (even minutes) to be able to observe the phenomena of interest.

In this thesis, the eigenvalue and EMTP analysis methods are used to study the behaviour of thyristor controlled series capacitor compensated systems with regard to subsynchronous oscillations.

2.3 Compensation with Thyristor Controlled Series Capacitor

In recent years a considerable amount of effort has been dedicated to research into the use of power electronics for fast switching of reactive compensation. A growing interest among North American utilities spurred the Electric Power Research Institute (EPRI) to initiate the Flexible AC Transmission System (FACTS) project [22].

TCSC is an important member of the FACTS devices family. It is intended to perform the following tasks [23]:

1. Direct control of power flow and mitigation of loop flow
2. Transient stability control; improving the transient stability of the power system
3. Damping of power oscillations and mitigation of subsynchronous resonance

The idea of TCSC was formed during the 1980s by Vithayathil of Bonneville Power Administration, and Hingorani of Electric Power Research Institute. Hingorani later proposed the more general concept of Flexible AC Transmission System [4].

In a TCSC module, the series capacitor is provided with a parallel path, consisting of a back-to-back thyristor switch and a surge inductor, as shown in Fig. 2.2. Also included is a metal oxide varistor (MOV) for overvoltage protection, and a bypass circuit breaker, typical of series capacitors. A complete TCSC system comprises several such modules in series, and is added to a conventional series capacitor bank as part of an overall installation to aid power system performance [24].

In this thesis, a thyristor is modelled as an ideal lossless switch which turns on instantly when the anode to cathode voltage is positive, and the gate pulse is on. It turns off at the instant when the current from anode to cathode goes through zero and the current direction is going to change. In reality a thyristor, as any other semiconductor switch, has limitations that must be taken into account in the design of TCSC.

There are already three prototype projects in operation in the USA that have demonstrated the successful implementation of thyristor controlled series compensators [4]. The

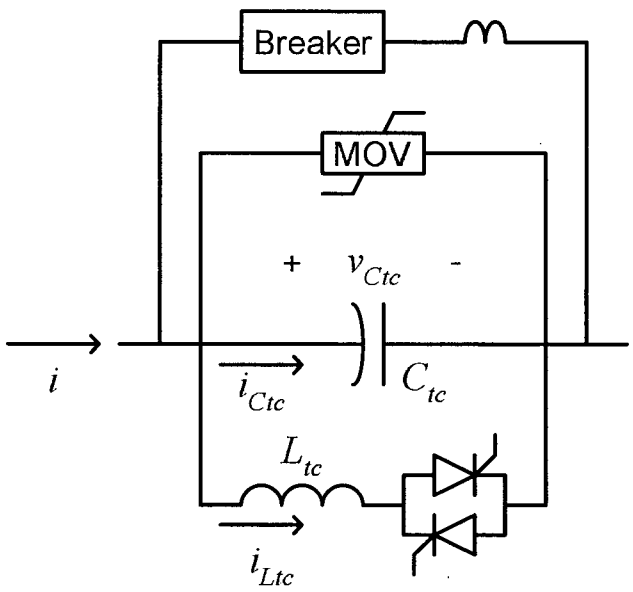

Figure 2.2: TCSC module power circuit

analysis, based on the torque per unit velocity method [25] and the experimental data based on SSR performance tests [11], have indicated that TCSC does not normally contribute to SSR. It is even claimed by Piwko and others [11] that TCSC is SSR neutral and can reduce SSR effects caused by nearby fixed series capacitors.

Taking a general look at the TCSC structure, it is evident that it resembles an LC filter except for the thyristors in the inductive branch. Fig. 2.3 compares the frequency response of the susceptance[1] of a single capacitor and that of a parallel combination of a capacitor and an inductor that yields the same total compensation at 60 Hz. The LC combination goes into the inductive region for frequencies below the point indicated by a +. Therefore, the possibility of resonance between the electrical and mechanical subsystems is automatically eliminated for frequencies below that point. This characteristic is termed *detuning* of the resonance.

TCSC also shows detuning, however its behaviour is more complex than an LC filter. Specifically there is damping associated with the switching action that happens in the device. TCSC, even in open loop operation, shows a resistive behaviour towards disturbances at

[1]Susceptance, B, is the imaginary part of the admittance, $\boldsymbol{Y}$, such that $\boldsymbol{Y} = G + jB$.

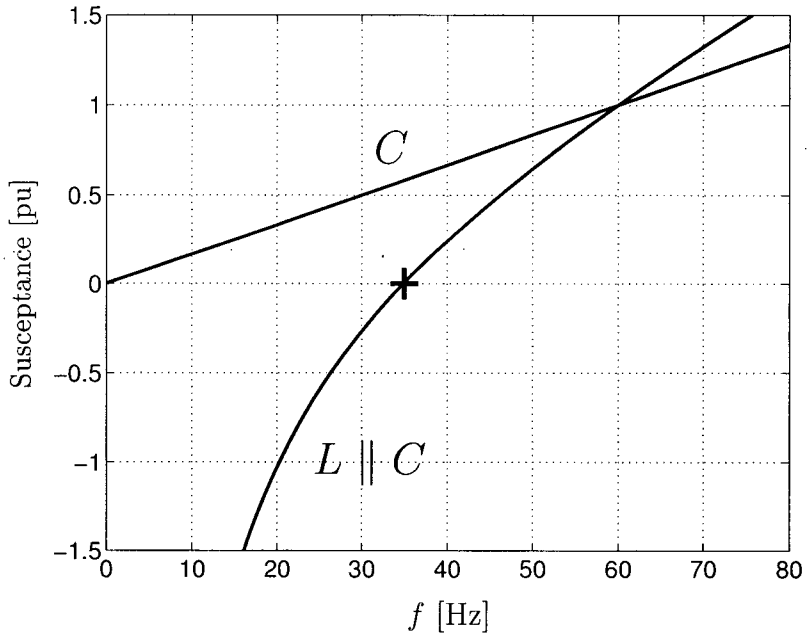

Figure 2.3: Comparison of the frequency response of a capacitor and an LC filter

frequencies below its switching frequency. This behaviour was first reported by Ron Hedin, Stephan Weiss, and others who observed it both on a transient network analyzer and in simulation [25, 26]. The damping associated with the open loop operation of the TCSC is termed *passive* as opposed to the active damping effected by higher level controls [27].

From the viewpoint of this work, publications about TCSC are categorized into the following groups.

FACTS concepts: These publications review FACTS technology, its origins; the ways in which it is changing the transmission and distribution of power, and the role of TCSC in the set of FACTS controllers, for example [1, 28, 29, 30, 31].

SSR characteristics: Many publications discuss the SSR characteristics of TCSC. References [21, 27, 32, 33, 34, 35, 36] analyse the SSR mitigation with this device using linearized models. Detailed EMTP simulations are very useful for this purpose [25, 37], however, they give less general results about the behaviour of the system. The fact that TCSC shows a pronounced nonlinear behaviour makes EMTP simulation meth-

ods more reliable than others. The IEEE SSR benchmark models [38, 39], extended to include a thyristor controlled series capacitor, are normally used as the test cases. Fig. 2.4 shows the system chosen as the test case in this thesis. The parameters of the system are given in Appendix B.

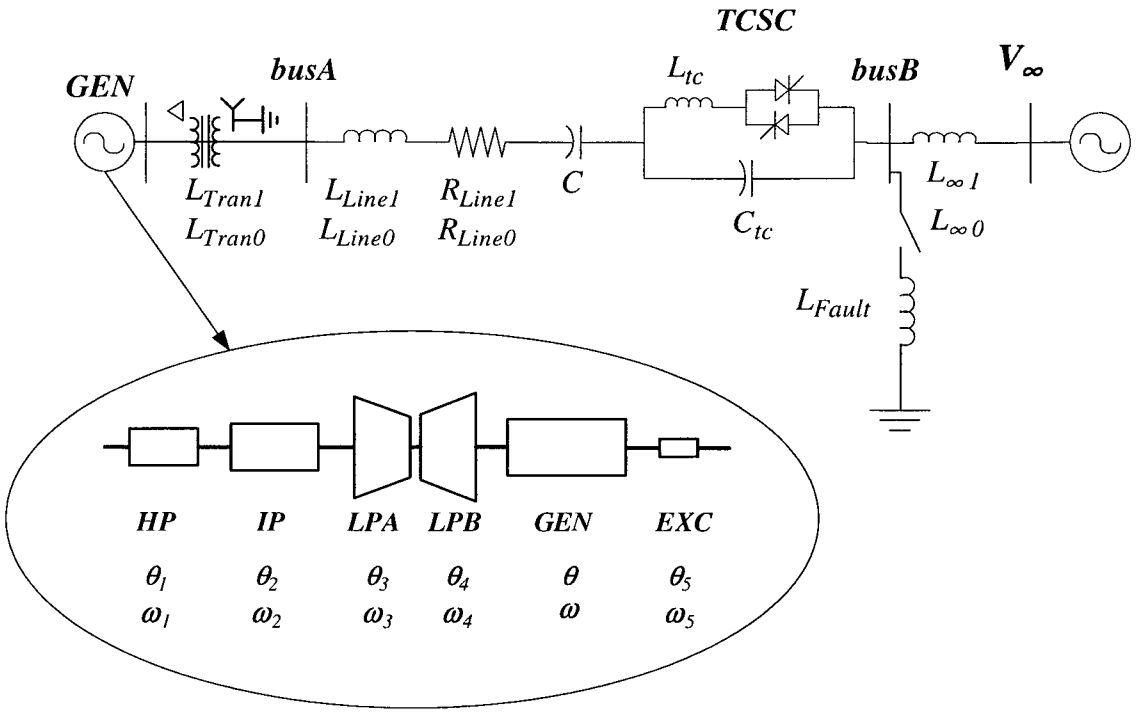

Figure 2.4: First SSR Benchmark Model System extended to include a TCSC

Circuit behaviour: This group of publications discusses the circuit behaviour of TCSC. It is common practice to apply a sinusoidal current source to the device and calculate the resulting voltage [22, 40, 41, 27, 42]. What are known as *capability curves* give the voltage or reactance of TCSC as a function of line current [24, 43].

In order to apply eigenvalue analysis in a circuit containing TCSC, a linear model must be available. This is a major issue, since TCSC is highly nonlinear, and linearizing it by averaging the steady state is inadequate to show the true behaviour of TCSC in stability studies [27, 44]. A method to use instead of steady-state averaging, is the linearization of a Poincaré map [41, 45, 32]. This technique captures the passive

damping characteristic of TCSC, and therefore is very well suited for subsynchronous resonance studies. More about this method will appear later on.

Field test results: The first demonstration project of TCSC was commissioned in 1991 at the 345 kV Kanawha River Substation in West Virginia, USA, of American Electric Power Service Corporation. This was a test installation of thyristor switches in one phase for rapid switching of series capacitor segments, and was supplied by ABB of Sweden. In October 1992 the first three-phase TCSC was installed at the 230 kV Kayenta Substation in Arizona by Western Area Power Administration (WAPA). A large prototype three-phase TCSC was installed in 1993 at the 500 kV Slatt Substation in Oregon by Bonneville Power Administration (BPA). This project was sponsored by Electric Power Research Institute (EPRI), and the equipment was developed by General Electric. There are papers that describe the field tests performed at these sites, for example [11, 46, 47].

Other topics: The problems and interests associated with TCSC are numerous and definitely not confined to SSR mitigation. TCSC provides more controllability over the flow of power in the line [48], and affects many types of stability in a power system. On the other hand, because it produces harmonics [49], it may be a source of problems as well.

2.4 Fundamental Reactance and Capability Curves of TCSC

Fig. 2.5 shows a single-phase TCSC connected to a sinusoidal current source $i_s(t)$. The voltage across the capacitor is denoted by v_{Ctc}, and the current through the inductor is denoted by i_{Ltc}.

Suppose that the time origin has been chosen such that $i_s(t) = \sqrt{2}I_s \cos \omega_s t$. This circuit achieves steady state when the anti-parallel thyristors are fired with equal delays with respect to the zero-crossings of either the capacitor voltage or the line current. Typical steady-state waveforms of a single-phase TCSC with *equidistant firing* are given in Fig. 2.6

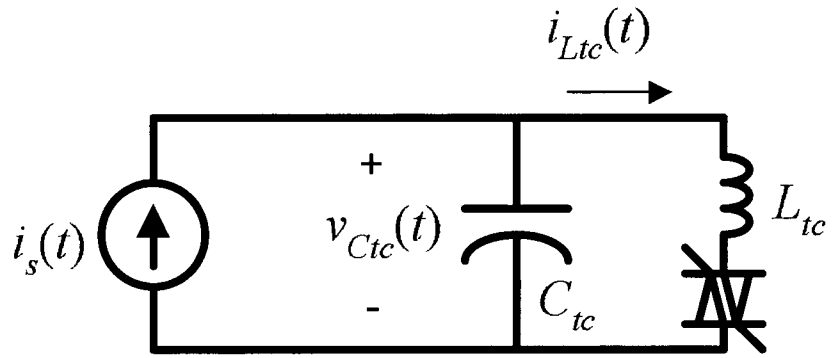

Figure 2.5: A single-phase TCSC

for the capacitive mode and in Fig. 2.7 for the inductive mode. Capacitive mode means that the fundamental reactance of TCSC is capacitive, and inductive mode means that the fundamental reactance of the TCSC is inductive. This is evident from the figures by noting that in the capacitive mode (Fig. 2.6), v_{Ctc} lags i_s by 90°, and in the inductive mode (Fig. 2.7), v_{Ctc} leads i_s by 90°.

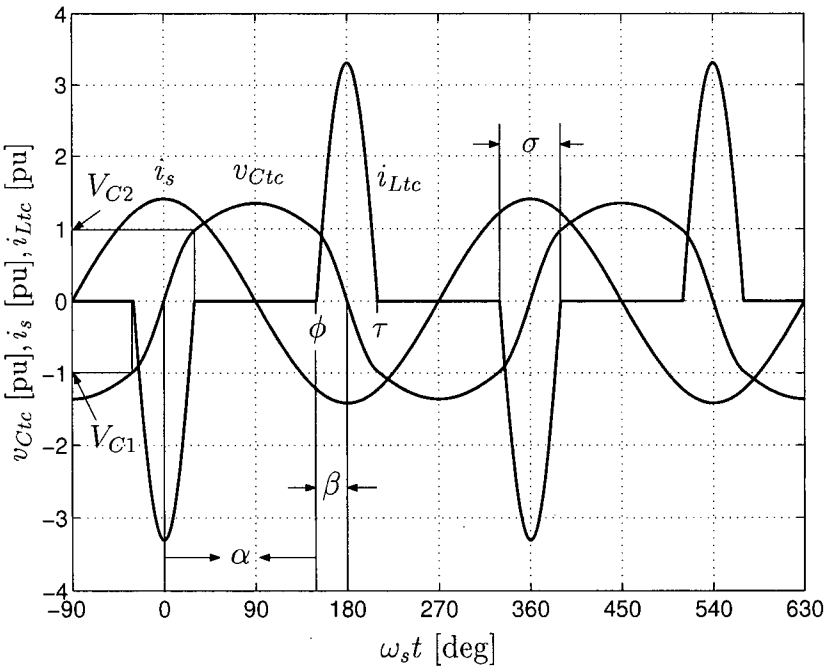

Figure 2.6: Steady-state waveforms of TCSC in capacitive operation

As shown in the figures, the zero-crossing of the capacitor voltage is used to define the *firing angle*, α. The firing pulse generator, however, is either synchronized with the zero-

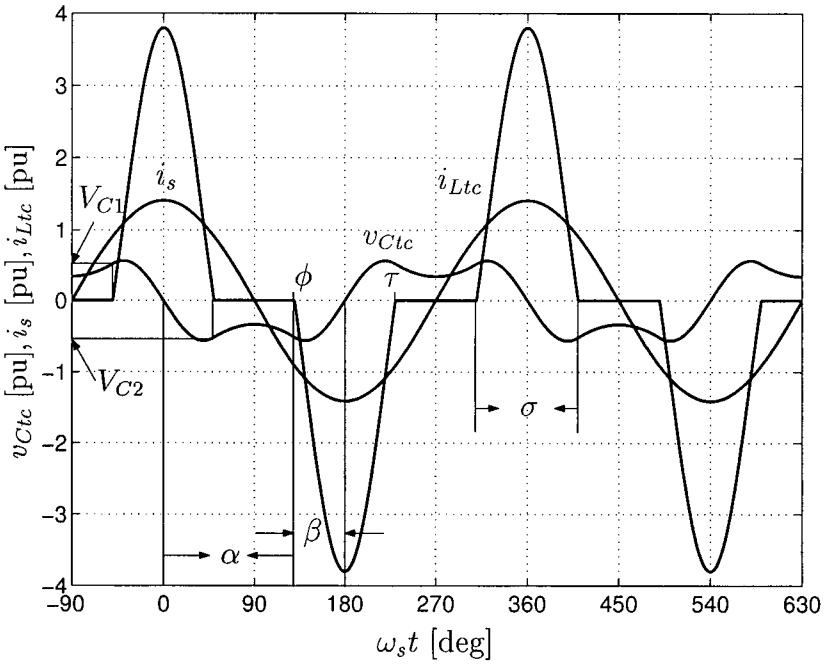

Figure 2.7: Steady-state waveforms of TCSC in inductive operation

crossings of the capacitor voltage, v_{Ctc}, or those of the line current, i_s [4]. If the line current is used for synchronization, the gate pulse is sent to the appropriate thyristor $\alpha - 90°$ after the zero-crossing of i_s. As discussed in Chapter 4, the frequency response of the TCSC is dependent on this synchronization.

To preserve the meaning of α, measured by definition from the capacitor voltage zero-crossing, the turn-on angle is generally referred to by $\phi = \omega_s t_{on}$, where t_{on} is the instant when a thyristor starts conducting. Note that for the time origin chosen in Fig. 2.6 and Fig. 2.7, $\phi = \alpha$. In addition, regardless of the time origin and reference point for measurement, we have $\Delta\phi = \Delta\alpha$. The turn-off angle is generally referred to by $\tau = \omega_s t_{off}$, with t_{off} being the instant when the current in the inductive branch vanishes. The *angle of advance* is defined by

$$\beta \triangleq 180° - \alpha \qquad \text{deg} \tag{2.5}$$

where $\triangleq$ means "equal by definition". In steady state the *conduction angle*, σ, equals 2β. In writing the steady state relations of the TCSC waveforms, it is convenient to use the

following parameters [4]:

$$\omega_{Ntc} = \frac{1}{\sqrt{L_{tc}C_{tc}}} \qquad \text{rad/s} \tag{2.6}$$

$$\kappa \triangleq \frac{\omega_{Ntc}}{\omega_s} = \sqrt{\frac{X_{Ctc}}{X_{Ltc}}} \tag{2.7}$$

ω_{Ntc} is the natural resonance frequency between C_{tc} and L_{tc}, and κ is the ratio of this frequency to the synchronous frequency. X_{Ctc} and X_{Ltc} are the reactances of the capacitor and inductor, respectively.

The current through the inductor during the conduction time is

$$i_{Ltc}(t) = \frac{\kappa^2}{\kappa^2 - 1}\sqrt{2}I_s[\cos\omega_s t - \frac{\cos\beta}{\cos\kappa\beta}\cos\omega_{Ntc}t] \quad , \quad -\beta \leq \omega_s t \leq \beta \tag{2.8}$$

In steady state, the capacitor voltage at $\omega_s t_1 = -\beta$, when one of the thyristors turns on, is given by

$$V_{C1} = \frac{\sqrt{2}I_s X_{Ctc}}{\kappa^2 - 1}[\sin\beta - \kappa\cos\beta\tan\kappa\beta] \tag{2.9}$$

Because of the symmetry of the waveforms, at $\omega_s t_2 = \beta$, when the thyristor turns off, we have

$$v_{Ctc}(t_2) = V_{C2} = -V_{C1} \tag{2.10}$$

The expression for $v_{Ctc}(t)$ is

$$v_{Ctc}(t) = \frac{\sqrt{2}I_s X_{Ctc}}{\kappa^2 - 1}[-\sin\omega_s t + \kappa\frac{\cos\beta}{\cos\kappa\beta}\sin\omega_{Ntc}t] \quad , \quad -\beta \leq \omega_s t \leq \beta \tag{2.11}$$

$$v_{Ctc}(t) = V_{C2} + \sqrt{2}I_s X_{Ctc}[\sin\omega_s t - \sin\beta] \quad , \quad \beta < \omega_s t < \pi - \beta \tag{2.12}$$

In steady state, v_{Ctc} is periodic with the fundamental frequency equal to the synchronous frequency of the network, and contains odd harmonics of the order $3, 5, 7, \cdots$.

The equivalent reactance of TCSC at the fundamental frequency, X_{TCSC}, is obtained by dividing the rms magnitude of the fundamental component of v_{Ctc} by I_s, and is given by

$$X_{TCSC} = \frac{V_{Ctc}}{I_s} = X_{Ctc} - \frac{X_{Ctc}^2}{X_{Ctc} - X_{Ltc}}\frac{(2\beta + \sin 2\beta)}{\pi} + \frac{4X_{Ctc}^2}{X_{Ctc} - X_{Ltc}}\frac{\cos^2\beta}{(\kappa^2 - 1)}\frac{[\kappa\tan\kappa\beta - \tan\beta]}{\pi} \tag{2.13}$$

The variation of X_{TCSC}/X_{Ctc} as a function of β is shown in Fig. 2.8. This characteristic is obtained for the synchronous frequency. The appropriate value for κ, ensures that there is only one resonance point for $0 < \beta < 90°$. The resonance advance angle, β_{Ntc}, is obtained from $\cos \kappa\beta_{Ntc} = 0$. The typical value of β_{Ntc} is 35°. Near the resonance point, TCSC has a very high impedance that results in a very high voltage drop. Hence, it is necessary to operate TCSC such that X_{TCSC}/X_{Ctc} stays within limits of typically 2 and 3.

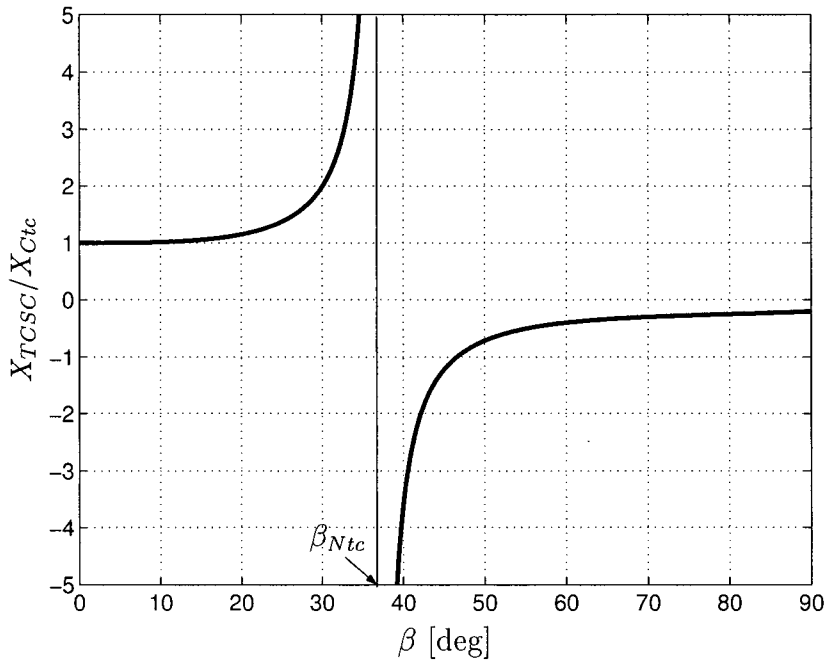

Figure 2.8: Variation of the equivalent reactance of TCSC as a function of β

A set of *capability* curves [24] in terms of module voltage versus line current for a single TCSC module is given in Fig. 2.9. For operation in the capacitive region, the maximum firing advance angle, β, limits the capability up to a value of line current where the maximum voltage constrains the operation. The maximum voltage constraint is typically given for three durations: continuous, 30-minutes, and a few seconds (1 to 10, depending upon system requirements).

Inductive operation is limited by the maximum firing delay, α, at low line currents, and maximum thyristor current at high line currents. Between these constraints is an additional limiting characteristic related to harmonics. The harmonics cause additional heating in the surge inductor and thyristor, and may cause peak voltages which approach the voltage

withstand capability of the capacitors and MOV.

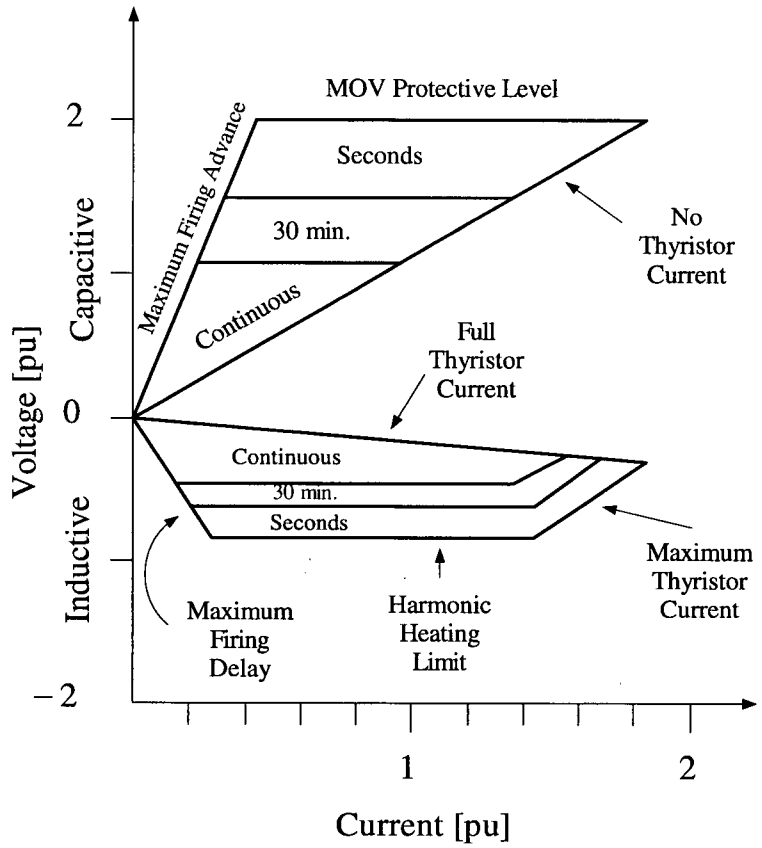

Figure 2.9: Typical TCSC V-I capability curves for a single module

The TCSC capability can also be illustrated in terms of reactance versus line current, as shown in Fig. 2.10. This figure shows the gap in control range between capacitive and inductive operation, as well as in the dynamic range with increasing line current.

2.5 Linear Time-Periodic Systems

A three-phase power system with a TCSC is instantaneously unbalanced. However, it returns to its original state after one cycle of the main period (1/60 s). The power system state equations can be linearized between any two switching instants. The dynamics of the system at all times are described by different sets of state equations connected by boundary conditions that relate the states before and after each switching. The equations obtained

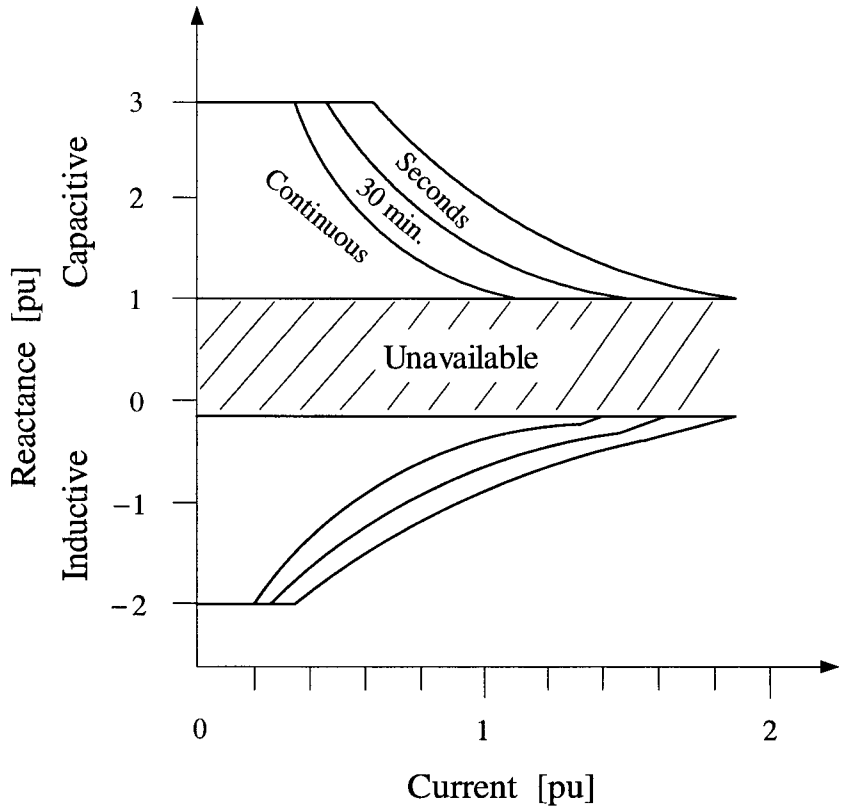

Figure 2.10: Typical TCSC X-I capability curves for a single module

this way are linear time-periodic.

If an equivalent linear time-invariant system can be found by means of a transformation that preserves the stability properties of the linear time-periodic system, then eigenvalue analysis can be performed on the transformed system and the results extended to the original one. The following definitions and theorem from the linear systems theory [20] show that such a transformation indeed exists.

Definition 1 Let $\mathbf{P}_{eq}(t)$ be an $n_x \times n_x$ matrix defined over $-\infty < t < \infty$. It is assumed that $\mathbf{P}_{eq}(t)$ and $\dot{\mathbf{P}}_{eq}(t)$ are nonsingular and continuous for all t. Let $\mathbf{x}_{eq} = \mathbf{P}_{eq}(t)\mathbf{x}$. Then the dynamical equation

$$\dot{\mathbf{x}} = \mathbf{A}(t)\mathbf{x} + \mathbf{B}(t)\mathbf{u} \tag{2.14a}$$

$$\mathbf{y} = \mathbf{C}(t)\mathbf{x} + \mathbf{D}(t)\mathbf{u} \tag{2.14b}$$

and the dynamical equation

$$\dot{\mathbf{x}}_{eq} = \mathbf{A}_{eq}(t)\mathbf{x}_{eq} + \mathbf{B}_{eq}(t)\mathbf{u} \tag{2.15a}$$

$$\mathbf{y} = \mathbf{C}_{eq}(t)\mathbf{x}_{eq} + \mathbf{D}_{eq}(t)\mathbf{u} \tag{2.15b}$$

where

$$\mathbf{A}_{eq}(t) = [\mathbf{P}_{eq}(t)\mathbf{A}(t) + \dot{\mathbf{P}}_{eq}(t)]\mathbf{P}_{eq}^{-1}(t) \tag{2.16a}$$

$$\mathbf{B}_{eq}(t) = \mathbf{P}_{eq}(t)\mathbf{B}(t) \tag{2.16b}$$

$$\mathbf{C}_{eq}(t) = \mathbf{C}(t)\mathbf{P}_{eq}^{-1}(t) \tag{2.16c}$$

$$\mathbf{D}_{eq}(t) = \mathbf{D}(t) \tag{2.16d}$$

are said to be equivalent, and $\mathbf{P}_{eq}(t)$ is said to be an *equivalence transformation.*

Definition 2 A matrix $\mathbf{P}_{eq}(t)$ is called a *Lyapunov transformation* if (1) $\mathbf{P}_{eq}(t)$ and $\dot{\mathbf{P}}_{eq}(t)$ are continuous and bounded on $t_0 \leq t < \infty$ and (2) there exists a constant m such that

$$0 < m < |\det[\mathbf{P}_{eq}(t)]| \quad \text{for all } t \geq t_0 \tag{2.17}$$

Theorem 1 Assume that the matrix $\mathbf{A}$ in (2.14a) is periodic with period T. Let $\mathbf{P}_{eq}(t)$ be defined as

$$\mathbf{P}_{eq}(t) \triangleq e^{\mathbf{A}_{eq}t}\mathbf{\Psi}^{-1}(t) \tag{2.18}$$

where $\mathbf{\Psi}(t)$ is a fundamental matrix[2] of $\dot{\mathbf{x}} = \mathbf{A}(t)\mathbf{x}$ [20]. Then the dynamical equation in (2.14) and the dynamical equation

$$\dot{\mathbf{x}}_{eq}(t) = \mathbf{A}_{eq}\mathbf{x}_{eq}(t) + \mathbf{P}_{eq}(t)\mathbf{B}(t)\mathbf{u}(t) \tag{2.19a}$$

$$\mathbf{y}(t) = \mathbf{C}(t)\mathbf{P}_{eq}^{-1}(t)\mathbf{x}_{eq}(t) + \mathbf{D}(t)\mathbf{u}(t) \tag{2.19b}$$

where $\mathbf{A}_{eq}$ is a constant matrix, are equivalent in the sense of Lyapunov.

[2]A fundamental matrix is by definition an $n_x \times n_x$ matrix whose columns are n_x linearly independent solutions of $\dot{\mathbf{x}} = \mathbf{A}(t)\mathbf{x}$.

A Lyapunov transformation preserves the stability of a dynamical equation, but an equivalence transformation in general does not. According to the above theorem the existence of a Lyapunov transformation that transforms the periodic matrix $\mathbf{A}(t)$ to a constant one is guaranteed.

The homogeneous part of this theorem is the so-called *theory of Floquet.* It states that if $\dot{\mathbf{x}} = \mathbf{A}(t)\mathbf{x}$ and if $\mathbf{A}(t+T) = \mathbf{A}(t)$ for all t, then its fundamental matrix is of the form $\mathbf{P}_{eq}^{-1}(t)e^{\mathbf{A}_{eq}t}$, where $\mathbf{P}_{eq}^{-1}(t)$ is a periodic function. Furthermore, $\dot{\mathbf{x}} = \mathbf{A}(t)\mathbf{x}$ is equivalent in the sense of Lyapunov to $\dot{\mathbf{x}}_{eq} = \mathbf{A}_{eq}\mathbf{x}_{eq}$.

$\mathbf{\Psi}(t)$ is generally not known, so it may be very difficult to find this transformation. The matrix $\mathbf{A}_{eq}$, however, can be found by numerical methods. Consider the linear time-varying dynamical equation (2.14) where we assume [20]

$$\mathbf{A}(t+T) = \mathbf{A}(t) \tag{2.20}$$

for all t and some positive constant T. Let $\mathbf{\Psi}(t)$ be a fundamental matrix of $\dot{\mathbf{x}} = \mathbf{A}(t)\mathbf{x}$. Then $\mathbf{\Psi}(t+T)$ is also a fundamental matrix of $\dot{\mathbf{x}} = \mathbf{A}(t)\mathbf{x}$. This is shown by noting that

$$\dot{\mathbf{\Psi}}(t+T) = \mathbf{A}(t+T)\mathbf{\Psi}(t+T) = \mathbf{A}(t)\mathbf{\Psi}(t+T) \tag{2.21}$$

The matrix function $\mathbf{\Psi}(t)$ is nonsingular for all t; consequently, so is $\mathbf{\Psi}(t+T)$. Hence, there exists a nonsingular constant matrix $\mathbf{F}$ such that

$$\mathbf{\Psi}(t+T) = \mathbf{\Psi}(t)\mathbf{F} \tag{2.22}$$

For the nonsingular matrix $\mathbf{F}$, there exists a constant matrix $\mathbf{A}_{eq}$ such that

$$e^{\mathbf{A}_{eq}T} = \mathbf{F} \tag{2.23}$$

We can take $\mathbf{\Psi}(t)$ to be the identity matrix and numerically (see section 5.2) calculate $\mathbf{F} = \mathbf{\Psi}(t+T)$.

Here a clear advantage of discrete modelling becomes apparent. To get $\mathbf{A}_{eq}$, a matrix logarithm has to be calculated which involves approximation. However, $\mathbf{F}$ is actually the

A-matrix of the sampled-data system obtained by discretization with the time step T. The eigenvalues of $\mathbf{F}$ are called the *Floquet multipliers* of the system. The Poincaré map is an essentially equivalent, geometrical view on this matter, as discussed in the next section.

2.6 Poincaré Map

The stability of any system which is periodic with period T can be studied using the concept of Poincaré map. Suppose a nonlinear dynamical system is given by

$$\dot{\mathbf{x}} = \mathbf{f}(\mathbf{x}) \tag{2.24}$$

An *orbit* based at $\mathbf{x}_0$ is a solution curve of the differential equation (2.24) with the initial condition $\mathbf{x}_0$ at t_0. A point $\mathbf{x}_z$ in the space where $\mathbf{f}$ vanishes, namely $\mathbf{f}(\mathbf{x}_z) = \mathbf{0}$ is called a *fixed point* or *zero*. If an orbit based at a point $\mathbf{x}_0$ in the neighborhood of a zero $\mathbf{x}_z$, tends towards it, $\mathbf{x}(t) \to \mathbf{x}_z$ as $t \to \infty$, then $\mathbf{x}_z$ is said to be asymptotically stable.

Instead of approaching a fixed point, the solution curve of a nonlinear system can move in a *closed* or *periodic* orbit. A periodic solution is one for which there exists $0 < T < \infty$ such that $\mathbf{x}(t) = \mathbf{x}(t+T)$ for all t. The stability of solution curves can be studied in the vicinity of a closed orbit by use of the Poincaré map or advance map. To explain the map in a simple way, consider a dynamical system with three state variables in Fig. 2.11 [50].

γ is a periodic orbit in the 3-dimensional space $\mathbb{R}^3$, where the dimension is the number of state variables. A cross section Σ has been chosen such that γ has an intersection with it at point p_z. Σ is chosen small enough such that p_z is the only intersection. Now choose a neighborhood of p_z in Σ and denote it by ϑ. Note that $\vartheta \subseteq \Sigma$. The *Poincaré map* $\mathrm{PM} : \vartheta \to \Sigma$ for a point $p_0 \in \vartheta$ is defined to be the point $p_1 = \mathrm{PM}(p_0) \in \Sigma$ to which the orbit based at p_0 first returns.

The point p_1, in turn, is mapped into another point $p_2 \in \Sigma$. If the mapping is continued, a set of discrete points in space $(p_0, p_1, p_2, \cdots)$ is obtained. Clearly we have $\mathrm{PM}(p_z) = p_z$. In other words, p_z is a fixed point of the Poincaré map. The stability of the orbits in the vicinity of the periodic orbit based at p_z is determined by the behaviour of the sample points.

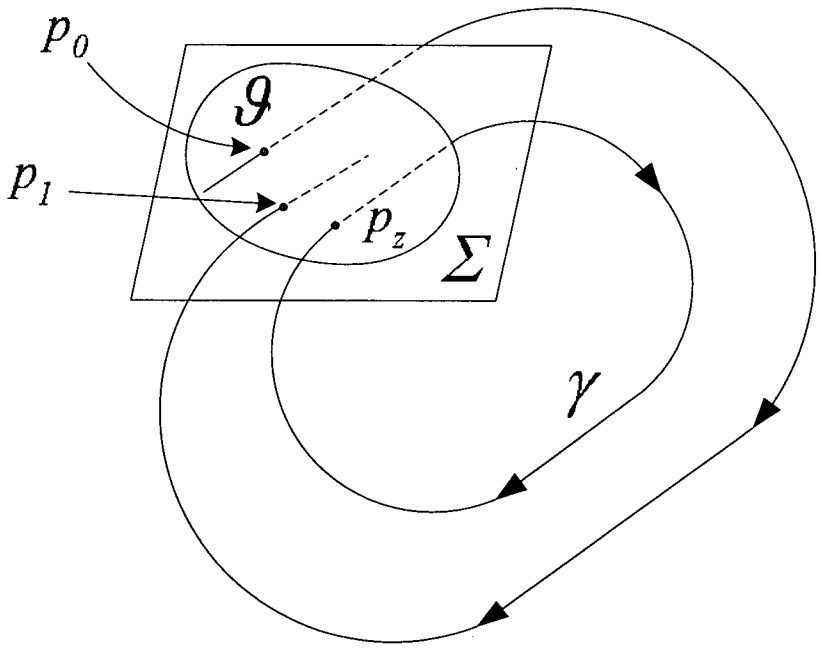

Figure 2.11: Demonstration of the Poincaré map

In the last section, the Floquet multipliers were introduced. In fact, *the eigenvalues of the Jacobian of the linearized Poincaré map are the same as the Floquet multipliers.*

In order to find the Jacobian, equations (2.24) are linearized about the periodic orbit, and then integrated over one period. An excellent treatment of the Poincaré mapping method for stability studies of switching circuits can be found in [51].

The Poincaré map is used in Chapter 5 to derive a linearized sampled-data state-space model for a TCSC compensated system. The map is obtained by integrating the system differential equations, taking into account the changes in equations and coordinates when switchings occur.

In an ideal steady-state condition, a TCSC compensated system returns to its original state after $T = 1/60$ s (corresponding to the synchronous frequency of 60 Hz). However, this time step is too large for implementing an effective damping controller for the instabilities that occur in the range of subsynchronous frequencies. T can be reduced to one-third of that value by taking into account the three-phase symmetry of the network. Reducing the time

step to one-sixth of the synchronous period so that only one current pulse is included in the time span, results in a discrete time-periodic model for the system. However, it is possible to obtain a linear time-invariant model by eliminating the zero-sequence variables. This is discussed in detail in Chapter 5.

2.7 Observer-based Stabilizing Controller

While it is possible to study the stabilizing controllers from a more general standpoint, the observer-based formulation is more relevant to the work presented in Chapter 6 of this thesis, and therefore it is reviewed here. The references for this section are [52, 53, 54].

In a discretized model of the system given by

$$\mathbf{x}(n+1) = \mathbf{A}\mathbf{x}(n) + \mathbf{B}\mathbf{u}(n) \tag{2.25a}$$

$$\mathbf{y}(n) = \mathbf{C}\mathbf{x}(n) + \mathbf{D}\mathbf{u}(n) \tag{2.25b}$$

an eigenvalue of $\mathbf{A}$ lying outside the unit circle, implies internal instability. The control action $\mathbf{u} = -\mathbf{k}\mathbf{x}(n)$ can stabilize the system provided that $[\mathbf{A}\ \mathbf{B}]$ is stabilizable. *Pole placement with full state feedback* is not very practical, however. First, for an n_x-dimensional system, it requires n_x measurements, which, in turn, means n_x transducers. Such a controller would be both expensive and bulky. Further, to be implementable all the states have to be measurable. In a synchronous machine model with a round rotor, the damper windings are not real windings but are used to simulate damper bars and eddy current effects in the iron core of the rotor. Even if a state formulation could be obtained where all states were measurable, it might not be the preferred formulation. Therefore whenever state feedback is considered, normally a *state observer* is also designed to replace the actual state measurements in $\mathbf{u}(n) = -\mathbf{k}\mathbf{x}(n)$ with "observations" $\hat{\mathbf{x}}(n)$ of the states, making the control law $\mathbf{u}(n) = -\mathbf{k}\hat{\mathbf{x}}(n)$. So we are poised to think of a two-stage controller: The first stage is an observer to generate an estimate of the plant's state; the second stage is to feed back this estimate as though it is the state. The observer is in essence a dynamical system with the same number of states as the system it wants to observe. A straightforward way to obtain an observer for the system

in (2.25) is

$$\hat{\mathbf{x}}(n+1) = \mathbf{A}\hat{\mathbf{x}}(n) + \mathbf{B}\mathbf{u}(n) - \mathbf{L}_{ob}[\mathbf{C}\hat{\mathbf{x}}(n) + \mathbf{D}\mathbf{u}(n) - \mathbf{y}(n)] \tag{2.26a}$$

$$\mathbf{y}_{ob}(n) = \hat{\mathbf{x}}(n) \tag{2.26b}$$

If the observer gain $\mathbf{L}_{ob}$ is selected such that the eigenvalues of $\mathbf{A} - \mathbf{L}_{ob}\mathbf{C}$ are within the unit circle, the difference between $\mathbf{x}(n)$ and $\hat{\mathbf{x}}(n)$ approaches zero with time. For fast error dynamics, the gain matrix $\mathbf{L}_{ob}$ must be designed such that the eigenvalues are sufficiently inside the unit circle. For this, the observability of $[\mathbf{A}\ \mathbf{C}]$ is required. Fig. 2.12 shows a plant with the observer in (2.26) and a feedback controller.

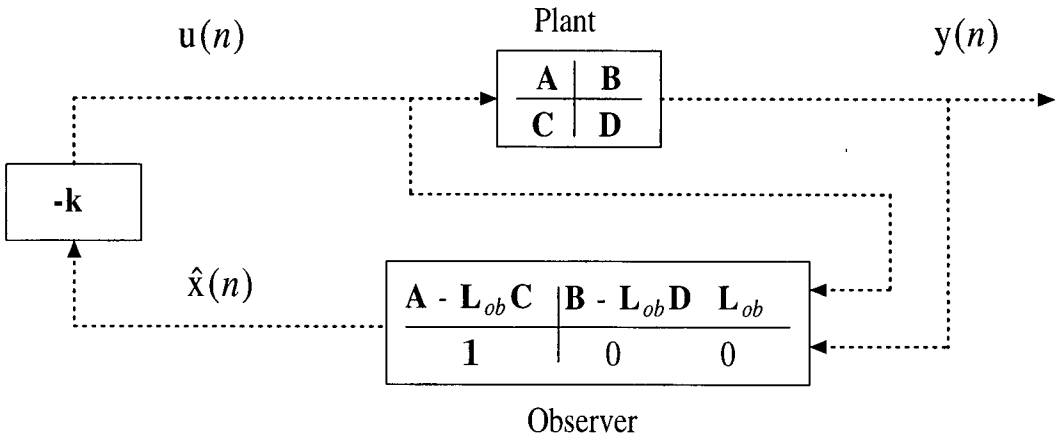

Figure 2.12: Plant and observer

If the measurements of some of the states are available, an observer can be made to estimate only the ones that are not available. In that case the control law becomes $-\mathbf{k}[\hat{\mathbf{x}}_1\ \ \mathbf{x}_2]^t$, where $\hat{\mathbf{x}}_1$ is the vector of the observed states and $\mathbf{x}_2$ is the vector of the measured ones. The observer in Chapter 6 is a partial observer designed to only estimate the states of the turbo-generator.

A systematic approach to the design of observers is Kalman filtering. This method takes into account the uncertainty in the model and the measurements, and has proved very useful in practice. The relations of the discrete Kalman filter are reviewed next.

2.7.1 Discrete Kalman Observer

Suppose the system is governed by linear stochastic difference equations

$$\mathbf{x}(n+1) = \mathbf{A}\mathbf{x}(n) + \mathbf{B}\mathbf{u}(n) + \mathbf{E}\mathbf{w}(n) \tag{2.27a}$$

$$\mathbf{y}(n) = \mathbf{C}\mathbf{x}(n) + \mathbf{D}\mathbf{u}(n) + \mathbf{G}\mathbf{w}(n) + \mathbf{v}(n) \tag{2.27b}$$

where $\mathbf{w}(n)$ is the input or process noise, and $\mathbf{v}(n)$ is the output or measurement noise. They are assumed to be independent random variables, white and with normal probability density functions such that

$$\text{pdf}(\mathbf{w}) = \mathcal{N}(\mathbf{0}, \mathbf{Q}_\mathbf{w}) \tag{2.28}$$

$$\text{pdf}(\mathbf{v}) = \mathcal{N}(\mathbf{0}, \mathbf{R}_\mathbf{v}) \tag{2.29}$$

where $\mathcal{N}(\mathbf{0}, \mathbf{Q}_\mathbf{w})$ means a normal distribution with zero mean and covariance $\mathbf{Q}_\mathbf{w}$. The matrices $\mathbf{Q}_\mathbf{w}$ and $\mathbf{R}_\mathbf{v}$ are the process and measurement noise covariance matrices. *Even if there are no noises or disturbances in the system,* $\mathbf{Q}_\mathbf{w}$ *and* $\mathbf{R}_\mathbf{v}$ *can be used as design parameters to set the gains of the observer* [55]. This is in fact how they are used in Chapter 6, as we do not consider stochastic processes in developing the damping controller for the TCSC compensated system.

Kalman filtering is a method by which we first predict the next state, using the available measurements, and then correct our prediction when the new measurements arrive. So at time n, we have the measurement $\mathbf{y}(n)$ and the prediction we make when we are at time $n-1$, that is $\hat{\mathbf{x}}(n|n-1)$. Eq.(2.30) provides the prediction for the next step. Eq. (2.31) yields the correction $\hat{\mathbf{x}}(n|n)$ which is used to build the control action.

$$\hat{\mathbf{x}}(n+1|n) = \mathbf{A}\hat{\mathbf{x}}(n|n-1) + \mathbf{B}\mathbf{u}(n) + \mathbf{L}_{Kl}[\mathbf{y}(n) - \mathbf{C}\hat{\mathbf{x}}(n|n-1) - \mathbf{D}\mathbf{u}(n)] \tag{2.30}$$

$$\hat{\mathbf{x}}(n|n) = \hat{\mathbf{x}}(n|n-1) + \mathbf{M}_{Kl}[\mathbf{y}(n) - \mathbf{C}\hat{\mathbf{x}}(n|n-1) - \mathbf{D}\mathbf{u}(n)] \tag{2.31}$$

where $\mathbf{L}_{Kl}$ and $\mathbf{M}_{Kl}$ are the gains of the Kalman observer. $\mathbf{M}_{Kl}$ is termed *innovation gain.* Here a general-purpose math package [56] is employed for calculating these gains given the parameters $\mathbf{Q}_\mathbf{w}$ and $\mathbf{R}_\mathbf{v}$.

The equations for the discrete Kalman filter can be represented in the general form of (2.25) as follows

$$\hat{\mathbf{x}}(n+1|n) = (\mathbf{A} - \mathbf{L}_{Kl}\mathbf{C})\hat{\mathbf{x}}(n|n-1) + \begin{bmatrix}\mathbf{B} - \mathbf{L}_{Kl}\mathbf{D} & \mathbf{L}_{Kl}\end{bmatrix} \begin{bmatrix}\mathbf{u}(n) \\ \mathbf{y}(n)\end{bmatrix} \tag{2.32}$$

$$\mathbf{y}_{Kl}(n) = \hat{\mathbf{x}}(n|n) = (\mathbb{1} - \mathbf{M}_{Kl}\mathbf{C})\hat{\mathbf{x}}(n|n-1) + \begin{bmatrix}-\mathbf{M}_{Kl}\mathbf{D} & \mathbf{M}_{Kl}\end{bmatrix} \begin{bmatrix}\mathbf{u}(n) \\ \mathbf{y}(n)\end{bmatrix} \tag{2.33}$$

2.8 Conclusion

This chapter is aimed at providing both a literature overview and a background on the topic of subsynchronous resonance and compensation with thyristor controlled series capacitors.

The physical nature of subsynchronous resonance and its analysis methods are discussed. The Floquet theory and the Poincaré map, two useful concepts equivalent in essence, that enable the eigenanalysis to be extended to switching circuits, are explained in this chapter.

Finally, the theory of observer-based stabilizing feedback controllers is briefly reviewed to be used later in Chapter 6 when the feedback control of TCSC is discussed.

Chapter 3

Subsynchronous Resonance with Fixed Capacitors

The details with which synchronous machines must be modeled depend very much on the type of transient study to be done [57]. In subsynchronous resonance studies, the machine model is much more detailed than for example the models employed for short-circuit, and simplified stability studies.

While it is necessary to involve the detailed models in order to obtain valid results, it helps for educational purposes to take out the not-so-critical details, to arrive at a model which more clearly shows the nature of the interactions taking place.

In this chapter, we introduce a simplified model in order to understand the physical nature of the energy flow into a subsynchronous mode of oscillation. In this respect, first a linear coupled oscillator is studied. Then a fictitious model for SSR is introduced and used to study the flow of energy into the subsynchronous mode. We simplify the system as much as possible, but still keep enough detail to be able to capture the phenomenon of interest.

Having gained insight into the matter, in the last section of the chapter we return to the practical models, and discuss the simulation of the First Subsynchronous Resonance Benchmark Model with fixed series compensation. A standard case is simulated, and linearized for eigenanalysis.

3.1 Linear Coupled Oscillators

Subsynchronous resonance is, in essence, a coupled oscillator problem and in that respect it is informative to make a comparison between it and a well-analyzed coupled oscillator system. Here we choose a simple system of two identical pendulums connected with a spring, as shown in Fig. 3.1, and study the energy transfer in the system.

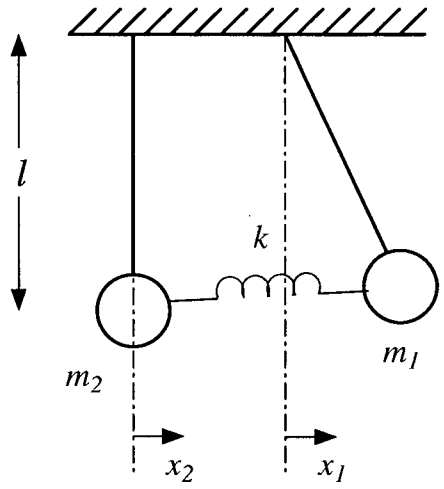

Figure 3.1: Coupled pendulums

If damping is ignored, this system is closed, that is it does not exchange energy with the medium, and therefore its energy content is conserved. The situation depicted in the figure is when one of the pendulums is at rest in its equilibrium point, while the other has been deviated. Upon the release of the pendulums, the energy stored in the mass-spring structure will turn into kinetic energy, most of it being used to accelerate the deviated pendulum. If the coupling is *weak*, that is when the force constant of the coupling spring is small compared to the pendulum constants [58], the energy gradually transfers to the pendulum on the left, increasing its amplitude of oscillation until it comes to a full swing, leaving the first one at rest in the middle. Then the reverse process starts, and in the absense of damping, this back-and-forth energy transfer continues indefinitely. Fig. 3.2 shows the changes in position of the pendulums with time for $m_1 = m_2 = 0.50$ kg, $l = 0.25$ m, and $k = 2.50$ N/m. This is the familiar phenomenon of beats.

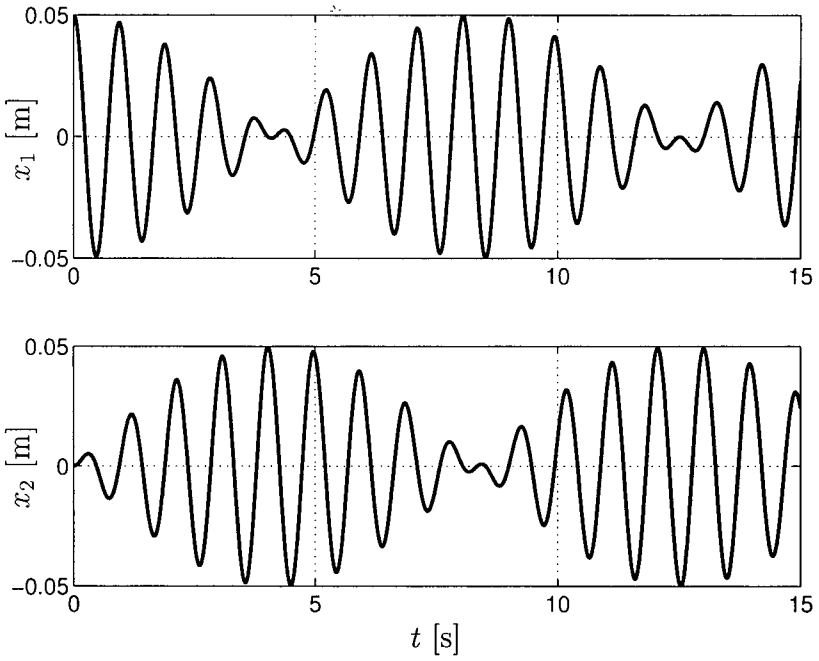

Figure 3.2: Positions of the pendulums

The energy which was once located in one oscillator, is transfered to the other one. Note that although the "location" of energy changes within the system, the modes of oscillation are decoupled and do not exchange energy with each other. To see this more clearly, we write the dynamical equations of the coupled pendulums.

$$\frac{d^2x_1}{dt^2} = -\frac{g_0}{l}x_1 - \frac{k}{m}(x_1 - x_2) \tag{3.1a}$$

$$\frac{d^2x_2}{dt^2} = -\frac{g_0}{l}x_2 + \frac{k}{m}(x_1 - x_2) \tag{3.1b}$$

In (3.1), x_1 and x_2 are the deviations of the pendulums from their equilibrium points, respectively, as shown in Fig. 3.1. The pendulums are assumed to be long enough so that their deviations along the y-axis can be neglected. They have the same length l and the same mass m. g_0 is the gravitational constant. If (3.1a) and (3.1b) are added to and subtracted from each other, we get

$$\frac{d^2}{dt^2}(x_1 + x_2) = -\frac{g_0}{l}(x_1 + x_2) \tag{3.2a}$$

$$\frac{d^2}{dt^2}(x_1 - x_2) = -(\frac{g_0}{l} + \frac{k}{m})(x_1 - x_2) \tag{3.2b}$$

which are the equations of two independent oscillators. $x_1 + x_2$ and $x_1 - x_2$ are the modes of oscillation of the coupled pendulums. With any set of initial conditions, these modes can be

excited. It is also possible to excite only one of them. Suppose both oscillators are deviated exactly the same amount to the right. When they are released, they swing together without exchanging energy with the spring. In this case only the first mode is excited. In another scenario, if the pendulums are deviated the same amount but in the opposite directions, only their differential mode of oscillation is excited.

In a subsynchronous resonance situation we again have two oscillators. Reference [9] has a plot of the mechanical and the electrical torques during a torque amplification process which is similar to the first 5 s in Fig. 3.2. Can we conclude that when SSR happens, energy is transfered to the mechanical oscillator from the electrical one within one mode? That seems to be the case, at least when torque amplification occurs, however a closer examination reveals otherwise. In the next section, we introduce a simplified system in which subsynchronous resonance happens and use it to study the energy transfer in the case of SSR.

3.2 A Simplified Model for SSR Study

Two-phase AC machines give rise to rotating fields very similar in nature to those set up by three-phase machines. The first step in our simplification is therefore to consider a two-phase synchronous machine instead of a three-phase one in which the following assumptions are made [59]:

1. The windings are sinusoidally distributed, so each current-carrying winding produces a sinusoidal magnetic field in the air gap.
2. Permeability of the core is infinite, so the magnetic circuit is linear (no saturation) and the entire magnetic field is concentrated in the air gap.
3. Saliency in the machine is ignored so the magnetic characteristics along the d and q axes are the same.
4. Magnetic flux leakage is ignored. This means that all the flux produced by a winding passes through the core.

With these assumptions it is possible to accurately describe the self and mutual inductances of the machine in terms of its dimensions [59]:

$$L_{W_iW_j} = (N_{W_i}/2)(N_{W_j}/2)\pi\mu_0 r\ell a_g^{-1}\cos(\angle W_iW_j) \tag{3.3}$$

where

N_{W_i}	=	Number of turns of winding i	
μ_0	=	$4\pi 10^{-7}$	Hm^{-1}
r	=	Radius of the rotor	m
ℓ	=	Axial length of the generator rotor	m
a_g	=	Air gap length	m
$\angle W_iW_j$	=	Angle between the axes of windings i and j	rad

Both the self inductance of a winding and the mutual inductance between two windings can be calculated from (3.3). Fig. 3.3 is a pictorial representation of the two-phase machine. The convention of [60] is used, whereby the d axis leads the q axis.

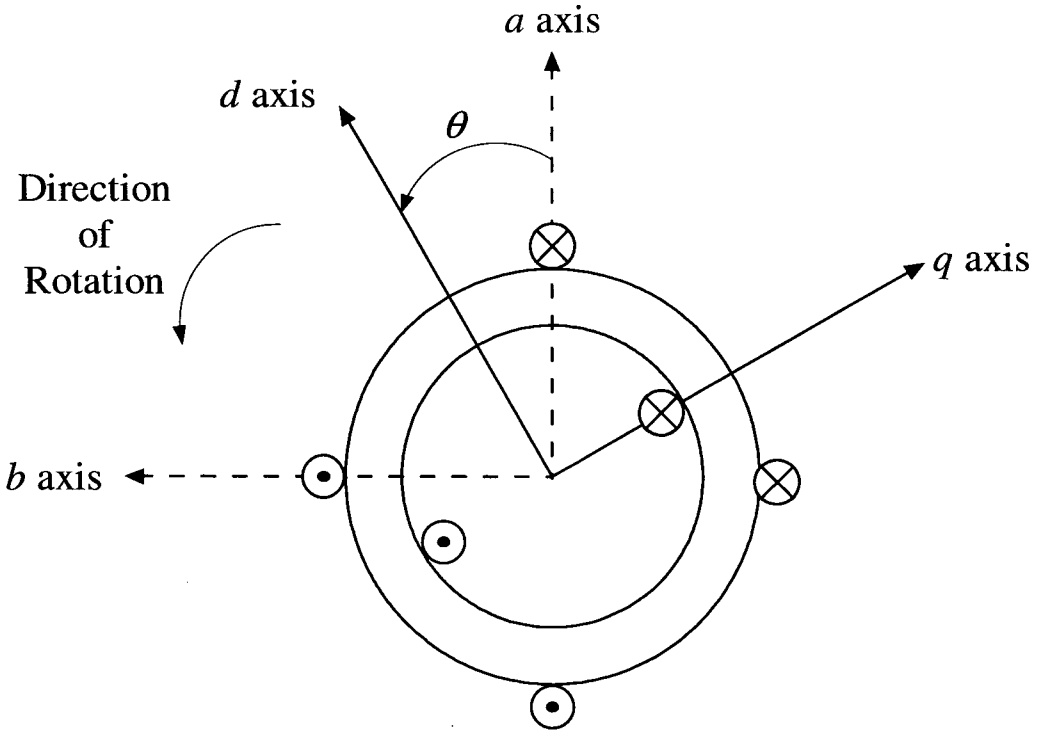

Figure 3.3: Pictorial representation of a two-phase synchronous machine

We write the flux linkage equations for the two stator and one rotor circuits:

$$\psi_a = L_{aa}i_a + L_{ab}i_b + L_{aF}i_F \tag{3.4}$$

$$\psi_b = L_{ba}i_a + L_{bb}i_b + L_{bF}i_F \tag{3.5}$$

$$\psi_F = L_{Fa}i_a + L_{Fb}i_b + L_{FF}i_F \tag{3.6}$$

Since the angle between the two stator windings is 90° and the rotor is round, the mutual coupling, $L_{ab} = L_{ba}$, between them is 0. In this machine only the mutual inductances between the rotor winding and each of the stator windings are variable.

$$\psi_a = L_s i_a + M_F i_F \cos\theta \tag{3.7}$$

$$\psi_b = L_s i_b + M_F i_F \sin\theta \tag{3.8}$$

$$\psi_F = M_F i_a \cos\theta + M_F i_b \sin\theta + L_F i_F \tag{3.9}$$

Note that in our ficticious machine, with all stray inductances neglected, we have

$$M_F^2 = L_s L_F \tag{3.10}$$

In other words, the square of the maximum mutual inductance between the rotor field winding and each of the stator windings is equal to the product of their self-inductances. The schematic of the ficticious machine is shown in Fig. 3.4. Mutual inductances are omitted from the schematic for clarity, but are present with the values determined from (3.3).

Let us write the voltage equations

$$\begin{bmatrix} v_a \\ v_b \\ -v_F \end{bmatrix} = -\begin{bmatrix} R_s & 0 & 0 \\ 0 & R_s & 0 \\ 0 & 0 & R_F \end{bmatrix}\begin{bmatrix} i_a \\ i_b \\ i_F \end{bmatrix} - \begin{bmatrix} \dot{\psi}_a \\ \dot{\psi}_b \\ \dot{\psi}_F \end{bmatrix} \tag{3.11}$$

Using (3.7), (3.8) and (3.9) to write out the flux linkage derivatives in (3.11)we get

$$v_a = -R_s i_a - \dot{\psi}_a = -R_s i_a - L_s\frac{di_a}{dt} - M_F\frac{di_F}{dt}\cos\theta + M_F i_F \omega \sin\theta \tag{3.12}$$

$$v_b = -R_s i_b - \dot{\psi}_b = -R_s i_b - L_s\frac{di_b}{dt} - M_F\frac{di_F}{dt}\sin\theta - M_F i_F \omega \cos\theta \tag{3.13}$$

$$\begin{aligned} -v_F = -R_F i_F - \dot{\psi}_F = -R_F i_F - M_F\frac{di_a}{dt}\cos\theta - M_F\frac{di_b}{dt}\sin\theta - L_F\frac{di_F}{dt} \\ + M_F i_a \omega \sin\theta - M_F i_b \omega \cos\theta \end{aligned} \tag{3.14}$$

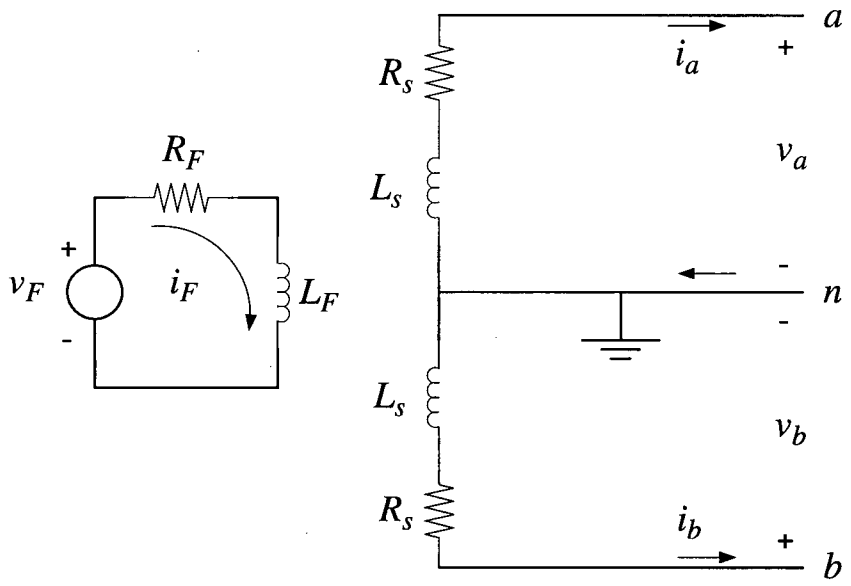

Figure 3.4: Schematic diagram of the ficticious two-phase synchronous machine

A transformation similar to Park's transformation for three-phase machines is used to make the mutual inductances constant

$$\mathbf{P} = \begin{bmatrix} \cos\theta & \sin\theta \\ \sin\theta & -\cos\theta \end{bmatrix} \tag{3.15}$$

where θ is the generator rotor angle. The inverse of $\mathbf{P}$ is $\mathbf{Q} = \mathbf{P}^{-1} = \mathbf{P}$. Applying this transformation to the flux linkages and voltage equations gives

$$\begin{bmatrix} \psi_d \\ \psi_q \\ \psi_F \end{bmatrix} = \begin{bmatrix} L_s & 0 & M_F \\ 0 & L_s & 0 \\ M_F & 0 & L_F \end{bmatrix} \begin{bmatrix} i_d \\ i_q \\ i_F \end{bmatrix} \tag{3.16}$$

$$\begin{bmatrix} v_d \\ v_q \\ -v_F \end{bmatrix} = -\begin{bmatrix} R_s & 0 & 0 \\ 0 & R_s & 0 \\ 0 & 0 & R_F \end{bmatrix} \begin{bmatrix} i_d \\ i_q \\ i_F \end{bmatrix} - \omega \begin{bmatrix} 0 & 1 & 0 \\ -1 & 0 & 0 \\ 0 & 0 & 0 \end{bmatrix} \begin{bmatrix} \psi_d \\ \psi_q \\ \psi_F \end{bmatrix} - \begin{bmatrix} \dot{\psi}_d \\ \dot{\psi}_q \\ \dot{\psi}_F \end{bmatrix} \tag{3.17}$$

Now, suppose the machine is connected to an infinite bus through a series LC circuit, as shown in Fig. 3.5 for phase a.

Writing the Kirchhoff's Voltage Law (KVL) equations for both phases, and transforming the differential equations to the dq frame using (3.15), yields

$$\begin{bmatrix} v_d \\ v_q \end{bmatrix} = \begin{bmatrix} v_{\infty d} \\ v_{\infty q} \end{bmatrix} + \begin{bmatrix} v_{Cd} \\ v_{Cq} \end{bmatrix} + \omega L \begin{bmatrix} 0 & 1 \\ -1 & 0 \end{bmatrix} \begin{bmatrix} i_d \\ i_q \end{bmatrix} + L\frac{d}{dt} \begin{bmatrix} i_d \\ i_q \end{bmatrix} \tag{3.18}$$

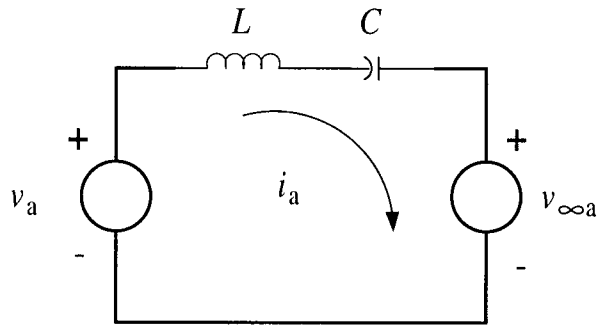

Figure 3.5: External circuit connected to the machine

If the infinite bus voltage is taken to be

$$v_{\infty a}(t) = \sqrt{2}V_\infty \cos(\omega_s t + \alpha_\infty) \tag{3.19}$$

$$v_{\infty b}(t) = \sqrt{2}V_\infty \cos(\omega_s t + \alpha_\infty - \pi/2) \tag{3.20}$$

then we have

$$\begin{bmatrix} v_{\infty d} \\ v_{\infty q} \end{bmatrix} = \sqrt{2}V_\infty \begin{bmatrix} \cos(\delta + \pi/2 - \alpha_\infty) \\ \sin(\delta + \pi/2 - \alpha_\infty) \end{bmatrix} \tag{3.21}$$

where $\delta = \theta - \omega_s t - \pi/2$.

If we define

$$\hat{\mathbf{R}} \triangleq \begin{bmatrix} R_s & 0 & 0 \\ 0 & R_s & 0 \\ 0 & 0 & R_F \end{bmatrix} \tag{3.22}$$

$$\hat{\mathbf{L}} \triangleq \begin{bmatrix} L_s + L & 0 & M_F \\ 0 & L_s + L & 0 \\ M_F & 0 & L_F \end{bmatrix} \tag{3.23}$$

$$\hat{\mathbf{N}} \triangleq \begin{bmatrix} 0 & 1 & 0 \\ -1 & 0 & 0 \\ 0 & 0 & 0 \end{bmatrix} \hat{\mathbf{L}} \tag{3.24}$$

then combining (3.16), (3.17), and (3.18) yields

$$\frac{d}{dt}\begin{bmatrix} i_d \\ i_q \\ i_F \end{bmatrix} = -\hat{\mathbf{L}}^{-1}(\hat{\mathbf{R}} + \omega\hat{\mathbf{N}}) \begin{bmatrix} i_d \\ i_q \\ i_F \end{bmatrix} - \hat{\mathbf{L}}^{-1} \begin{bmatrix} v_{Cd} \\ v_{Cq} \\ 0 \end{bmatrix} - \hat{\mathbf{L}}^{-1} \begin{bmatrix} v_{\infty d} \\ v_{\infty q} \\ -v_F \end{bmatrix} \tag{3.25}$$

Equations (3.25) are the state equations of the currents in the system. Note that since the machine has two phases, and is symmetrical with no stray inductances, the equivalent inductances of the machine in the d-axis and q-axis are equal to a stator self-inductance, $L_d = L_q = L_s$.

The state equations for the capacitor voltages are

$$\frac{d}{dt}\begin{bmatrix} v_{Cd} \\ v_{Cq} \end{bmatrix} = -\omega \begin{bmatrix} 0 & 1 \\ -1 & 0 \end{bmatrix} \begin{bmatrix} v_{Cd} \\ v_{Cq} \end{bmatrix} + \frac{1}{C}\begin{bmatrix} i_d \\ i_q \end{bmatrix} \tag{3.26}$$

Next we obtain the state equations of the mechanical system. The electromagnetic torque is given by

$$t_{qe} = i_q\psi_d - i_d\psi_q = M_F i_F i_q \tag{3.27}$$

We assume that the shaft consists of two rigid rotors, connected through a spring as shown in Fig. 3.6.

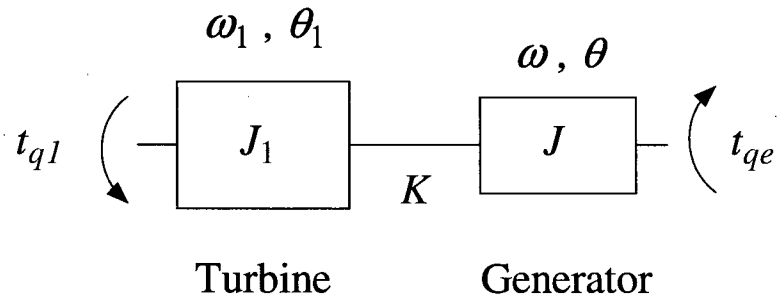

Figure 3.6: Shaft assembly of the simplified model

The differential equations describing the dynamics of the shaft are

$$\frac{d\omega_1}{dt} = -\frac{K}{J_1}\theta_1 + \frac{K}{J_1}\theta + \frac{t_{q1}}{J_1} \tag{3.28a}$$

$$\frac{d\omega}{dt} = +\frac{K}{J}\theta_1 - \frac{K}{J}\theta - \frac{M_F}{J} i_F i_q \tag{3.28b}$$

Equations (3.25)-(3.28) describe the dynamics of the simplified system.

These equations are next used to simulate an example case. We use the parameters from [61] for the simplified system.

K	=	$132.8295 \cdot 10^6$	Nm/rad
J	=	7425.254	kgm^2
J_1	=	13094.151	kgm^2
R_s	=	0.0	Ω
R_F	=	0.702	Ω
L_s	=	3.536	mH
L_F	=	3.226	H
L	=	0.865	H
C	=	26.22	μF
f_s	=	60	Hz
V_a	=	22.0	kV

The isolated shaft system has a natural frequency of 26.65 Hz as determined by eigenvalue analysis. The value of capacitance has been deliberately chosen to give rise to a natural electrical frequency of $60 - 26.65 = 33.35$ Hz. Note that when the equations of the system are referred to the rotor side, the electrical frequencies appear as their complements with respect to the synchronous frequency.

In the simulation results that follow, the generator is switched into an external network which consists only of a capacitor and an inductor in each phase. The infinite voltage source is therefore shorted. The system is nearly closed except for the voltage source and the resistance in the rotor field circuit.

The generator terminal voltage is equal to its rated value of 22.0 kV in the beginning. Using (3.12), and noting that in steady state the first three terms are zero, the steady state field current is obtained as

$$I_F = \frac{\sqrt{2}V_a}{\omega_s M_F} \tag{3.29}$$

which in turn is used to find the field voltage $V_F = R_F I_F$.

Initially, there is no charge on the capacitor plates. Fig. 3.7 shows the speeds of the rotors and Fig. 3.8 the currents of the d and q axes.

The simulation is run for well past the ability of a physical system to take the oscillations before getting damaged. It is evident from Fig. 3.7 and Fig. 3.8 that the energies of the electrical and mechanical oscillations grow simultaneously, and not at the expense of each other. This is unlike the pendulum example that was studied in the previous section.

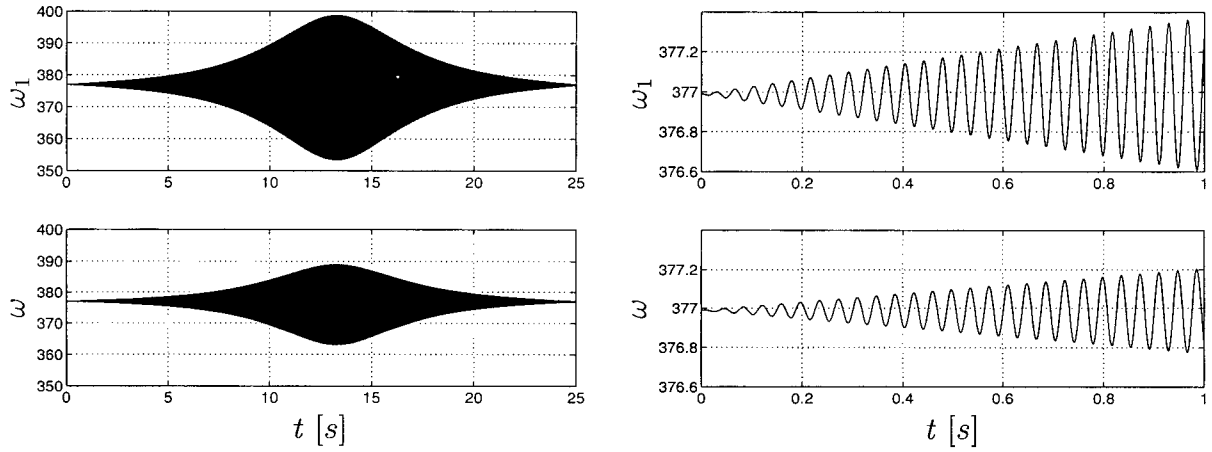

Figure 3.7: Rotor speeds of the two-phase synchronous machine

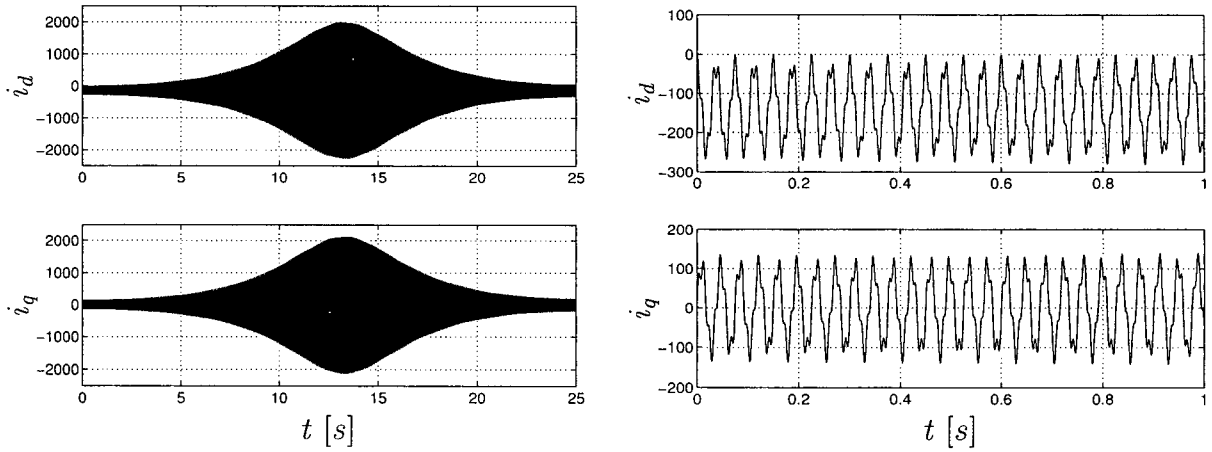

Figure 3.8: Stator currents of the two-phase synchronous machine

Fig. 3.9 shows the kinetic energy of the rotors obtained from

$$E_k(t) = \frac{1}{2}J_1\omega_1^2(t) + \frac{1}{2}J\omega^2(t) \tag{3.30}$$

The energy of the oscillations comes from the kinetic energy of the rotors (which are turning at synchronous speed in the beginning), causing the average rotational speed to drop. Since the rotors are highly massive, a small drop in the average speed is enough to provide the energy of the oscillations even at their peak.

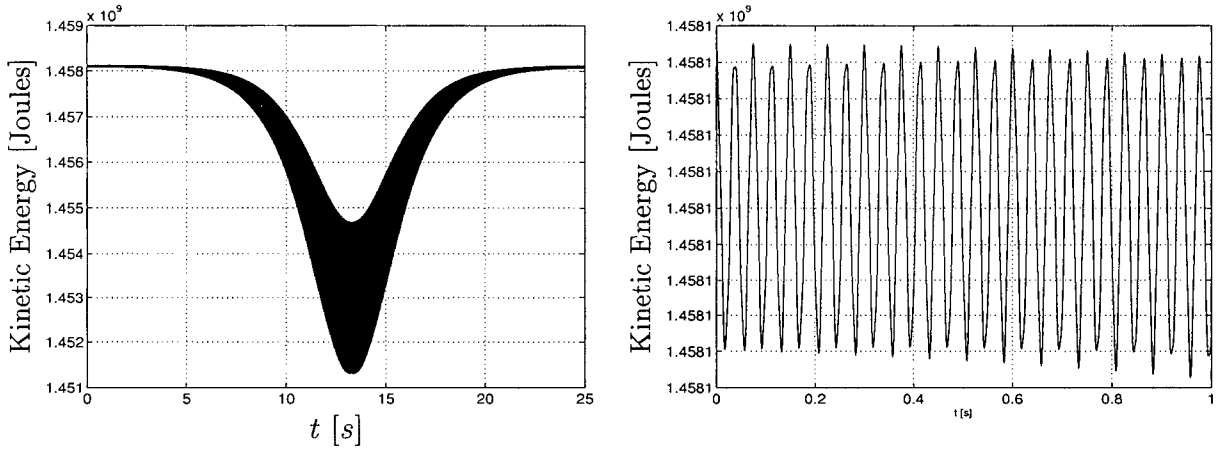

Figure 3.9: Kinetic energy of the rotors

So, during a subsynchronous resonance condition, the energy of a mode of oscillation increases. This energy can come from another mode. The nonlinearity in the system makes this phenomenon possible, since in a linear system the modes are decoupled and do not exchange energy with each other.

3.3 IEEE First SSR Benchmark Model with Fixed Compensation

We choose the First IEEE Subsynchronous Resonance Benchmark Model, referred to as "FBM", to be our test case for the following reasons:

1. This system has 5 subsynchronous modes of oscillation. Therefore it provides flexibility in changing the series compensation level to excite different modes.
2. It has been the major case study in the literature on subsynchronous resonance.
3. Although subsynchronous resonance develops in other configurations as well, the most common and severe case is when a synchronous generator is radially connected to the network by a series compensated transmission line.

This section discusses the FBM parameters, its nonlinear dynamical equations, and eigenvalue analysis for a standard case with fixed series compensation to prepare for the more involved analysis with thyristor controlled compensation in later chapters.

The dynamical equations of the FBM with thyristor controlled series compensation are given in Appendix B, and linearized in Chapter 5. To avoid repetition here, whenever the equations are the same or similar, reference is made to the appropriate location.

The external network of phase a with a fixed capacitor is shown in Fig. 3.10, where $R_{a_{tot}}$ and $L_{a_{tot}}$ denote the total resistances and inductances of the transformer, the line and the infinite bus in phase a, respectively. There are also mutual resistance and inductance between the phases that are not shown in the figure.

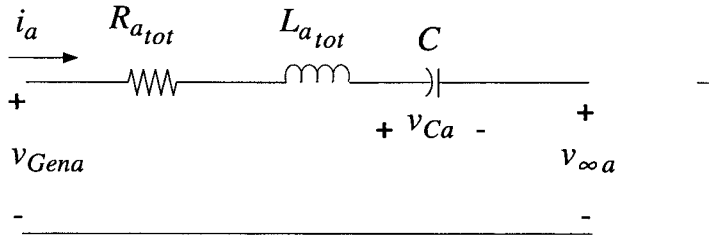

Figure 3.10: The external network connected to the turbo-generator in FBM

Since the system has three-phase symmetry the resistance and inductance are the same in all phases. Furthermore, the mutual components between any two phases are equal. If the mutual elements are denoted by $R_{ab_{tot}}$ and $L_{ab_{tot}}$, then the differential equations of the three-phase network become

$$\begin{bmatrix} v_{Gena} \\ v_{Genb} \\ v_{Genc} \end{bmatrix} - \begin{bmatrix} v_{\infty a} \\ v_{\infty b} \\ v_{\infty c} \end{bmatrix} = \begin{bmatrix} R_{a_{tot}} & R_{ab_{tot}} & R_{ab_{tot}} \\ R_{ab_{tot}} & R_{a_{tot}} & R_{ab_{tot}} \\ R_{ab_{tot}} & R_{ab_{tot}} & R_{a_{tot}} \end{bmatrix} \begin{bmatrix} i_a \\ i_b \\ i_c \end{bmatrix} + \begin{bmatrix} L_{a_{tot}} & L_{ab_{tot}} & L_{ab_{tot}} \\ L_{ab_{tot}} & L_{a_{tot}} & L_{ab_{tot}} \\ L_{ab_{tot}} & L_{ab_{tot}} & L_{a_{tot}} \end{bmatrix} \frac{d}{dt} \begin{bmatrix} i_a \\ i_b \\ i_c \end{bmatrix} + \begin{bmatrix} v_{Ca} \\ v_{Cb} \\ v_{Cc} \end{bmatrix} \tag{3.31}$$

In FBM the parameters of the transformer, the line, and the infinite bus are given in terms of symmetrical components. A three-phase balanced inductance matrix

$$\begin{bmatrix} L_a & L_{ab} & L_{ab} \\ L_{ab} & L_a & L_{ab} \\ L_{ab} & L_{ab} & L_a \end{bmatrix} \tag{3.32}$$

becomes

$$\begin{bmatrix} L_a + 2L_{ab} & 0 & 0 \\ 0 & L_a - L_{ab} & 0 \\ 0 & 0 & L_a - L_{ab} \end{bmatrix} \tag{3.33}$$

when the system phasors are transformed into the symmetrical components. Having (3.33), it is straightforward to obtain the self and mutual parameters for each of the network components in order to build the matrices in (3.31).

We write (3.31) in the compact form

$$\mathbf{v}_{Gen,abc} - \mathbf{v}_{\infty,abc} = \mathbf{R}\mathbf{i}_{abc} + \mathbf{L}\frac{d}{dt}\mathbf{i}_{abc} + \mathbf{v}_{C,abc} \tag{3.34}$$

These equations are next transformed into the $0dq$ reference frame by use of the power-invariant Park transformation

$$\mathbf{P}(\theta) = \sqrt{2/3}\begin{bmatrix} 1/\sqrt{2} & 1/\sqrt{2} & 1/\sqrt{2} \\ \cos\theta & \cos(\theta - 2\pi/3) & \cos(\theta + 2\pi/3) \\ \sin\theta & \sin(\theta - 2\pi/3) & \sin(\theta + 2\pi/3) \end{bmatrix} \tag{3.35}$$

where θ is the angular position of the generator rotor, defined to be the position of the d-axis of the rotor with respect to the axis of phase a winding of the stator. The inverse of $\mathbf{P}$ is denoted by $\mathbf{Q}$, and is equal to the transpose of $\mathbf{P}$, that is $\mathbf{Q} = \mathbf{P}^{-1} = \mathbf{P}^t$. The transformed equations of the external network in (3.34) are in the form

$$\mathbf{v}_{Gen,0dq} - \mathbf{v}_{\infty,0dq} = \mathbf{PRQ}\mathbf{i}_{0dq} + \mathbf{PLQ}\left(\frac{d}{dt}\mathbf{i}_{0dq} - \frac{d\mathbf{P}}{dt}\mathbf{Q}\mathbf{i}_{0dq}\right) + \mathbf{v}_{C,0dq} \tag{3.36}$$

PRQ and **PLQ** again have the general form given in (3.33). Therefore, when working in $0dq$ reference frame, the symmetrical components can be readily used. Also note that

$$\frac{d\mathbf{P}}{dt}\mathbf{Q} = -\mathbf{P}\frac{d\mathbf{Q}}{dt} = \omega\begin{bmatrix} 0 & 0 & 0 \\ 0 & 0 & -1 \\ 0 & 1 & 0 \end{bmatrix} \triangleq \omega\mathbf{M} \tag{3.37}$$

where ω is the angular speed of the generator rotor. Since time is in per unit with the base $t_B = 1/\omega_B$ s, the form of equations in actual quantities and in per unit are the same.

The generator terminal voltages $\mathbf{v}_{Gen,0dq}$ can be expressed in terms of the synchronous machine stator and rotor currents. The zero axis, direct axis, and quadrature axis equivalent circuits of a synchronous generator with four rotor windings are shown in Fig. 3.11, Fig. 3.12, and Fig. 3.13, respectively. The rotor windings on the direct axis are denoted by 'F' and 'D', and those on the quadrature axis are denoted by 'Q' and 'G'.

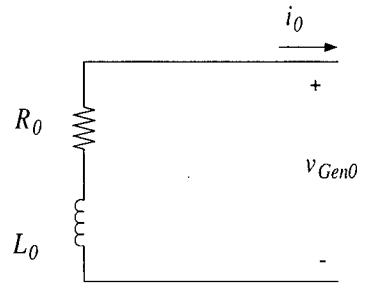

Figure 3.11: 0-axis circuit of the synchronous generator

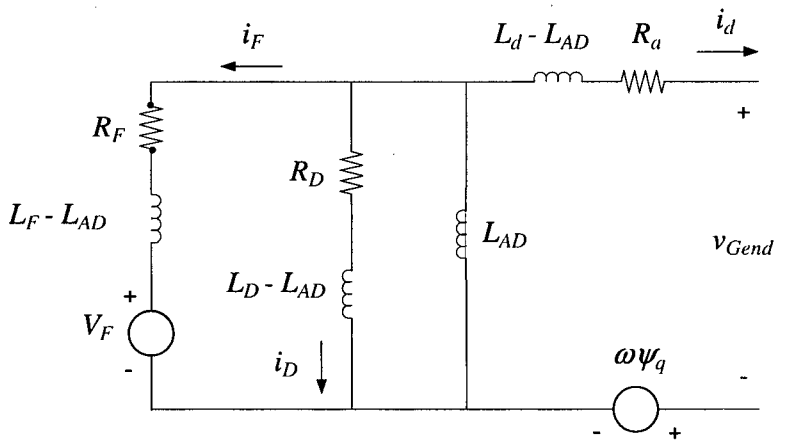

Figure 3.12: d-axis circuit of the synchronous generator

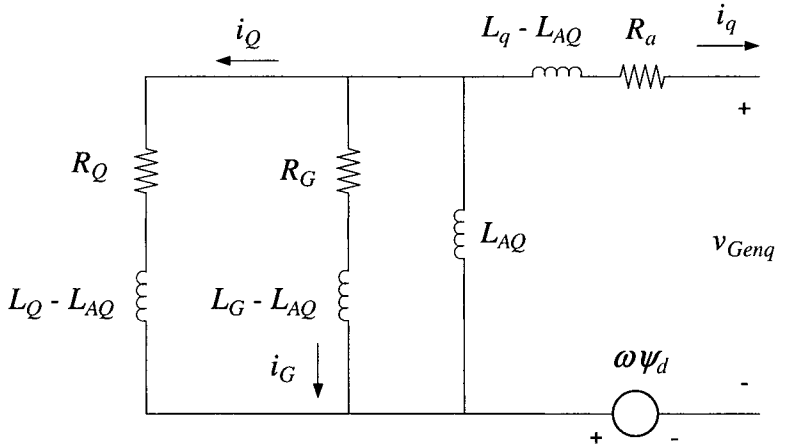

Figure 3.13: q-axis circuit of the synchronous generator

In Fig. 3.12 and Fig. 3.13, the flux linkages ψ_d and ψ_q are

$$\psi_d = L_d i_d + L_{AD} i_F + L_{AD} i_D \tag{3.38}$$

$$\psi_q = L_q i_q + L_{AQ} i_Q + L_{AQ} i_G \tag{3.39}$$

The differential equations of the synchronous generator are given below. These equations can be derived from the equivalent circuits.

$$\begin{bmatrix} v_{Gen0} \\ v_{Gend} \\ v_{Genq} \\ -V_F \\ 0 \\ 0 \\ 0 \end{bmatrix} = - \begin{bmatrix} R_0 & 0 & 0 & 0 & 0 & 0 & 0 \\ 0 & R_a & \omega L_q & 0 & 0 & \omega L_{AQ} & \omega L_{AQ} \\ 0 & -\omega L_d & R_a & -\omega L_{AD} & -\omega L_{AD} & 0 & 0 \\ 0 & 0 & 0 & R_F & 0 & 0 & 0 \\ 0 & 0 & 0 & 0 & R_D & 0 & 0 \\ 0 & 0 & 0 & 0 & 0 & R_Q & 0 \\ 0 & 0 & 0 & 0 & 0 & 0 & R_G \end{bmatrix} \begin{bmatrix} i_0 \\ i_d \\ i_q \\ i_F \\ i_D \\ i_Q \\ i_G \end{bmatrix}$$

$$- \begin{bmatrix} L_0 & 0 & 0 & 0 & 0 & 0 & 0 \\ 0 & L_d & 0 & L_{AD} & L_{AD} & 0 & 0 \\ 0 & 0 & L_q & 0 & 0 & L_{AQ} & L_{AQ} \\ 0 & L_{AD} & 0 & L_F & L_{AD} & 0 & 0 \\ 0 & L_{AD} & 0 & L_{AD} & L_D & 0 & 0 \\ 0 & 0 & L_{AQ} & 0 & 0 & L_Q & L_{AQ} \\ 0 & 0 & L_{AQ} & 0 & 0 & L_{AQ} & L_G \end{bmatrix} \frac{d}{dt} \begin{bmatrix} i_0 \\ i_d \\ i_q \\ i_F \\ i_D \\ i_Q \\ i_G \end{bmatrix} \tag{3.40}$$

Using the notation defined in Appendix B, (3.40) is written in the following compact form.

$$\begin{bmatrix} \mathbf{v}_{Gen,0dq} \\ -\mathbf{v}_{FDQG} \end{bmatrix} = - \begin{bmatrix} \mathbf{R}_{0dq} - \omega \mathbf{M} \mathbf{L}_{0dq} & -\omega \mathbf{M} \mathbf{L}_{SR} \\ \mathbf{0}_{4\times 3} & \mathbf{R}_{FDQG} \end{bmatrix} \begin{bmatrix} \mathbf{i}_{0dq} \\ \mathbf{i}_{FDQG} \end{bmatrix} - \begin{bmatrix} \mathbf{L}_{0dq} & \mathbf{L}_{SR} \\ \mathbf{L}_{SR}^t & \mathbf{L}_R \end{bmatrix} \frac{d}{dt} \begin{bmatrix} \mathbf{i}_{0dq} \\ \mathbf{i}_{FDQG} \end{bmatrix} \tag{3.41}$$

The last step to obtain the current equations is to substitute $\mathbf{v}_{Gen,0dq}$ in (3.41) using the external network equations in (3.36), and rearranging the terms. The final result is

$$\begin{bmatrix} \dot{\mathbf{i}}_{0dq} \\ \dot{\mathbf{i}}_{FDQG} \end{bmatrix} = \hat{\mathbf{L}}^{-1}(\omega \hat{\mathbf{N}} - \hat{\mathbf{R}}) \begin{bmatrix} \mathbf{i}_{0dq} \\ \mathbf{i}_{FDQG} \end{bmatrix} - \hat{\mathbf{L}}^{-1} \begin{bmatrix} \mathbf{v}_{C,0dq} \\ \mathbf{0}_{4\times 1} \end{bmatrix} - \hat{\mathbf{L}}^{-1} \begin{bmatrix} \mathbf{v}_{\infty,0dq} \\ -\mathbf{v}_{FDQG} \end{bmatrix} \tag{3.42}$$

where the variables $\hat{\mathbf{L}}$, $\hat{\mathbf{N}}$, and $\hat{\mathbf{R}}$ are defined in Appendix B.

The differential equations for the capacitor voltages are the same as given in (B.16).

Also, the mechanical differential equations do not alter when the series compensation is changed from fixed to thyristor controlled. These equations are given in (B.25) and (B.26). The shaft has 5 natural subsynchronous modes with frequencies given in Table 3.1.

Table 3.1: Mechanical modal frequencies of the IEEE First SSR Benchmark Model

Mode	Frequency [Hz]
TM1	15.71
TM2	20.21
TM3	25.55
TM4	32.28
TM5	47.45

The mechanical dampings in FBM are given in terms of modal dampings indicated by damping decrements. Theoretically, any set of modal dampings can be converted to equivalent self and mutual dampings by means of the reverse transformation from the modal domain to the spring-mass domain [18]. Unfortunately, such a reverse transformation leads to mutual dampings between not only the adjacent elements, but among all elements irrespective of their physical location on the shaft. The spring-mass model does not provide for these fictitious mutual damping elements, but represents mutual damping only between adjacent elements. To be able to use the modal dampings in the mass-spring model, [18] introduces a parameter fitting technique, called "*modal adjustment*", that we review next.

3.3.1 Approximate Method to Calculate Self-Dampings

The spring-mass model can be adjusted to simulate the measured modal dampings as long as the damping adjustments are relatively small. In the following an approximate method is described for making these adjustments.

The dynamics of the turbine-generator shaft are given by

$$\mathbf{J}\ddot{\theta} + \mathbf{D}\dot{\theta} + \mathbf{K}\theta = \mathbf{t_q} \tag{3.43}$$

where $\mathbf{J}$ is the diagonal inertia matrix, $\mathbf{D}$ is the diagonal damping matrix, and $\mathbf{K}$ is the non-diagonal spring constant matrix either in per unit or in actual quantities.

The reason why $\mathbf{D}$ is diagonal, is that we are not considering the shaft damping between adjacent masses. These dampings are smaller than the dampings to reference and can often be neglected [18]. If these dampings are not neglected, then $\mathbf{D}$ will become a tri-diagonal

matrix. The modal decomposition can still be performed in this general case. Note that $\mathbf{D}$ is unknown, and has to be determined from the modal dampings.

Since $\mathbf{K}$ is not diagonal, equations (3.43) are not decoupled. However, there always exists an equivalence transformation that decouples this system. The dampings, $\mathbf{D}$, are unknown but small, therefore in finding the transformation matrix, we neglect them, and consider the system as

$$\mathbf{J}\ddot{\boldsymbol{\theta}} + \mathbf{K}\boldsymbol{\theta} = \mathbf{t_q} \tag{3.44}$$

or

$$\ddot{\boldsymbol{\theta}} + \mathbf{J}^{-1}\mathbf{K}\boldsymbol{\theta} = \mathbf{J}^{-1}\mathbf{t_q} \tag{3.45}$$

Suppose we denote the equivalence transformation by $\mathbf{P}_{mod}$, then

$$\boldsymbol{\theta}_{mod} = \mathbf{P}_{mod}\boldsymbol{\theta} \tag{3.46}$$

Applying this transformation to (3.45) yields

$$\mathbf{P}_{mod}\ddot{\boldsymbol{\theta}} + \mathbf{P}_{mod}\mathbf{J}^{-1}\mathbf{K}\boldsymbol{\theta} = \mathbf{P}_{mod}\mathbf{J}^{-1}\mathbf{t_q} \tag{3.47}$$

or

$$\ddot{\boldsymbol{\theta}}_{mod} + (\mathbf{P}_{mod}\mathbf{J}^{-1}\mathbf{K}\mathbf{P}_{mod}^{-1})\boldsymbol{\theta}_{mod} = (\mathbf{P}_{mod}\mathbf{J}^{-1})\mathbf{t_q} \tag{3.48}$$

The second term on the left-hand side of (3.48) has to be diagonal in order for the equations to be decoupled. Therefore the transformation matrix we are seeking is actually one that diagonalizes $\mathbf{J}^{-1}\mathbf{K}$. This transformation consists of the mode shapes (eigenvectors) of $\mathbf{J}^{-1}\mathbf{K}$ as its columns.

Having obtained $\mathbf{P}_{mod}$, we now turn our attention to the dampings. The modal dampings are obtained from the self dampings by

$$\mathbf{D}_{mod} = \mathbf{P}_{mod}\mathbf{D}\mathbf{P}_{mod}^{-1} \tag{3.49}$$

where $\mathbf{D}_{mod}$ is the diagonal matrix of modal dampings. In FBM the modal dampings are given in terms of damping decrements, indicated in the Appendix B by *md*. The relation between a damping decrement and a modal damping is given by

$$md_i = \frac{D_{imod}}{2J_{imod}} \tag{3.50}$$

where J_{imod} is the modal moment of inertia. Similar to (3.49), the relation between the modal moments of inertia and actual moments of inertia is $\mathbf{J}_{mod} = \mathbf{P}_{mod}\mathbf{J}\mathbf{P}_{mod}^{-1}$. Since we neglected the dampings in finding $\mathbf{P}_{mod}$, the non-diagonal elements of (3.49) may be nonzero. However, we only consider the diagonal elements. If $\mathbf{P}_{mod}$ is given by

$$\mathbf{P}_{mod} = \begin{bmatrix} p_{11} & p_{12} & \cdots & p_{1n_m} \\ p_{21} & p_{22} & \cdots & p_{2n_m} \\ \vdots & \vdots & \ddots & \vdots \\ p_{n_m1} & p_{n_m2} & \cdots & p_{n_mn_m} \end{bmatrix} \tag{3.51}$$

where n_m is the number of masses, then it can be shown that the i^{th} diagonal term of the transformation in (3.49) is

$$D_{imod} = D_1p_{1i}^2 + D_2p_{2i}^2 + \cdots + D_{n_m}p_{n_mi}^2 \tag{3.52}$$

Finally the equations that determine the self dampings from the modal dampings, D_{imod} $i = 1, 2, \cdots, n_m$, are

$$\begin{bmatrix} p_{11}^2 & p_{21}^2 & \cdots & p_{n_m1}^2 \\ p_{12}^2 & p_{22}^2 & \cdots & p_{n_m2}^2 \\ \vdots & \vdots & \ddots & \vdots \\ p_{1n_m}^2 & p_{2n_m}^2 & \cdots & p_{n_mn_m}^2 \end{bmatrix} \begin{bmatrix} D_1 \\ D_2 \\ \vdots \\ D_{n_m} \end{bmatrix} = \begin{bmatrix} D_{1mod} \\ D_{2mod} \\ \vdots \\ D_{n_mmod} \end{bmatrix} \tag{3.53}$$

Equation (3.53) is used in this thesis to obtain the self dampings from the modal damping specifications. If a modal damping is not given, its value is assigned zero. Some of the dampings calculated this way may come out to be negative, which are clearly fictitious values. This does not however pose a problem for the eigenvalue analysis [18].

3.3.2 Analysis of a Standard Case

In order to test the validity of the dynamical equations of the system, as obtained above, here we use them to simulate the standard case 1-T of the FBM [38].

The reactance of the series compensation, $X_C = 0.371$ pu, is tuned approximately to 40 Hz both during and after the fault to excite the second torsional mode TM2 with frequency 20.21 Hz. The fault is a three-phase to ground short circuit at busbar B (Fig. 2.4). The prefault voltage in phase a is zero. The reactance of the fault is taken to be 0.04 pu. The fault clearing process starts at 0.075 s after the fault, with each phase opening at the next occuring line current zero-crossing. During the fault, the system dynamical equations are changed. This is taken into account in the simulation.

Fig. 3.14 shows the electromagnetic torque, and two of the shaft torques for 0.5 s. MATLAB® differential equation solver ODE15s is used for the simulation. The curves are in agreement with those provided by [38].

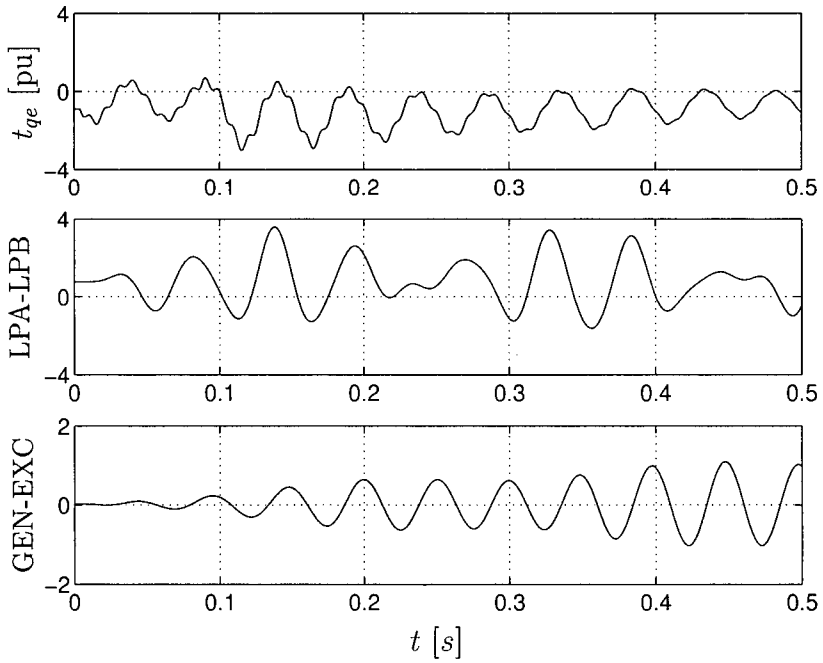

Figure 3.14: Torques in FBM Case 1-T

Eigenvalue analysis requires the nonlinear equations to be linearized first. The equations of the FBM with partly fixed and partly thyristor controlled compensation are linearized for different switch combinations in Section 5.3. To obtain the Jacobian for fixed compensation, it suffices to omit the rows and columns pertaining to the TCSC voltages in (5.31), (5.32), and (5.33). Note that the Jacobian is the **A**-matrix of the continuous linearized system.

Fig. 3.15 shows the movement of the eigenvalues in the s-plane when compensation is

varied from 30% to 90%. The arrows indicate the direction of increasing compensation. Only the first 4 subsynchronous modes are shown; the change in TM5 is small. The case of $X_C = 0.371$ pu is indicated by a dot on the curves. It is seen that at this particular compensation level, the largest undamping is that of TM2, and therefore it is the dominant unstable mode.

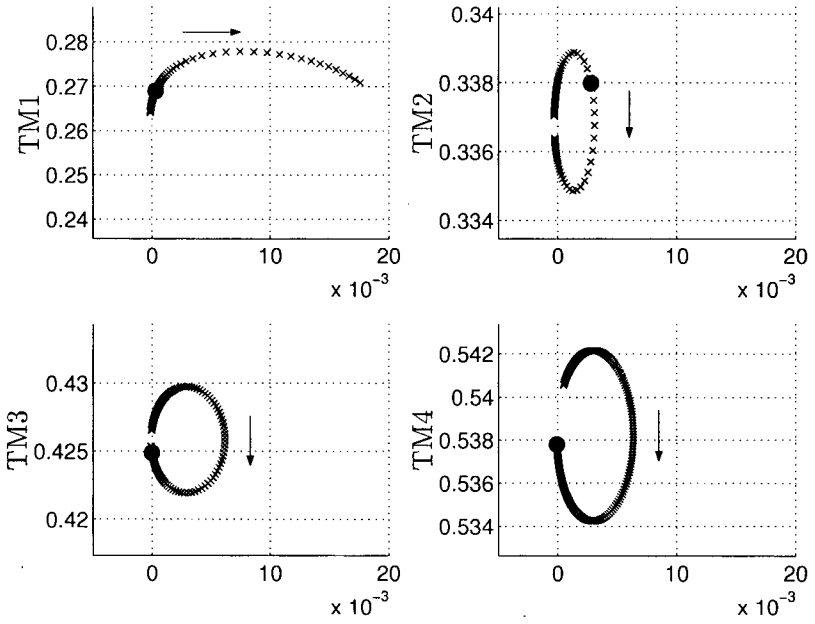

Figure 3.15: Movement of the eigenvalues in the s-plane with compensation level

3.4 Conclusion

In this chapter the transient, nonlinear simulation of the subsynchronous resonance is discussed with both simplified and detailed models.

The comparison of the simplified system with a linear coupled-oscillator reveals that the nature of energy flow into the subsynchronous modes of oscillation is more complicated, and relies on the nonlinearity of the system. When a subsynchronous mode is self-excited, the energy of both the mechanical and the electrical oscillations increases, while in the case of the linear coupled oscillators the energy content in each mode is constant.

Since the First Subsynchronous Resonance Benchmark Model is the chosen test case in this thesis, in the last section, the parameters and dynamical equations of this system are

studied. The approximate method, by means of which the modal damping decrements are transferred into self-dampings is explained. The standard case 1-T in [38] is simulated to insure that the derivation is correct.

Finally, the shift of the eigenvalues of the linearized system with compensation level is shown. Since the linearized model is continuous, the eigenvalues are plotted in the s-plane.

In the following chapters, where the series compensation is partly fixed and partly thyristor controlled, the linearized model is discrete. Therefore the eigenvalues are plotted in the z-plane, and their position relative to the unit circle determines their stability.

Chapter 4

Passive Damping of Thyristor Controlled Series Capacitor

A point of contention is the nature of the response of a TCSC to disturbances at subsynchronous frequencies. Specifically, it has been shown that a TCSC operating in open loop possesses a resistive characteristic at subsynchronous frequencies [25, 27]. This result is surprising since a TCSC with ideal switches does not have any resistive element. So the question is then posed as to the whereabouts of the energy dissipated in the calculated resistance. Note that the commutation of thyristors in a TCSC is not forced, and therefore no energy loss can be attributed to it. In other words, an ideal thyristor in a TCSC turns off when it is not carrying current, so at the time of turning off, there is no energy stored in the inductor in the corresponding thyristor branch.

Here we investigate the source of this resistance, and suggest a way to compute it when a periodic steady state exists or can be approximately assumed for the circuit. The calculated resistance is compared with that by another method, proposed to obtain the frequency response of TCSC, which also yields a resistive component at each subsynchronous frequency.

Then, three open-loop firing schemes are compared with respect to the impedance they present to subsynchronous currents.

Finally, the dynamic model of a single-phase TCSC based on the linearization of the

Poincaré map is tested for accuracy in capturing the passive damping.

4.1 Fundamental Concepts

When a circuit consisting only of passive elements responds to a current waveform $i(t)$ applied to its terminals with a voltage waveform $v(t)$, then (as is well known), the instantaneous power consumed by the circuit is given by

$$p(t) = v(t)i(t) \tag{4.1}$$

Now, suppose the current and the voltage are both periodic with period T. Then the equivalent resistance of the circuit is calculated by

$$R_{eq} = \frac{< p(t) >_T}{I^2} = \frac{\frac{1}{T}\int_T v(\eta)i(\eta)d\eta}{\frac{1}{T}\int_T i^2(\eta)d\eta} \tag{4.2}$$

I is the rms value of the periodic current. The only requirement on the current and voltage is that they both be periodic with a common period. If in (4.2), instead of the total current, a purely sinusoidal component with period T_i (obtained from Fourier analysis) is used, then R_{eq} can be taken as the equivalent resistance at the corresponding frequency. Note that T/T_i is an integer. We make use of this point in interpreting the behaviour of a TCSC at a single frequency.

4.2 Method of Resistance Calculation

In order to study the behaviour of TCSC at a subsynchronus frequency consider Fig. 4.1, where a single-phase TCSC is shown to be injected by a current of the form

$$i(t) = \sqrt{2}I_s \sin(\omega_s t + \gamma_s) + \sqrt{2}I_h \sin(\omega_h t + \gamma_h) \tag{4.3}$$

The magnitude of the subharmonic current, I_h, is much less than the magnitude of the synchronous current, I_s, and the disturbance in the line current does not drive the TCSC out of its normal operation. Therefore, small signal analysis is applicable.

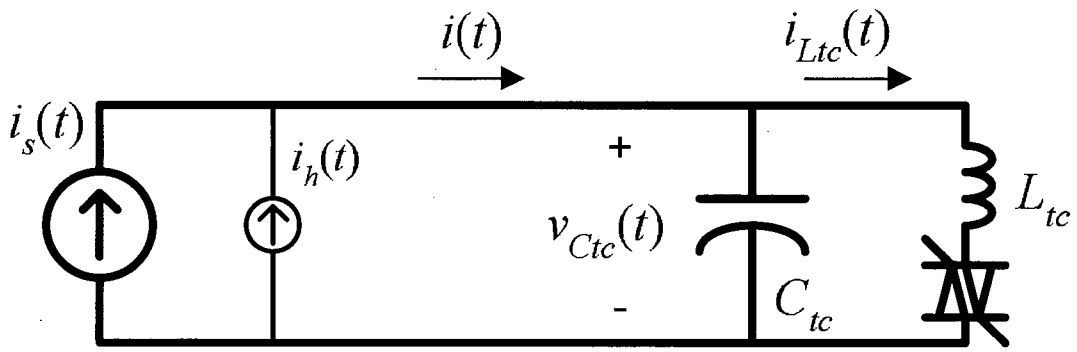

Figure 4.1: A single-phase TCSC

A current of the form (4.3) is not necessarily periodic. For example, it would not be periodic for $\omega_s = 2\pi 60$ rad/s and $\omega_h = 100$ rad/s. Here, however, we choose to work with frequencies that result in a periodic current waveform. The justification is that for any irrational number, there exists a sufficiently close rational number. Therefore, theoretically, using frequencies whose ratio is rational does not prevent the analysis being done with any desired precision.

Another issue, which is more important from a practical point of view, is that the period of the waveform in (4.3) can be much longer than the period of its constituent sinusoids. Take for example $\omega_s = 2\pi 60$ rad/s and $\omega_h = 2\pi 47$ rad/s. The periods of the corresponding sinusoids are $1/60 \cong 0.0167$ s and $1/47 \cong 0.0213$ s, while the period of their summation is 1.0 s.

If $i(t)$ results in a periodic voltage waveform across the TCSC terminals with the same period as that of the current, or a rational ratio of it, we can use (4.2) to calculate the total equivalent resistance of the TCSC. A firm statement about the periodicity of the voltage is formidable however, for two reasons:

1. The behaviour of the TCSC depends on the firing policy, and a result obtained for one policy is not necessarily valid for another.
2. The waveform in (4.3) can have a very long period, which means we may need to take into account a great number of switchings in order to firmly validate the periodicity.

Let us analyze the open-loop firing with respect to the zero crossings of the current waveform in (4.3). With this assumption, the firing system is unaware of the subsynchronous

current, and looks for the zero crossing in the total current to send the gate pulse after a fixed time $(\alpha - \pi/2)/\omega_s$, α being the firing angle by definition calculated from the zero crossing of the capacitor voltage. As an example, take $f_s = 60$ Hz and $f_h = 47$ Hz. The current waveform repeats after 1 s. The smallest possible period for $v_{Ctc}(t)$ is therefore 1 s. So at least 120 current pulses have to be considered to see if $v_{Ctc}(t+1)$ and $dv_{Ctc}(t+1)/dt$ are equal to $v_{Ctc}(t)$ and $dv_{Ctc}(t)/dt$ for a chosen set of initial conditions.

The differential equations of the system are analytically solved for the 'on' and 'off' states separately. Suppose the gate pulse is sent at t_{on} and the inductive branch immediately starts to conduct until its current passes through zero. Then the inductor current, $i_{Ltc}(t)$, and the capacitor voltage, $v_{Ctc}(t)$, during this time are

$$i_{Ltc}(t) = k_1 \cos\omega_{Ntc}(t - t_{on}) + k_2 \sin\omega_{Ntc}(t - t_{on}) + \frac{\omega_{Ntc}^2}{\omega_{Ntc}^2 - \omega_s^2}\sqrt{2}I_s \sin(\omega_s t + \gamma_s) + \frac{\omega_{Ntc}^2}{\omega_{Ntc}^2 - \omega_h^2}\sqrt{2}I_h \sin(\omega_h t + \gamma_h) \tag{4.4}$$

$$v_{Ctc}(t) = L_{tc}\frac{di_{Ltc}}{dt} = -k_1\omega_{Ntc}L_{tc}\sin\omega_{Ntc}(t - t_{on}) + k_2\omega_{Ntc}L_{tc}\cos\omega_{Ntc}(t - t_{on}) + \frac{\omega_{Ntc}^2\omega_s L_{tc}}{\omega_{Ntc}^2 - \omega_s^2}\sqrt{2}I_s \cos(\omega_s t + \gamma_s) + \frac{\omega_{Ntc}^2\omega_h L_{tc}}{\omega_{Ntc}^2 - \omega_h^2}\sqrt{2}I_h \cos(\omega_h t + \gamma_h) \tag{4.5}$$

where

$$\omega_{Ntc} = \frac{1}{\sqrt{L_{tc}C_{tc}}} \tag{4.6}$$

$$k_1 = \frac{\omega_{Ntc}^2\sqrt{2}I_s \sin(\omega_s t_{on} + \gamma_s)}{\omega_s^2 - \omega_{Ntc}^2} + \frac{\omega_{Ntc}^2\sqrt{2}I_h \sin(\omega_h t_{on} + \gamma_h)}{\omega_h^2 - \omega_{Ntc}^2} \tag{4.7}$$

$$k_2 = \frac{v_{Ctc}(t_{on})}{\omega_{Ntc}L_{tc}} + \frac{\omega_{Ntc}\omega_s\sqrt{2}I_s \cos(\omega_s t_{on} + \gamma_s)}{\omega_s^2 - \omega_{Ntc}^2} + \frac{\omega_{Ntc}\omega_h\sqrt{2}I_h \cos(\omega_h t_{on} + \gamma_h)}{\omega_h^2 - \omega_{Ntc}^2} \tag{4.8}$$

If an 'off' state starts at t_{off}, then the capacitor voltage from this time until the time when the inductive branch comes back to the circuit is

$$v_{Ctc}(t) = -\frac{\sqrt{2}I_s}{\omega_s C_{tc}}\cos(\omega_s t + \gamma_s) - \frac{\sqrt{2}I_h}{\omega_h C_{tc}}\cos(\omega_h t + \gamma_h) + k_3 \tag{4.9}$$

$$k_3 = v_{Ctc}(t_{off}) + \frac{\sqrt{2}I_s}{\omega_s C_{tc}} \cos(\omega_s t_{off} + \gamma_s) + \frac{\sqrt{2}I_h}{\omega_h C_{tc}} \cos(\omega_h t_{off} + \gamma_h) \tag{4.10}$$

With a set of initial conditions, equations (4.4)-(4.10) are solved successively to see if at the end of 1 s we return to the conditions which existed at the beginning of the simulation. Instead of going through the cumbersome procedure of iteration with different sets of initial conditions, we start with zero initial conditions and simulate long enough until the circuit achieves steady state. Although there is no resistance in the circuit, the discontinuous mode of operation helps to eliminate the transient response owing to the natural frequency ω_{Ntc}. This is checked for the example case in the next section, before proceeding with the resistance calculation.

4.3 Numerical Example

To be able to make comparisons, the TCSC in [62] is used as an example. The parameters are

$$L_{tc} = 7.0 \quad \text{mH} \tag{4.11a}$$

$$C_{tc} = 500 \quad \mu\text{F} \tag{4.11b}$$

$$f_s = 60 \quad \text{Hz} \tag{4.11c}$$

$$f_h = 47 \quad \text{Hz} \tag{4.11d}$$

$$\sigma = 80^\circ \tag{4.11e}$$

The conduction angle σ, corresponds to a firing angle $\alpha = 180 - \sigma/2 = 140^\circ$ (the delay from the zero crossing of the current becomes $140^\circ - 90^\circ = 50^\circ$). The injected current is chosen as

$$i(t) = \underbrace{\sin(2\pi 60 + \pi/2)}_{i_s(t)} + \underbrace{0.1\sin(2\pi 47)}_{i_h(t)} \tag{4.12}$$

In the simulation results that follow, a 50 μs time step is used. An iterative procedure is employed to improve the accuracy of the zero crossing instants to $\pm 10^{-12}$ s. Simulation is

started with zero initial conditions and allowed to run for over 1.6 s. The code is written in MATLAB®. Fig. 4.2 shows the capacitor voltage in two time spans that are apart by 1 s.

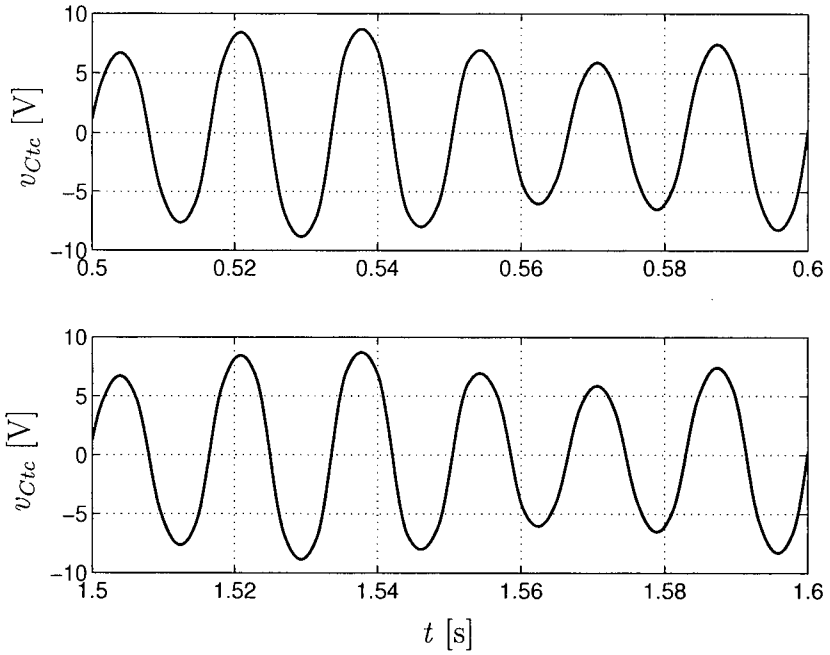

Figure 4.2: Capacitor voltage in two time spans apart by 1 s

The mean of the difference between the two waveforms in Fig. 4.2 is in the order of 10^{-13} V. Therefore for our purpose, v_{Ctc} has achieved the state of periodicity and we can apply (4.2) to the waveforms in $t \in [0.5\ 1.5]$ s.

The total resistance of the TCSC to the current in (4.12) is found to be

$$R_{eq} = \frac{\int_{0.5}^{1.5} v_{Ctc}(\eta)[i_s(\eta) + i_h(\eta)]d\eta}{I_s^2 + I_h^2} = 3.31 \cdot 10^{-8} \qquad \Omega \tag{4.13}$$

This value is less than the accuracy of the calculation. Therefore, it is not significant and can be assumed to be zero. However, when only the subsynchronous current is taken into account, we get

$$R_h = \frac{\int_{0.5}^{1.5} v_{Ctc}(\eta) i_h(\eta) d\eta}{I_h^2} = 4.6338 \qquad \Omega \tag{4.14}$$

Also, with only the synchronous current,

$$R_s = \frac{\int_{0.5}^{1.5} v_{Ctc}(\eta) i_s(\eta) d\eta}{I_s^2} = -0.0463 \qquad \Omega \tag{4.15}$$

So the resistance at 47 Hz is obtained at the expense of a slightly negative resistance at 60 Hz. Now, let us compare the results just obtained with FFT analysis results. Fig. 4.3 shows the FFT of v_{Ctc} and i.

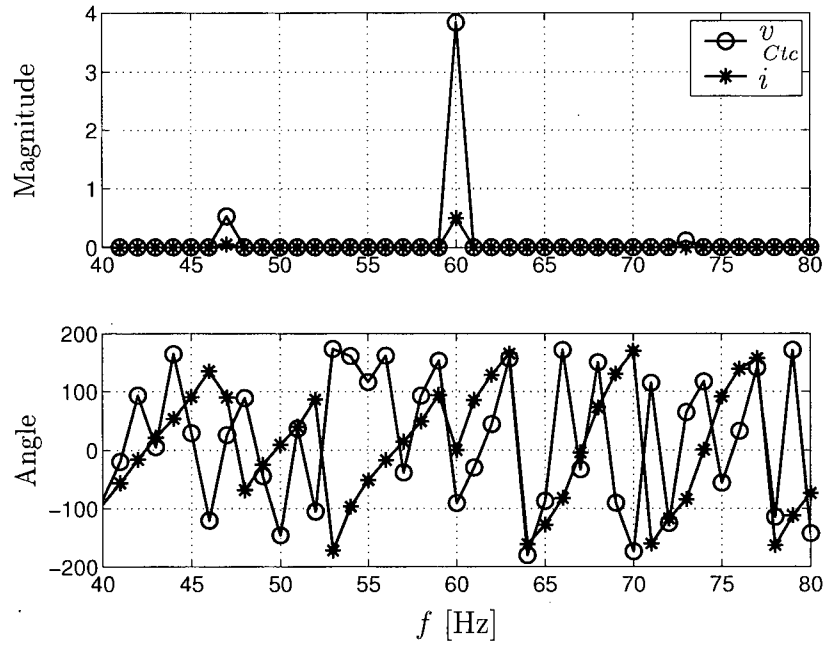

Figure 4.3: FFT of the capacitor voltage and the line current

The FFT of the current has elements with nonzero magnitude only at 47 Hz and 60 Hz, as expected. A close examination of the FFT shows that the voltage and the current components at these two frequencies are

$$\boldsymbol{V}_{47} = 0.52768e^{j26.0445} \tag{4.16a}$$

$$\boldsymbol{I}_{47} = 0.05e^{j90} \tag{4.16b}$$

$$\boldsymbol{V}_{60} = 3.83648e^{-j90.346} \tag{4.16c}$$

$$\boldsymbol{I}_{60} = 0.5e^{j0} \tag{4.16d}$$

So the resistance values calculated from FFT components become

$$R_{47} = \mathrm{Re}\left\{\frac{\boldsymbol{V}_{47}}{\boldsymbol{I}_{47}}\right\} = \quad 4.6338 \qquad \Omega \tag{4.17}$$

$$R_{60} = \mathrm{Re}\left\{\frac{\boldsymbol{V}_{60}}{\boldsymbol{I}_{60}}\right\} = -0.0463 \qquad \Omega \tag{4.18}$$

which are in perfect agreement with the results obtained in (4.14) and (4.15).

A method for obtaining the frequency response of a TCSC is proposed in [62], which implies a different way of calculating resistance, based on the assumption that the steady-state turn-on and turn-off instants of a thyristor in a TCSC are not altered by the small-signal subharmonic current. Hence the linearity principle applies, and the effect of a subsynchronous current source can be investigated, once the other sources are set to zero. A synchronously varying resistor is used to replace the thyristor. This method allows for the forced commutation of the inductor current, which is a *dissipating* action in nature, and as a result, no negative resistance is observed at synchronous frequency. Fig. 4.4 shows the variation in the capacitor voltage and inductor current for the TCSC parameters in (4.11). The occurrence of forced commutation is evident. The current used for the simulation is

$$i_h(t) = 0.1\cos(2\pi 47t) \tag{4.19}$$

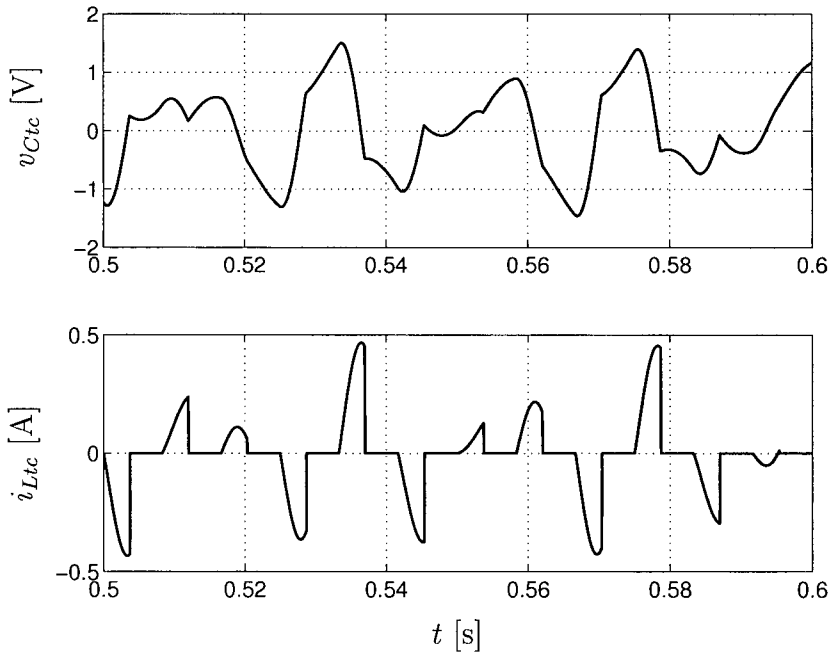

Figure 4.4: Sample of v_{Ctc} and i_{Ltc} from the method of [62]

The resistance of the thyristor during 'on' and 'off' states is assumed to be 10^{-6} and 10^{10} Ω, respectively. The resistance at 47 Hz is found by FFT analysis from

$$\boldsymbol{V}_{47} = 0.4526e^{j160.90} \tag{4.20a}$$

$$\boldsymbol{I}_{47} = 0.05e^{-j180} \tag{4.20b}$$

to be

$$R_{47} = \mathrm{Re}\left\{\frac{\boldsymbol{V}_{47}}{\boldsymbol{I}_{47}}\right\} = 8.5540 \qquad \Omega \tag{4.21}$$

The difference, between the value of resistance in this case and the value of resistance obtained before, can be explained by the fact that the source of resistance is completely different in the two cases.

4.4 Frequency Response Curves of TCSC

The resistance observed at a subsynchronous frequency is a virtual resistance that appears because of the switching action in the device. It is, therefore, in order to ask how the resistance changes with the conduction angle and the firing policy used.

Fig. 4.5 shows the changes observed in resistance as a function of frequency at certain conduction angles for the test circuit and the TCSC with L and C of (4.11). The numbers given in the legend are the conduction angles in degrees. The reactance is also given to make the plots more useful for subsynchronous resonance studies. Capacitive reactance is shown as positive, hence the label 'Cap. React.'. To obtain these plots, the frequency of the disturbance current is varied over the range of 5 Hz to 115 Hz in steps of 1 Hz, and the simulation is allowed to run for 1.5 s in each case. The accuracy of the zero crossing detection is enhanced by an iterative procedure. Then the FFT of the waveforms in the time span of [0.5 1.5] s is used to obtain the resistance and the reactance. The time step used for the simulation is increased to 500 μs, with the resulting Nyquist frequency of 1000 Hz, which is still enough for accuracy in the range of frequencies plotted in the figure.

The firing policy used so far to obtain the previous results is to send the pulse gate to the positive polarity thyristor, $(\alpha - \pi/2)/\omega_s$ s after detecting the positive-to-negative zero crossing in the line current, and vice versa. With this policy, the device acts as a capacitive reactance, together with resistance on the subsynchronous disturbances. Here, the following two firing methods are examined and compared with the former:

1. Gate pulse to the positive thyristor is sent α/ω_s s after the negative-to-positive zero crossing in the capacitor voltage and vice versa.

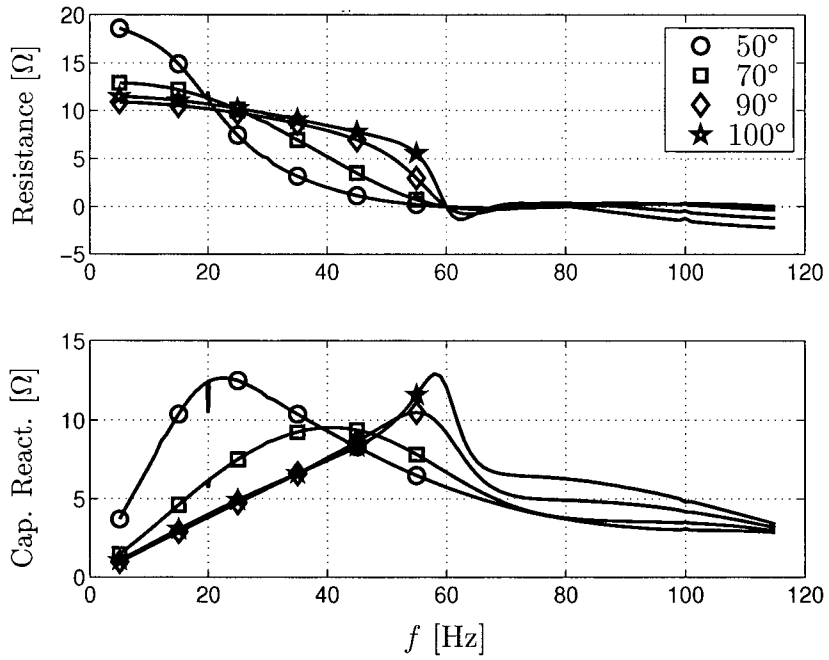

Figure 4.5: Frequency response curves for the TCSC in (4.11)

2. Gate pulse to the positive polarity thyristor is sent $(\alpha + \pi/2)/\omega_s$ s after the negative-to-positive zero crossing in the line current and vice versa.

Fig. 4.6 shows the plots of resistance and reactance at a 90° conduction angle with the above three open-loop firing policies. In Fig. 4.6, 'Cpn' denotes firing with respect to the positive-to-negative zero crossing in the line current, while 'Vnp' is with respect to the negative-to-positive zero crossing in the voltage, and 'Cnp' is with respect to the negative-to-positive zero crossing in the line current. It is interesting to note that the resistance becomes negative for frequencies below 12 Hz for the 'Cnp' policy. For these frequencies, the resistance observed at the synchronous frequency is positive, which leads to the same result obtained before, namely that the total energy consumption by the device is zero.

The resemblance of the frequency response to that of a parallel LC circuit is most pronounced for the 'Vnp' scheme.

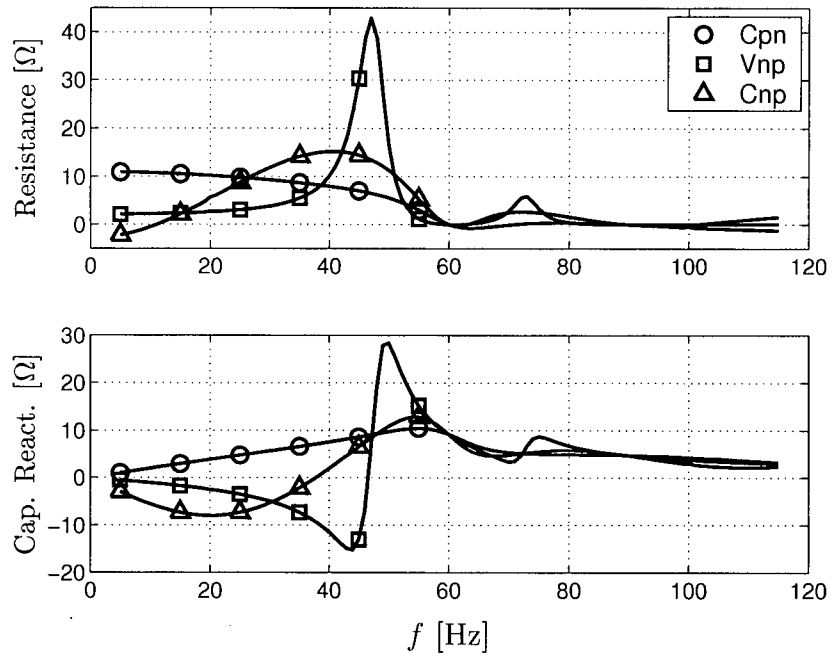

Figure 4.6: Frequency response curves for $\sigma = 90°$ and different firing policies

4.5 Passive Damping in TCSC Dynamic Models

The existing dynamic models developed for small signal analysis of TCSC fall into one of two categories [27]:

1. Linearization of the average steady-state or power flow model.
2. Linearization of the Poincaré map.

In the first approach, the thyristor-controlled inductive branch is replaced by an equivalent linear inductor which in parallel with C_{tc} gives the same compensation level at the synchronous frequency. This method fails to capture the passive resistive behaviour of the TCSC. The eigenvalues of the linear model lie on the imaginary axis of the s-plane and the TCSC shows an undamped response to subsynchronous excitations.

In Chapter 2, it was stated that the dynamics of any system which is periodic with period T can be studied by sampling the system state once per period [45]. The system dynamics are described by the discrete model that maps the change in the sampled states from one sampled point to the next. This concept is formalized as the Poincaré map from the dynamical systems theory. Linearization of the Poincaré map incorporates a resistive

behaviour. The question is how this resistive behaviour compares to the resistance calculated by power considerations.

The discrete model for a single-phase TCSC, obtained by linearization of the Poincaré map, is derived in Appendix A, and is given by (A.15). For convenience, the relation is repeated here.

$$\Delta v_{Ctc}(k\pi+\pi) = \cos\kappa\bar{\sigma}\Delta v_{Ctc}(k\pi) + (-1)^k\alpha_\phi\Delta\phi + \frac{1}{\omega_s C_{tc}}\cos\kappa\bar{\sigma}\int_{k\pi}^{k\pi+\bar{\phi}}\Delta i(\eta)d\eta + \frac{1}{\omega_s C_{tc}}\int_{k\pi+\bar{\phi}}^{k\pi+\bar{\tau}}\cos[\kappa(k\pi+\bar{\tau}-\eta)]\Delta i(\eta)d\eta + \frac{1}{\omega_s C_{tc}}\int_{k\pi+\bar{\tau}}^{k\pi+\pi}\Delta i(\eta)d\eta \tag{A.15}$$

This map basically predicts the small signal change in the capacitor voltage sample taken after π rad, $\Delta v_{Ctc}(k\pi+\pi)$, given the small signal change in the present sample, $\Delta v_{Ctc}(k\pi)$, the small signal change in the firing angle, $\Delta\phi$, for the firing that happens at some instant between $k\pi$ rad and $k\pi+\pi$ rad, and the small signal variation of the line current during $k\pi \le \omega_s t \le k\pi+\pi$. For the meaning of other variables see Appendix A.

Notice that the Jacobian of the Poincaré map, alias the **A**-matrix of this linear model, is $\cos\kappa\bar{\sigma} < 1$. Therefore, the model has an eigenvalue inside the unit circle, which means that the model shows damping.

In the derivation of (A.15), the half wave symmetry of the TCSC waveforms has been exploited to reduce the advance map to half the period, thereby reducing the amount of calculations. $\Delta\phi$ and $\Delta i(\cdot)$ are the inputs.

The complexity of the map with regard to Δi is because in the differential equations from which (A.15) is derived, the line current i is the forcing function.

References [27, 32] have assumed that the small signal variation of the current, $\Delta i(t)$, is given by $\Delta i_d \cos\omega_s t - \Delta i_q \sin\omega_s t$, with Δi_d and Δi_q constant (zero-order hold). That is, the input expressed in terms of Δi_d and Δi_q remains constant between two sampled points. This assumption has been made to be able to simplify the map and convert the linear model from discrete to continuous time. However, it reduces the accuracy of the model.

Here, we rather stay in the discrete domain and are more concerned about the accuracy, therefore this assumption is relaxed. For a detailed derivation of the continuous-time models for TCSC in the dq-reference frame see [27, 32].

The model in (A.15) is linear. The linearity with respect to $\Delta v_{Ctc}(k\pi)$, and $\Delta\phi$ is evident. To see the linearity with respect to $\Delta i(\cdot)$, take two current waveforms $\Delta i^{(1)}(\cdot)$ and $\Delta i^{(2)}(\cdot)$; $k\pi \leq \omega_s t \leq k\pi + \pi$, and denote the response of (A.15) to each of them by $y_1 = \Delta v^{(1)}_{Ctc}(k\pi + \pi)$ and $y_2 = \Delta v^{(2)}_{Ctc}(k\pi + \pi)$, respectively. Then it is straightforward to show that the response to $a_1\Delta i^{(1)}(\cdot) + a_2\Delta i^{(2)}(\cdot)$ is $a_1 y_1 + a_2 y_2$, where a_1 and a_2 are two real numbers.

The linearity means that if the input Δi is a sinusoidal current, the steady-state output points (after transients have died) should also lie on a sinusoid, with the same frequency. On the other hand, (A.15) is supposed to portray the small-signal behaviour of the TCSC at subsynchronous frequencies. Therefore, if $\Delta i(t) = I_h \sin(\omega_h t + \gamma_h)$, then the sample points must lie on the voltage component of TCSC with the same frequency.

The voltage components of the TCSC voltage at different frequencies are obtained by Fourier analysis. Both the magnitude and phase of each frequency component are determined by FFT. Note that the virtual resistance of the TCSC is basically a phase shift between the voltage and current at a subsynchronous frequency. If the disturbance $\Delta i(t)$ is applied to (A.15), and the resultant sample points lie on the subsynchronous voltage component, then the discrete model captures the correct resistance at that frequency. In the following, this point is investigated for the example considered in Section 4.3.

When Δi is a sinusoid, the integrals in (A.15) can be computed analytically. To use (A.15), $\Delta\phi$ needs to be determined as well. Note that the firing of TCSC is done with respect to the line current zero-crossings. Suppose t_z is the time at which the line current passes through zero, and that the steady-state current is denoted by i^* such that

$$i(t) = i^*(t) + \Delta i(t) \tag{4.22}$$

With the time origin for the waveforms assumed as in the Appendix A, we have $i^*(t) = \sqrt{2} I_s \sin(\omega_s t + \pi)$. Fig. 4.7 shows a situation where the zero-crossing in the line current is shifted to the right with respect to the zero-crossing in the steady-state current i^*. Without

the disturbance Δi, the zero-crossing at $\omega_s \bar{t}_z = k\pi$ is used for setting the firing time immediately after $k\pi$ (synchronization with the line current). With the disturbance, when the zero-crossing at t_z is detected, a gate pulse is sent to the appropriate thyristor after a fixed time corresponding to the angle $\phi = \omega_s t_z - \pi/2 + \alpha$, thus $\Delta\phi = \omega_s \Delta t_z$. Therefore

$$t_z = \bar{t}_z + \frac{\Delta\phi}{\omega_s} = k\pi + \frac{\Delta\phi}{\omega_s} \tag{4.23}$$

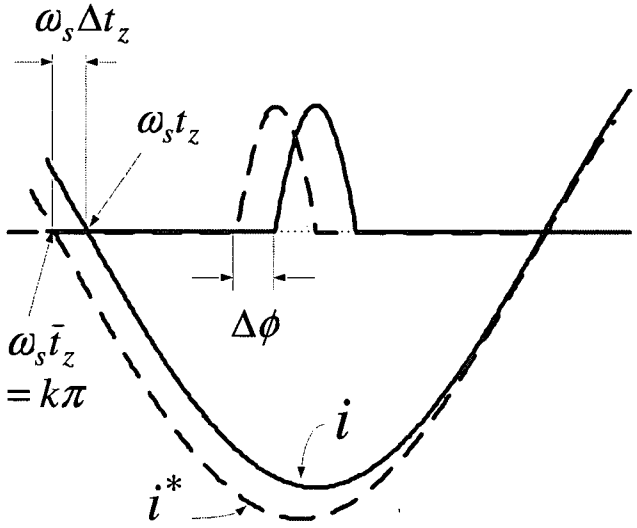

Figure 4.7: Change of firing instant with disturbance in the line current

With the disturbance as given in (4.3), we now substitute $t = t_z$ to obtain

$$i(t_z) = i^*(\bar{t}_z + \frac{\Delta\phi}{\omega_s}) + \Delta i(\bar{t}_z + \frac{\Delta\phi}{\omega_s}) = 0 \tag{4.24}$$

or

$$\sqrt{2} I_s \sin(k\pi + \Delta\phi + \pi) + \sqrt{2} I_h \sin(\frac{\omega_h}{\omega_s}(k\pi + \Delta\phi) + \gamma_h) = 0 \tag{4.25}$$

Linearization of (4.25) based on the small-signal assumption yields

$$\Delta\phi \approx (-1)^k \frac{I_h}{I_s} \sin(\frac{\omega_h}{\omega_s} k\pi + \gamma_h) \tag{4.26}$$

Fig. 4.8 shows the 47 Hz component of the capacitor voltage, $\boldsymbol{V}_{47}$, obtained from FFT analysis, together with the sample points obtained by applying the disturbance, $i_h(t)$ in

(4.12) to (A.15). The TCSC parameters are those given in Section 4.3. The sample points follow the waveform very closely, which is an indication of the accuracy of the model. The waveform of the current is also given for comparison. Note that the phase shift between the current and voltage is not exactly 90°.

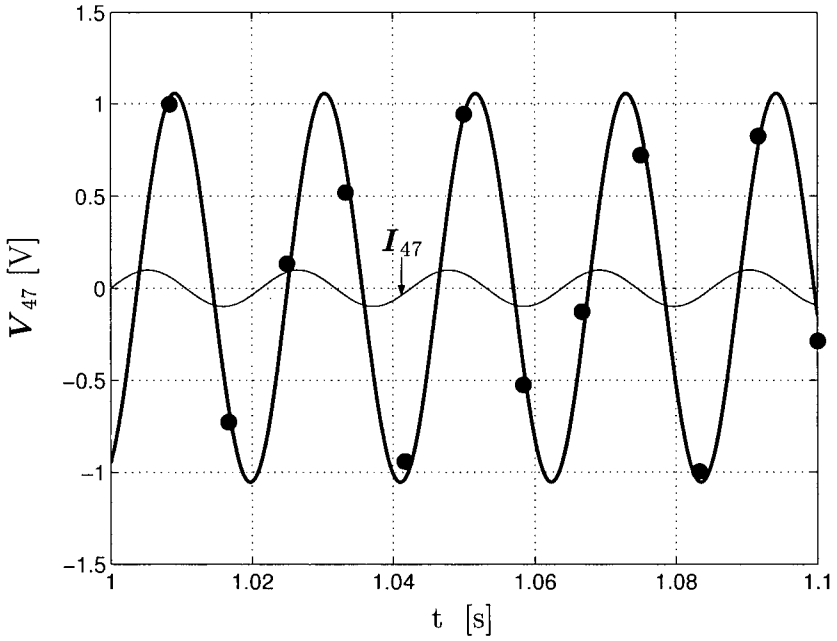

Figure 4.8: Comparison of $\boldsymbol{V}_{47}$ with the sample points from Poincaré map

4.6 Conclusion

Various studies have shown that the TCSC has a resistive behaviour towards subsynchronous currents. This phenomenon is, for the most part, independent of the actual resistance in the TCSC elements. When TCSC shows a positive resistance at a subsynchronous frequency, the energy is absorbed at that frequency and injected into the synchronous frequency. Therefore, the resistance at the subsynchronous frequency is obtained by a regenerative behaviour at the switching frequency that shows itself as a negative resistance, so that the ideal device does not dissipate energy, as expected.

The frequency response of TCSC is completely dependent on the firing scheme used for triggering the thyristors. While this result applies without argument for closed loop controls, the analysis contained here emphasizes the validity of the same statement about the open

loop controls as well.

The dynamic model of TCSC, obtained by the linearization of the Poincaré map, captures the passive damping, while the average steady-state model does not.

Chapter 5

Linear Model Derivation for a TCSC Compensated System

In the last chapter the linearization of a single-phase TCSC was discussed. It was shown that the linear model based on the Poincaré map captures the damping behaviour of the TCSC at subsynchronous frequencies. Throughout that analysis, the line current was assumed to be the forcing function. With this assumption, modular modelling of TCSC becomes possible. The linear models developed for a three-phase TCSC in [27, 32] are based on this supposition. However, the interface of the linear model thus obtained with the rest of the system has to be justified. This is especially true if the model is going to be used to design a feedback loop which aims at affecting the line currents by small signal variation of the TCSC firing angles.

To avoid this problem, a more general way is taken here to linearize the system dynamical equations. The Poincaré map or advance map of the nonlinear state space description of the whole system is linearized. Therefore, the line currents are among the state variables. The model is an outgrowth of the one introduced in [35]. The analysis in [35] assumes that the firing instants are constant, and therefore is short of giving the dependence of the advance map on the variations of the firing angles. This assumption is reasonable because the goal of that study is to obtain the eigenvalues of the linearized system to be able to assess the small signal stability at an operating point, with the TCSC in open loop operation.

Our treatment includes the variation of the firing angles. The model that is obtained is a sampled-data state-space model that allows the design of a feedback loop in order to vary the firing angles near a steady-state angle to increase the damping of subsynchronous modes of oscillation.

In the rest of the chapter, first the derivation of the model is explained in the general case. Then the model is derived for the equations of the First Subsynchronous Resonance Benchmark Model including a three-phase TCSC. In the next chapter, this model is then used to design the gains of a feedback controller that is able to eliminate subsynchronous instabilities.

5.1 Model Derivation

In order to simplify the discussion, the conduction angle σ is assumed to be less than 60°, so that at every instant either all thyristors are off or only one of them is conducting. This situation, depicted in Fig. 5.1, is typical when TCSC is operating in the capacitive mode, which is the mode of interest here. The discussion, however, is general and applies to other situations as well.

Between any two instants in time that none of the thyristors change their state, the power system with its nonlinearities, such as the generator torque equation, the trigonometric nonlinearities and the magnetic core saturation[1], is described by

$$\mathbf{x}(\mathbf{x}_{t_0}, t_0, t) = \mathbf{x}_{t_0} + \int_{t_0}^{t} \mathbf{g}(\mathbf{x}, \eta) d\eta \tag{5.1}$$

where $\mathbf{x}$, $\mathbf{x}_{t_0}$, and t_0 are the system state at time t, the initial state and the initial time, respectively. $\mathbf{g}(\mathbf{x}, t)$, the rate of change of state with time, is a set of nonlinear, time-varying equations. The dependence of $\mathbf{x}$ on the external sources, that is the turbine torques and the infinite voltage buses, is implicit in $\mathbf{g}$, though not shown to simplify notation. Since the model is derived for a single operating point, these external sources appear as constant parameters in the differential equations. Equation (5.1) is the integral form of $\dot{\mathbf{x}} = \mathbf{g}(\mathbf{x}, t)$

[1]The data provided for the IEEE First SSR Benchmark Model does not include the saturation curve, therefore in our study on this system, it is not taken into account.

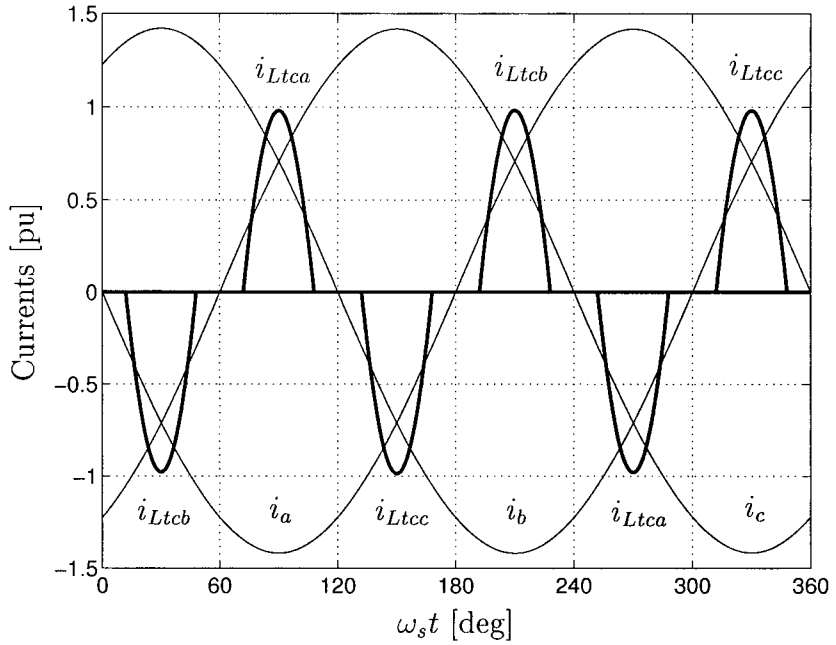

Figure 5.1: Steady-state waveforms of a three-phase TCSC in capacitive operation

with initial conditions $\mathbf{x} = \mathbf{x}_{t_0}$ at $t = t_0$. It is deliberately written in this form to show the functionality of the final state with respect not only to the time t, but also to the initial time t_0 and initial state $\mathbf{x}_{t_0}$. This information is necessary in the derivation of the linear model.

Suppose $\mathbf{x} \in \mathbb{R}^{n_x}$, where $\mathbf{x}$ is the state vector when all thyristors are off. If a thyristor turns on at time ϕ, a state variable will be added to the state vector and an equation to the set of differential equations. We will indicate this by an appropriate subscript, for example $\mathbf{x}_a$, $\mathbf{g}_a$. Since the current in the thyristor branch cannot change instantaneously, the following relation holds at the turn-on instant

$$\mathbf{x}_a(\phi) = \mathbf{Q_j}\mathbf{x}(\phi) \tag{5.2}$$

where $\mathbf{Q_j}$ is an $(n_x+1) \times n_x$ matrix that consists of an identity matrix of order n_x augmented with a row of zeros. Similarly at a switch-off time τ we have

$$\mathbf{x}(\tau) = \mathbf{P_j}\mathbf{x}_a(\tau) \tag{5.3}$$

with $\mathbf{P_j} = \mathbf{Q_j}^t$. $\mathbf{P_j}$ and $\mathbf{Q_j}$ are termed the *projection* and *injection* matrices, respectively

[51]. Also note that when a switch turns off, the rate of change of current in its branch becomes zero. Therefore at a switch-off time

$$\mathbf{g}(\mathbf{x}(\tau), \tau) = \mathbf{P_j g}_a(\mathbf{x}_a(\tau), \tau) \tag{5.4}$$

However, at a switch-on time the similar relation does not hold, that is

$$\mathbf{g}_a(\mathbf{x}_a(\phi), \phi) \neq \mathbf{Q_j g}(\mathbf{x}(\phi), \phi) \tag{5.5}$$

This is because when a thyristor turns on, the rate of change of current in its branch suddenly jumps to the nonzero value $v_{Ctc}(\phi)/L_{tc}$, where v_{Ctc} is the TCSC capacitor voltage, and L_{tc} the reactance in the thyristor branch.

Equations (5.2)-(5.5) are the boundary conditions between adjacent regions. With the help of these relations, the state variation at the end of one region is mapped into the state variation at the beginning of the next region.

The model developed in this section is a sampled-data model with a fixed sampling rate of 360 Hz. Fig. 5.2 shows two sampling instants, t_0 and t_1, taken with the sampling rate of 360 Hz. When the circuit is in steady state, six equidistant line current zero-crossings happen in one period. Therefore, if the first sample is taken at a line-current zero-crossing, the next sample will also coincide with the zero-crossing in another phase. In a real situation, the time span between two line current zero-crossings is variable. So t_1 may not exactly coincide with a zero-crossing.

In the next chapter, a controller based on the model developed here is designed for the TCSC firing. There, the sample points are the zero-crossing instants of the line currents. This is an approximation. However, since the variation of the time interval between the zero-crossings is small, the controller works properly.

Three time spans are identified between t_0 and t_1. During $[t_0 \quad \phi]$ and $[\tau \quad t_1]$ all the thyristors are off, while during $[\phi \quad \tau]$ the thyristor in phase b is conducting. Note that turn-on time ϕ, and the turn-off time τ are variable.

Starting with the third time span, the small signal variation of the state at t_1 as a result

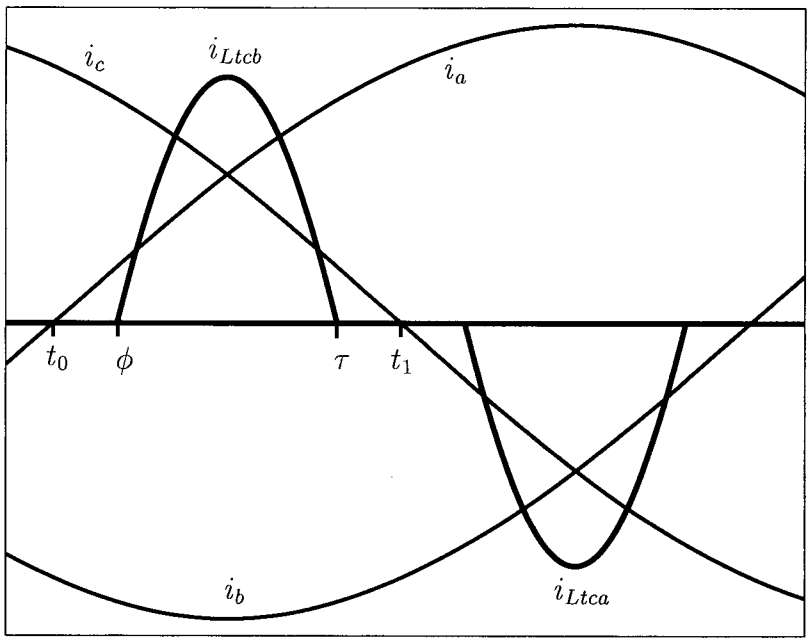

Figure 5.2: Current pulses in two phases and the line currents

of the variation of the state at τ and the change of τ itself, is

$$\Delta\mathbf{x}(t_1) = \left.\frac{\partial \mathbf{x}_{t_1}}{\partial \mathbf{x}_\tau}\right|_* \Delta\mathbf{x}(\tau) + \left.\frac{\partial \mathbf{x}_{t_1}}{\partial \tau}\right|_* \Delta\tau \tag{5.6}$$

where $\Delta\mathbf{x}$ denotes the small signal variations of the state variables about the periodic orbit. The orbit is identified by '$*$', such that $\mathbf{x}(t) = \mathbf{x}^*(t) + \Delta\mathbf{x}(t)$. The symbol '$|_*$' means evaluation at the steady state or periodic orbit. $\mathbf{x}_{t_1}$ and $\mathbf{x}_\tau$ in the partial derivatives mean $\mathbf{x}(t_1)$ and $\mathbf{x}(\tau)$, respectively. Since t_1 is a fixed sampling point, its derivative does not appear in (5.6).

At τ the thyristor in phase b turns off. Hence, (5.3) holds, and we have $\Delta\mathbf{x}(\tau) = \mathbf{P_j}\Delta\mathbf{x}_b(\tau)$, where $\Delta\mathbf{x}_b(\tau)$ is the small signal state variation at the final time of the second time span. $\Delta\mathbf{x}_b(\tau)$ is dependent on $\Delta\mathbf{x}_b(\phi)$, $\Delta\phi$, $\Delta\tau$ as follows

$$\Delta\mathbf{x}_b(\tau) = \left.\frac{\partial \mathbf{x}_{b\tau}}{\partial \mathbf{x}_{b\phi}}\right|_* \Delta\mathbf{x}_b(\phi) + \left.\frac{\partial \mathbf{x}_{b\tau}}{\partial \phi}\right|_* \Delta\phi + \left.\frac{\partial \mathbf{x}_{b\tau}}{\partial \tau}\right|_* \Delta\tau \tag{5.7}$$

Due to the boundary condition (5.2) at ϕ, we have $\Delta\mathbf{x}_b(\phi) = \mathbf{Q_j}\Delta\mathbf{x}(\phi)$. Finally, in the first time span $\Delta\mathbf{x}(\phi)$ is obtained as

$$\Delta\mathbf{x}(\phi) = \left.\frac{\partial \mathbf{x}_\phi}{\partial \mathbf{x}_{t_0}}\right|_* \Delta\mathbf{x}(t_0) + \left.\frac{\partial \mathbf{x}_\phi}{\partial \phi}\right|_* \Delta\phi \tag{5.8}$$

Note that since t_0 is fixed, its derivative is absent from (5.8). When (5.6)-(5.8) are combined with the aid of the boundary conditions, the linear map that advances the state variation from t_0 to t_1 is obtained as

$$\begin{aligned}\Delta\mathbf{x}(t_1) = &\frac{\partial \mathbf{x}_{t_1}}{\partial \mathbf{x}_\tau}\,\mathbf{P_j}\,\frac{\partial \mathbf{x}_{b\tau}}{\partial \mathbf{x}_{b\phi}}\,\mathbf{Q_j}\,\frac{\partial \mathbf{x}_\phi}{\partial \mathbf{x}_{t_0}}\,\Delta\mathbf{x}(t_0) + \\ &\frac{\partial \mathbf{x}_{t_1}}{\partial \mathbf{x}_\tau}\,\mathbf{P_j}\left[\frac{\partial \mathbf{x}_{b\tau}}{\partial \mathbf{x}_{b\phi}}\,\mathbf{Q_j}\,\frac{\partial \mathbf{x}_\phi}{\partial \phi} + \frac{\partial \mathbf{x}_{b\tau}}{\partial \phi}\right]\Delta\phi + \\ &\left[\frac{\partial \mathbf{x}_{t_1}}{\partial \mathbf{x}_\tau}\,\mathbf{P_j}\,\frac{\partial \mathbf{x}_{b\tau}}{\partial \tau} + \frac{\partial \mathbf{x}_{t_1}}{\partial \tau}\right]\Delta\tau \end{aligned} \tag{5.9}$$

where the symbol '$|_*$' has been omitted to simplify the notation, with the understanding that the partial derivatives are calculated on the steady-state orbit. If these derivatives can be obtained in an efficient way, then the model is practical.

First we notice that $\partial \mathbf{x}_{t_1}/\partial \mathbf{x}_\tau$, $\partial \mathbf{x}_{b\tau}/\partial \mathbf{x}_{b\phi}$ and $\partial \mathbf{x}_\phi/\partial \mathbf{x}_{t_0}$ are state transition matrices. A *state transition matrix*, $\mathbf{\Phi}(t, t_0)$, of the homogenous linearized system around the steady-state operating point

$$\frac{d\Delta\mathbf{x}}{dt} = \left.\frac{\partial \mathbf{g}}{\partial \mathbf{x}}\right|_* \Delta\mathbf{x} \triangleq \mathbf{J}(t)\Delta\mathbf{x}(t) \tag{5.10}$$

is the matrix that maps the small signal state at t_0 to the small signal state at t. $\mathbf{J}$ is the Jacobian matrix. If $\mathbf{J}$ satisfies the following commutativity property

$$\mathbf{J}(t)\left(\int_{t_0}^{t}\mathbf{J}(\eta)d\eta\right) = \left(\int_{t_0}^{t}\mathbf{J}(\eta)d\eta\right)\mathbf{J}(t) \tag{5.11}$$

then the state transition matrix has the closed form [20]

$$\mathbf{\Phi}(t, t_0) = \exp\left[\int_{t_0}^{t}\mathbf{J}(\eta)d\eta\right] \tag{5.12}$$

where exp is the matrix exponential function. However, (5.11) is not satisfied for our system, so $\mathbf{\Phi}(t, t_0)$ has to be calculated numerically in each region. The numerical calculation of the state transition matrix is the subject of Section 5.2.

Next, $\partial \mathbf{x}_\phi/\partial\phi$ and $\partial \mathbf{x}_{b\tau}/\partial\tau$ in (5.9) are of the form $\partial\mathbf{x}/\partial t$ which is equal to $\mathbf{g}(\mathbf{x}, t)$. So they are readily available.

It remains to be seen how $\partial \mathbf{x}_{t_1}/\partial\tau$ and $\partial \mathbf{x}_{b\tau}/\partial\phi$ are calculated in the general case of a non-linear time-varying system. If the equation (5.1) is differentiated with respect to $\mathbf{x}_{t_0}$ and t_0 we get

$$\frac{\partial \mathbf{x}}{\partial \mathbf{x}_{t_0}} = \mathbb{1} + \int_{t_0}^{t} \frac{\partial \mathbf{g}}{\partial \mathbf{x}} \frac{\partial \mathbf{x}}{\partial \mathbf{x}_{t_0}} d\eta \tag{5.13}$$

$$\frac{\partial \mathbf{x}}{\partial t_0} = -\mathbf{g}(\mathbf{x}_{t_0}, t_0) + \int_{t_0}^{t} \frac{\partial \mathbf{g}}{\partial \mathbf{x}} \frac{\partial \mathbf{x}}{\partial t_0} d\eta \tag{5.14}$$

These are recursive relations because $\partial \mathbf{x}/\partial \mathbf{x}_{t_0}$ and $\partial \mathbf{x}/\partial t_0$ appear on both sides. Using (5.13) and (5.14), it is possible to show by successive substitution that

$$\frac{\partial \mathbf{x}}{\partial t_0} = -\frac{\partial \mathbf{x}}{\partial \mathbf{x}_{t_0}} \mathbf{g}(\mathbf{x}_{t_0}, t_0) = -\mathbf{\Phi}(t, t_0)\mathbf{g}(\mathbf{x}_{t_0}, t_0) \tag{5.15}$$

The procedure of deriving (5.15) from (5.13) and (5.14) is shown in Appendix C. According to (5.15), *the partial derivative of the state at final time with respect to the initial time is obtained by multiplying the negative of the state transition matrix and the derivative function evaluated at the initial time.* The significance of (5.15) is that it is obtained for a linearized *time-varying* system. The derivation for linear time-invariant systems is straightforward because the solution for $\mathbf{x}$ in terms of t_0, $\mathbf{x}_{t_0}$ and t is expressed in a closed form using exponential functions.

Equation (5.15) together with (5.4) allows us to simplify the advance map given in (5.9). Using $\mathbf{\Phi}$ and $\mathbf{g}$ in the notation, the model for the linear system that advances the state from time t_0 to time t_1 becomes

$$\Delta \mathbf{x}(t_1) = \mathbf{A}\Delta \mathbf{x}(t_0) + \mathbf{b}\Delta\phi \tag{5.16}$$

with

$$\mathbf{A} = \mathbf{\Phi}^*(t_1, \bar{\tau})\mathbf{P_j}\mathbf{\Phi}_b^*(\bar{\tau}, \bar{\phi})\mathbf{Q_j}\mathbf{\Phi}^*(\bar{\phi}, t_0) \tag{5.17a}$$

$$\mathbf{b} = \mathbf{\Phi}^*(t_1, \bar{\tau})\mathbf{P_j}\mathbf{\Phi}_b^*(\bar{\tau}, \bar{\phi})\left[\mathbf{Q_j}\mathbf{g}(\mathbf{x}^*(\bar{\phi}), \bar{\phi}) - \mathbf{g}_b(\mathbf{x}_b^*(\bar{\phi}), \bar{\phi})\right] \tag{5.17b}$$

where the asterisk denotes a steady-state time function, and overbar on a variable denotes its steady-state value. It is noteworthy that the linear model does not depend on $\Delta\tau$, the

variation in the turn-off time. In fact, the coefficient of $\Delta\tau$ is

$$\begin{aligned}\mathbf{b}_\tau &= \mathbf{\Phi}^*(t,\bar{\tau})\mathbf{P_j g}_b(\mathbf{x}_b^*(\bar{\tau}),\bar{\tau}) - \mathbf{\Phi}^*(t,\bar{\tau})\mathbf{g}(\mathbf{x}^*(\bar{\tau}),\bar{\tau}) \\ &= \mathbf{\Phi}^*(t,\bar{\tau})[\mathbf{P_j g}_b(\mathbf{x}_b^*(\bar{\tau}),\bar{\tau}) - \mathbf{g}(\mathbf{x}^*(\bar{\tau}),\bar{\tau})] \\ &= \mathbf{0} \end{aligned} \tag{5.18}$$

The last line follows from (5.4). References [27, 45] have shown that the coefficients of the turn-off time are zero by using linear time-invariant representation for the system between two switching instants. The result here is obtained for the case of linear time-varying systems. Therefore, this is a general characteristic, that is *the linearized models of switching systems with unforced commutation do not depend on switch-off time variations.*

By incremental energy arguments, [51] identifies a source of damping associated with diodes or thyristors turning off. Since the method of Jacobian calculation used here is practically the same as there, this damping is included in the Jacobian (or equivalently, in the **A**-matrix of the model).

The linear model just obtained is valid for the positive pulse in phase b. Generally, if the discretization time step is chosen smaller than the period of the switching pattern, the linear system indices will be different for positive and negative pulses and for the three phases. For a TCSC compensated system, the models for the three phases are the same, but the positive and negative pulses have different zero-sequence components. Before proceeding to the controller design in the next chapter, the system state space description is reduced by eliminating the zero-sequence components. However, if they are to be kept, the linearized systems for the positive and negative pulses have to be distinguished from each other, for example by

$$\Delta\mathbf{x}(n+1) = \mathbf{A}_p\Delta\mathbf{x}(n) + \mathbf{b}_p\Delta\phi(n) \tag{5.19}$$

$$\Delta\mathbf{x}(n+1) = \mathbf{A}_n\Delta\mathbf{x}(n) + \mathbf{b}_n\Delta\phi(n) \tag{5.20}$$

5.2 Numerical Calculation of the State Transition Matrix

As indicated in the last section, for obtaining the linear system model we need to numerically calculate three state transition matrices. Recall that a state transition matrix is the matrix that advances the state in a certain time interval with the input being identically zero. For the first interval, this is shown as

$$\Delta\mathbf{x}(\bar{\phi}) = \mathbf{\Phi}^*(\bar{\phi}, t_0)\Delta\mathbf{x}(t_0) \tag{5.21}$$

Since the system is linearized, the effect of each input can be taken one at a time, with the other inputs set to zero. To get the first column of $\mathbf{\Phi}^*(\bar{\phi}, t_0)$ we apply $\Delta\mathbf{x}(t_0) = [1\ 0\ \ldots\ 0]^t$ and numerically integrate (5.10) from t_0 to $\bar{\phi}$. The other columns are calculated in a similar way. The following example shows how MATLAB® is used to find the state transition matrix.

Example

Suppose a nonlinear set of differential equations is given as

$$\dot{\mathbf{x}} = \begin{bmatrix}\dot{x}_1\\ \dot{x}_2\end{bmatrix} = \begin{bmatrix}-\sqrt{x_1} + x_2^2\\ x_1\end{bmatrix} \triangleq \mathbf{f}(\mathbf{x}) \tag{5.22}$$

and we want to calculate the state transition matrix $\Phi(1,0)$ of the linearized system around the path

$$x_1^*(t) = t + 1 \tag{5.23a}$$

$$x_2^*(t) = \cos t \tag{5.23b}$$

The Jacobian of the nonlinear system is

$$\mathbf{J}(\mathbf{x}) = \begin{bmatrix}\frac{\partial f_1}{\partial x_1} & \frac{\partial f_1}{\partial x_2}\\ \frac{\partial f_2}{\partial x_1} & \frac{\partial f_2}{\partial x_2}\end{bmatrix} = \begin{bmatrix}\frac{-1}{2\sqrt{x_1}} & 2x_2\\ 1 & 0\end{bmatrix} \tag{5.24}$$

$\mathbf{J}$ is the $\mathbf{A}$-matrix of the linearized continuous system

$$\frac{d\Delta\mathbf{x}}{dt} = \mathbf{J}(\mathbf{x})\Delta\mathbf{x} \tag{5.25}$$

whose state transition matrix is to be calculated. MATLAB® ODE solvers numerically integrate a set of differential equations. The derivative function is passed to the ODE solver in a separate file. For the current example the following file is used

```
function Dxdot = deriv(t,Dx)
xstar = [t+1; cos(t)];
x1 = xstar(1);
x2 = xstar(2);
A = [-1/2/sqrt(x1)        2*x2; ...
              1             0    ];

Dxdot = A*Dx;
```

The linearized equations given in (5.25) are to be integrated from time 0 to time 1, once with the initial condition Dx0 = [1; 0] to get the first column of $\Phi(1,0)$, and once with the initial condition Dx0 = [0; 1] to obtain the second column of $\Phi(1,0)$. The following code does the task.

```
Phi = zeros(2, 2);
Dx01 = [1; 0];
Dx02 = [0; 1];
Dx0vector = {Dx01; Dx02};
tspan = [0.0    1.0];
options = odeset('RelTol', 1e-3, 'AbsTol', 1e-6, 'MaxStep', 1e-3);
for i = 1 : 2
    Dx0 = Dx0vector{i};
    [t,Dx] = ode45('deriv', tspan, Dx0, options);
    Phi(:,i) = Dx(length(t),:)';
end
```

The numerical integration solution is returned in the vectors t and Dx. The last row of Dx corresponds to the final time of the integration. The above program yields the following

state transition matrix

$$\mathbf{\Phi}(1,0) = \begin{bmatrix} 1.3235 & 1.7706 \\ 1.0607 & 1.9183 \end{bmatrix} \tag{5.26}$$

As seen in the example, the state transition matrix is calculated about the periodic orbit of the system. Finding $\mathbf{x}^*$ is not a trivial task. One has to find the algebraic unknown $\mathbf{x}(0)$ such that $\mathbf{x}(0+T) = \mathbf{x}(0)$. However, since the current harmonics of the TCSC are mainly confined to its LC loop, and do not enter the line, the load flow solution is a good approximation for the periodic orbit.

For this purpose, the TCSC is replaced by its equivalent reactance at the fundamental frequency. After the load flow, time vectors with the desired time step are built for each of the ideal steady-state waveforms to be able to update $\partial\mathbf{g}/\partial\mathbf{x}$, as the integration proceeds. For this step, the non-sinusoidal ideal waveforms of the TCSC variables are used. Once the state transition matrices are ready, (5.17a) and (5.17b) are employed to calculate the $\mathbf{A}$ and $\mathbf{b}$ matrices.

The algorithm to obtain the discrete linear model parameters is therefore as follows:

1. Find the Jacobian of the nonlinear dynamical equations.
2. Perform a load flow for the system in the given operating point.
3. Build the ideal steady-state time vectors for each of the states. This is the approximate periodic orbit of the Poincaré map.
4. Calculate the state transition matrix for each of the time spans by introducing a disturbance in each state one at a time and integrating the linearized equations, (5.10), along the approximate orbit.
5. Use (5.17a) and (5.17b) to calculate $\mathbf{A}$ and $\mathbf{b}$.

In the next section, the steps are worked out for a particular example.

5.3 Linearization of the IEEE First SSR Benchmark Model with TCSC

The model discussed in the previous sections is tested here on the IEEE First Subsynchronous Resonance Benchmark Model. It is modified to include a series compensation that is partly

fixed and partly thyristor controlled, as shown in Fig. 2.4. The system parameters are given in Appendix B.1, and state equations appear in Appendix B.2. The state of the unfaulted system with all the thyristors off is defined as

$$\begin{aligned}\mathbf{x} = [&i_0, i_d, i_q, i_F, i_D, i_Q, i_G, v_{C0}, v_{Cd}, v_{Cq}, v_{Ctc0}, v_{Ctcd}, v_{Ctcq},\\ &\omega_1, \omega_2, \omega_3, \omega_4, \omega, \omega_5, \theta_1, \theta_2, \theta_3, \theta_4, \theta, \theta_5]^t\end{aligned} \tag{5.27}$$

where i_0, i_d and i_q are the line currents, i_F, i_D, i_Q, and i_G are the rotor currents, v_{C0}, v_{Cd}, and v_{Cq} are the fixed capacitor voltages, v_{Ctc0}, v_{Ctcd}, and v_{Ctcq} are the thyristor-controlled capacitor voltages and ω_i's and θ_i's are the rotor speeds and angles, respectively.

In the transient simulation, more state variables will be added to the state vector in (5.27) when topological changes happen, for example when thyristors turn on or when a fault occurs. The nonlinear equations are listed in matrix form in (5.28) for the case with all thyristors off.

$$\begin{bmatrix} \begin{bmatrix} \dot{\mathbf{i}}_{0dq} \\ \dot{\mathbf{i}}_{FDQG} \end{bmatrix} \\ \dot{\mathbf{v}}_{C,0dq} \\ \dot{\mathbf{v}}_{Ctc,0dq} \\ \dot{\boldsymbol{\omega}} \\ \dot{\boldsymbol{\theta}} \end{bmatrix} = \begin{bmatrix} \hat{\mathbf{L}}^{-1}(\omega\hat{\mathbf{N}}-\hat{\mathbf{R}}) & -\hat{\mathbf{L}}^{-1}\begin{bmatrix}\mathbb{1}_3 \\ \mathbf{0}_{4\times3}\end{bmatrix} & -\hat{\mathbf{L}}^{-1}\begin{bmatrix}\mathbb{1}_3 \\ \mathbf{0}_{4\times3}\end{bmatrix} & \mathbf{0}_{7\times6} & \mathbf{0}_{7\times6} \\ C^{-1}[\mathbb{1}_3\ \mathbf{0}_{3\times4}] & \omega\mathbf{M} & \mathbf{0}_{3\times3} & \mathbf{0}_{3\times6} & \mathbf{0}_{3\times6} \\ C_{tc}^{-1}[\mathbb{1}_3\ \mathbf{0}_{3\times4}] & \mathbf{0}_{3\times3} & \omega\mathbf{M} & \mathbf{0}_{3\times6} & \mathbf{0}_{3\times3} \\ \mathbf{0}_{6\times7} & \mathbf{0}_{6\times3} & \mathbf{0}_{6\times3} & -\frac{1}{2\omega_B}\mathbf{H}^{-1}\mathbf{D} & -\frac{1}{2\omega_B}\mathbf{H}^{-1}\mathbf{K} \\ \mathbf{0}_{6\times7} & \mathbf{0}_{6\times3} & \mathbf{0}_{6\times3} & \mathbb{1}_6 & \mathbf{0}_{6\times6} \end{bmatrix} \begin{bmatrix} \begin{bmatrix} \mathbf{i}_{0dq} \\ \mathbf{i}_{FDQG} \end{bmatrix} \\ \mathbf{v}_{C,0dq} \\ \mathbf{v}_{Ctc,0dq} \\ \boldsymbol{\omega} \\ \boldsymbol{\theta} \end{bmatrix} + \\ \begin{bmatrix} -\hat{\mathbf{L}}^{-1} & \mathbf{0}_{7\times6} & \mathbf{0}_{7\times6} & \mathbf{0}_{7\times6} \\ \mathbf{0}_{6\times7} & \mathbf{0}_{6\times6} & \mathbf{0}_{6\times6} & \mathbf{0}_{6\times6} \\ \mathbf{0}_{6\times7} & \mathbf{0}_{6\times6} & \frac{1}{2\omega_B}\mathbf{H}^{-1} & \mathbf{0}_{6\times6} \\ \mathbf{0}_{6\times7} & \mathbf{0}_{6\times6} & \mathbf{0}_{6\times6} & \mathbf{0}_{6\times6} \end{bmatrix} \begin{bmatrix} \mathbf{0}_{1\times3} & \mathbf{0}_{1\times6} \\ \mathbb{1}_3 & \mathbf{0}_{3\times6} \\ \mathbf{0}_{9\times3} & \mathbf{0}_{9\times6} \\ \mathbf{0}_{6\times3} & \mathbb{1}_6 \\ \mathbf{0}_{6\times3} & \mathbf{0}_{6\times6} \end{bmatrix} \begin{bmatrix} -\sqrt{3}V_\infty \sin(\theta - t - \frac{\pi}{2} - \alpha_\infty) \\ \sqrt{3}V_\infty \cos(\theta - t - \frac{\pi}{2} - \alpha_\infty) \\ -V_F \\ t_{q1} \\ t_{q2} \\ t_{q3} \\ t_{q4} \\ -t_{qe} \\ t_{q5} \end{bmatrix} \end{bmatrix} \tag{5.28}$$

Note that (5.28) can be written in the compact form

$$\dot{\mathbf{x}} = \mathbf{A}(\omega)\mathbf{x} + \mathbf{B}\mathbf{u}(\mathbf{i}_{0dq}, \mathbf{i}_{FDQG}, \theta, t) \tag{5.29}$$

In (5.29), the mechanical torques t_{q1}, t_{q2}, t_{q3}, t_{q4}, t_{q5}, the voltage parameters of the infinite

bus V_∞ and α_∞, and the field voltage V_F are constant, because the model is obtained at one steady-state operating point.

The electromagnetic torque is a function of the currents in the generator stator and rotor, therefore $\mathbf{u}$ is dependent on these currents. Note that $\mathbf{B}$ is a constant matrix, obtained by multiplying the first two matrices in the second row of (5.28). The explicit dependence of (5.29) on t can be eliminated by using the machine load angle $\delta(t)$ which is given by $\delta = \theta - t - \pi/2$.

The dynamical equations describing the case where any of the thyristors is on are conveniently described using the notation in (5.29). For example, if the branch in phase a is conducting, i_{Ltca} is added to the state variables. The equations then look like the following:

$$\dot{\mathbf{x}}_a = \begin{bmatrix} \dot{\mathbf{x}} \\ \dot{i}_{Ltca} \end{bmatrix} = \left[\begin{array}{ccc|c} & \mathbf{A}(\omega)_{25\times 25} & & \begin{array}{c}\mathbf{0}_{10\times 1}\\ -C_{tc}^{-1}\mathbf{P}(\theta)\begin{bmatrix}1\\0\\0\end{bmatrix}\\ \mathbf{0}_{12\times 1}\end{array} \\ \hline \mathbf{0}_{1\times 10} & L_{tc}^{-1}[1\ 0\ 0]\mathbf{Q}(\theta) & \mathbf{0}_{1\times 12} & 0 \end{array}\right] \mathbf{x}_a + \begin{bmatrix} \mathbf{B} \\ \mathbf{0}_{1\times 9} \end{bmatrix} \mathbf{u}(\mathbf{i}_{0dq}, \mathbf{i}_{FDQG}, \delta)$$

$$\triangleq \mathbf{A}_a(\omega, \theta)\mathbf{x}_a + \mathbf{B}_a\mathbf{u}(\mathbf{i}_{0dq}, \mathbf{i}_{FDQG}, \delta) \tag{5.30}$$

where $\mathbf{P}(\theta)$ and $\mathbf{Q}(\theta)$ are Park's transformation matrices. The Jacobians of the system in each region are the $\mathbf{A}$-matrices of the linearized system. They are needed in order to calculate the state transition matrices. The Jacobian of (5.29) is

$$\mathbf{J} = \frac{\partial}{\partial \mathbf{x}}[\mathbf{A}(\omega)\mathbf{x} + \mathbf{B}\mathbf{u}] = \mathbf{A}(\omega) + \left[\mathbf{0}_{25\times 17} \quad \frac{\partial \mathbf{A}}{\partial \omega}\mathbf{x} \quad \mathbf{0}_{25\times 7}\right] + \mathbf{B}\frac{\partial \mathbf{u}}{\partial \mathbf{x}} \tag{5.31}$$

By using (5.28), we have

$$\frac{\partial \mathbf{A}}{\partial \omega}\mathbf{x} = \begin{bmatrix} \hat{\mathbf{L}}^{-1}\hat{\mathbf{N}}\begin{bmatrix}\mathbf{i}_{0dq}\\ \mathbf{i}_{FDQG}\end{bmatrix} \\ \mathbf{M}\mathbf{v}_{C,0dq} \\ \mathbf{M}\mathbf{v}_{Ctc,0dq} \\ \mathbf{0}_{12\times 1} \end{bmatrix} \tag{5.32}$$

and

$$\frac{\partial \mathbf{u}}{\partial \mathbf{x}} = \begin{bmatrix} \mathbf{0}_{7\times7} & \mathbf{0}_{7\times16} & -\hat{\mathbf{L}}^{-1}\begin{bmatrix}\mathbf{0}_{1\times3}\\ \mathbb{1}_3 \\ \mathbf{0}_{3\times3}\end{bmatrix}\begin{bmatrix}-\sqrt{3}V_\infty\cos(\delta-\alpha_\infty)\\ -\sqrt{3}V_\infty\sin(\delta-\alpha_\infty)\\ 0\end{bmatrix} & \mathbf{0}_{7\times1} \\ \mathbf{0}_{10\times7} & \mathbf{0}_{10\times16} & \mathbf{0}_{10\times1} & \mathbf{0}_{10\times1} \\ -\dfrac{1}{2\omega_B H}\dfrac{\partial t_{qe}}{\partial \mathbf{i}} & \mathbf{0}_{1\times16} & \mathbf{0}_{1\times7} & \mathbf{0}_{1\times1} \\ \mathbf{0}_{7\times7} & \mathbf{0}_{7\times16} & \mathbf{0}_{7\times1} & \mathbf{0}_{7\times1} \end{bmatrix} \tag{5.33}$$

where $\partial t_{qe}/\partial \mathbf{i}$ is

$$\frac{\partial t_{qe}}{\partial \mathbf{i}} \triangleq \begin{bmatrix} 0 & \dfrac{\partial t_{qe}}{\partial i_d} & \dfrac{\partial t_{qe}}{\partial i_q} & \dfrac{\partial t_{qe}}{\partial i_F} & \dfrac{\partial t_{qe}}{\partial i_D} & \dfrac{\partial t_{qe}}{\partial i_Q} & \dfrac{\partial t_{qe}}{\partial i_G} \end{bmatrix} \tag{5.34}$$

The relation for the electromagnetic torque in terms of the machine currents is given in (B.33). So each of the terms in (5.34) is available.

The Jacobian for the interval with a thyristor in phase a conducting is

$$\mathbf{J}_a = \mathbf{A}_a(\omega,\theta) + \begin{bmatrix} \mathbf{0}_{26\times17} & \dfrac{\partial \mathbf{A}_a}{\partial \omega}\mathbf{x}_a & \mathbf{0}_{26\times5} & \dfrac{\partial \mathbf{A}_a}{\partial \theta}\mathbf{x}_a & \mathbf{0}_{26\times2} \end{bmatrix} + \mathbf{B}_a\frac{\partial \mathbf{u}}{\partial \mathbf{x}_a} \tag{5.35}$$

with

$$\frac{\partial \mathbf{A}_a}{\partial \omega}\mathbf{x} = \begin{bmatrix} \hat{\mathbf{L}}^{-1}\hat{\mathbf{N}}\begin{bmatrix}\mathbf{i}_{0dq}\\ \mathbf{i}_{FDQG}\end{bmatrix} \\ \mathbf{M}\mathbf{v}_{C,0dq} \\ \mathbf{M}\mathbf{v}_{Ctc,0dq} \\ \mathbf{0}_{13\times1} \end{bmatrix} \qquad \frac{\partial \mathbf{A}_a}{\partial \theta}\mathbf{x} = \begin{bmatrix} \mathbf{0}_{10\times1} \\ -C_{tc}^{-1}\dfrac{d\mathbf{P}}{d\theta}\begin{bmatrix}1\\0\\0\end{bmatrix} i_{Ltca} \\ \mathbf{0}_{12\times1} \\ -L_{tc}^{-1}[1\ \ 0\ \ 0]\dfrac{d\mathbf{Q}}{d\theta}\begin{bmatrix}v_{Ctc0}\\ v_{Ctcd}\\ v_{Ctcq}\end{bmatrix} \end{bmatrix} \tag{5.36}$$

The matrix $\partial \mathbf{u}/\partial \mathbf{x}_a$ is similar to (5.33) with a row and a column of zeros added in the end.

With the Jacobians at hand, the next step is to find the periodic cycle of the circuit, so that the state transition matrices be computed on the orbit. For this purpose, a load flow solution is used to approximate the periodic orbit.

In the case studies of this section, the linear model is computed for two different sets of series compensation parameters, and the eigenvalues are examined to see if they portray the stability of the system.

Note that since the obtained model is discrete, the stability of an eigenvalue is determined by its position in the z-plane relative to the unit circle. However, since it is convenient to identify the subsynchronous modes by their frequencies, the eigenvalue results are presented both in discrete and continuous domains, where the continuous eigenvalues are obtained with the procedure explained next.

5.3.1 Conversion of Eigenvalues from Discrete to Continuous

In a TCSC compensated system, continuous and discrete dynamics are both present, and interact with each other. The discrete events are the firing instants of the thyristors which affect and are affected by the continuous states of the system.

The model we have derived is a sampled-data model with a fixed time step, during which one discrete event (firing instant) occurs. The **A**-matrix of this model corresponds to the matrix **F** in (2.23). The model is internally stable if all its eigenvalues are inside the unit circle.

Suppose the matrix $\mathbf{A}_{eq}$ in (2.23) has an eigenvalue $\lambda_c = a_c + jb_c$. Then, the matrix **F** has an eigenvalue $\lambda_d = e^{(a_c+jb_c)T}$. If λ_d is multiplied by its complex conjugate, $\breve{\lambda}_d$ [2], the resultant number is e^{2a_cT}. Therefore, the real part or the damping of the corresponding continuous-time eigenvalue is determined by

$$a_c = \frac{1}{2T}\ln(\lambda_d\breve{\lambda}_d) \tag{5.37}$$

The continuous-time frequency is not determined uniquely by the discrete-time eigenvalue. In fact, the entire frequency domain of $-\infty < f < \infty$ Hz is mapped into $-f_{Ny} < f < f_{Ny}$ Hz, where f_{Ny} is the Nyquist frequency $f_{Ny} = 1/(2T)$ Hz. Notice that

$$e^{(a_c+jb_c)T} = e^{a_cT}\cos b_cT + je^{a_cT}\sin b_cT \triangleq a_d + jb_d \tag{5.38}$$

By calculating $\arctan(b_d/a_d)$ and adjusting the arc such that $-\pi < b_cT < \pi$, then the value of b_c is obtained in $-\omega_{Ny} \le b_c \le \omega_{Ny}$.

[2]Since $\bar{x}$ is used to indicate the steady-state value of a variable x, to avoid confusion, the complex conjugate is denoted by $\breve{x}$.

With a small enough time step, the subsynchronous modes are represented without aliasing, however there is a possibility that a mode with a frequency higher than the Nyquist becomes aliased into the subsynchronous region. Since the frequencies of the mechanical modes of the isolated shaft assembly, given in Table 3.1, do not change considerably when the shaft is incorporated into the electromechanical system, it is relatively easy to distinguish the real subsynchronous modes in the set of eigenvalues obtained by the above conversion.

Note that the frequency response of the discretized system is generally different from the original system. For simplicity assume that the original system is completely continuous. There are several methods available to discretize this system in order to obtain discrete-time models. They are based either on numerical integration methods or, like here, on the state space method. The particular method used for discretization and the sampling frequency affect the dynamic characteristics of the resulting system [55]. For frequencies well below the Nyquist frequency, the response of the discrete system is a good approximation of the continuous system. The following example illustrates this point.

Example

Suppose a continuous linear time-invariant scalar system is given as

$$\dot{x} = Ax(t) + bu(t) \tag{5.39}$$

The transfer function of this system is

$$H_c(s) = \frac{b}{s - A} \tag{5.40}$$

To discretize (5.39), we solve the differential equation for $x(n\Delta t)$ given the initial condition $x(n\Delta t - \Delta t)$.

$$x(n\Delta t) = e^{A\Delta t}x(n\Delta t - \Delta t) + \int_{n\Delta t - \Delta t}^{n\Delta t} e^{A(n\Delta t - \eta)}bu(\eta)d\eta \tag{5.41}$$

Assuming the input to be $u(n\Delta t - \Delta t)$ in the time span $n\Delta t - \Delta t \leq t \leq n\Delta t$, the input comes out of the integral, and the following discrete system results

$$x(n) = Fx(n-1) + gu(n-1) \tag{5.42}$$

where

$$F = e^{A\Delta t} \tag{5.43a}$$

$$g = \frac{b}{A}(e^{A\Delta t} - 1) \tag{5.43b}$$

The discrete transfer function is found by taking the z-transform of (5.42)

$$H_d(z) = \frac{g}{z - F} \tag{5.44}$$

To compare the frequency response of (5.40) and (5.44), take $A = -0.1$, and $b = 0.1$, and $\Delta t = 1/360$ s. We plot the ratio of the continuous transfer function for $s = j\omega$, to the the discrete transfer function for $z = e^{j\omega\Delta t}$ in Fig. 5.3.

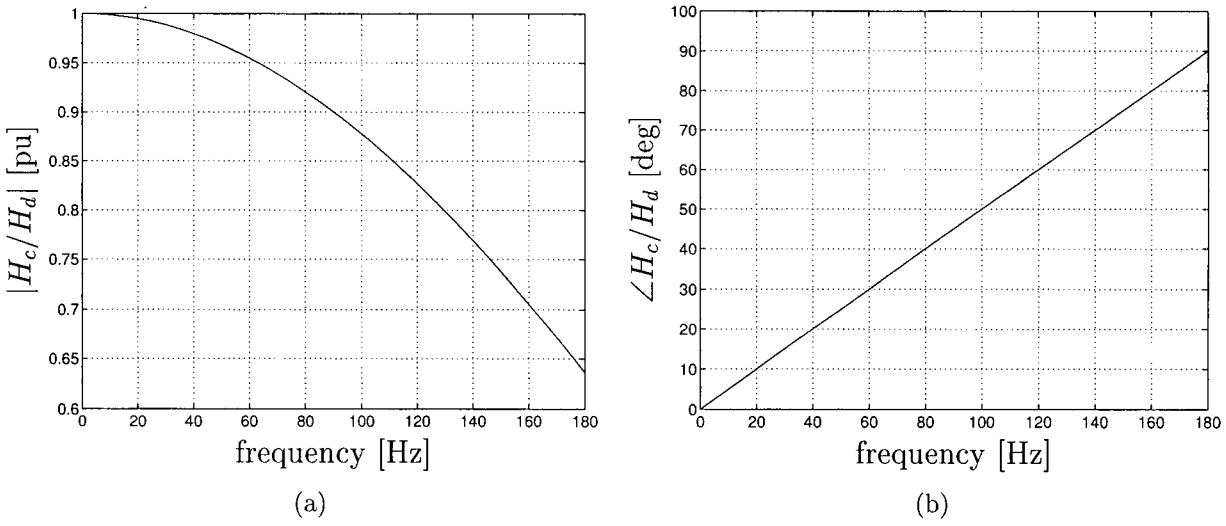

Figure 5.3: Comparison of the continuous and discrete transfer functions

Fig. 5.3(a) shows that at very small frequencies, the magnitude ratio is close to unity. As the frequency increases, the difference in the magnitude of the original continuous system and that of the discretized one increases. Since the time step is 1/360 s, the Nyquist frequency is 180 Hz. For this particular example, the magnitude of discrete transfer function for frequencies below 60 Hz, is less than 5% different from the corresponding continuous magnitude.

The phase of the discrete system increases linearly with frequency with respect to the continuous system phase as shown in Fig. 5.3(b).

5.3.2 Case Study 1

In this case the value of the fixed capacitor and the thyristor controlled capacitor are chosen as given in the appendix B.1. The total capacitive reactance is 0.371 pu when the thyristor valves are blocked. The dominant unstable mode under the blocked mode is TM2 with frequency 20.21 Hz. TCSC is set to work with 164° corresponding to a steady-state conduction angle of 32°.

Case1: Load Flow

With $X_{Ctc} = 0.25$ pu, $\kappa = 3$ and $\beta = (\pi/180)(180° - 164°)$ rad, the fundamental reactance of TCSC, calculated from (2.13), is equal to 0.2785 pu Therefore the *nominal degree of compensation* of the line [9] is

$$k_{nom} \triangleq \frac{X_C + X_{TCSC}}{X_{1line}} = \frac{0.121 + 0.2785}{0.50} = 79.9\ \% \tag{5.45}$$

The terminal characteristics are given as $P_t = 0.9$ pu, $V_t = 1.0$ pu and $PF = 0.9$. Using the terminal voltage as the reference phasor[3] we will have

$$\boldsymbol{V}_a = 1.0 \angle 0.0 \ \text{ pu} \tag{5.46}$$

$$\boldsymbol{I}_a = \frac{P_t}{V_t \cdot PF} \angle \cos^{-1} PF = 1.0 \angle -25.84° \ \text{ pu} \tag{5.47}$$

$$\boldsymbol{Z} = 0.02 + j(X_{1_{tot}} - X_C - X_{TCSC}) = 0.02 + j0.3005 \text{ pu} \tag{5.48}$$

$$\boldsymbol{V}_{\infty a} = \boldsymbol{V}_a - \boldsymbol{Z}\boldsymbol{I}_a = 0.8903 \angle -17.094° \text{ pu} \tag{5.49}$$

$\boldsymbol{V}_{\infty a}$ is the phasor of the infinite bus voltage (see Fig. B.1). $X_{1_{tot}} = 0.7$ pu is the total positive-sequence reactance of the line, the transformer, and the infinite bus. $\boldsymbol{Z}$ is the total series impedance, including the compensation. The machine torque angle δ, as indicated in Fig. 5.4, is obtained by finding the angle of the phasor $\boldsymbol{E}_{qa}$ which is along the same direction as the internal EMF $\boldsymbol{E}_q$ [60].

[3] If $\boldsymbol{V} = V\angle\theta$, then $v(t) = \sqrt{2}V\cos(\omega_s t + \theta)$.

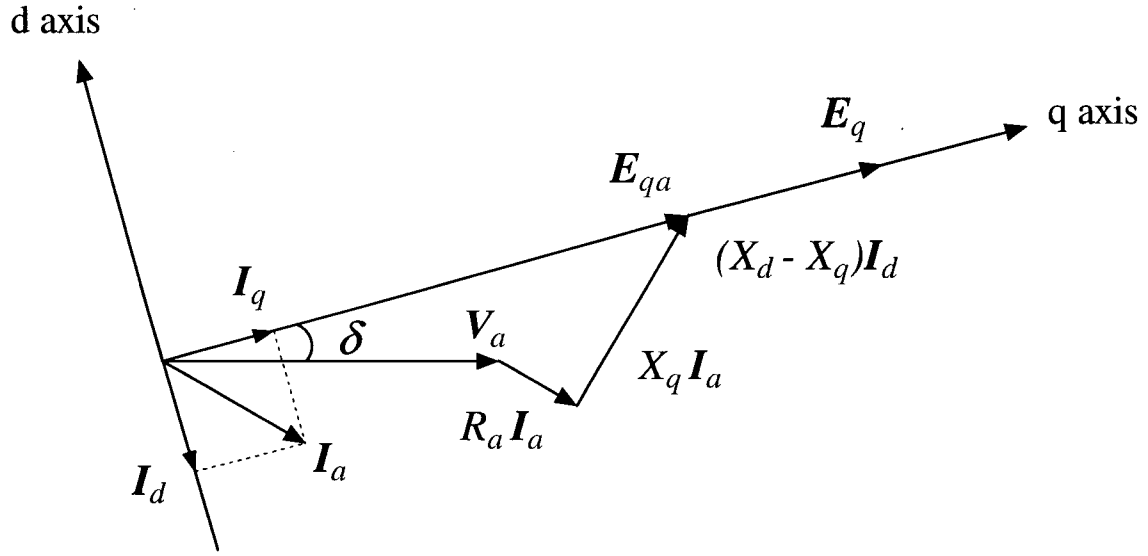

Figure 5.4: Location of the q axis from a known terminal current and voltage

$$\boldsymbol{E}_{qa} = \boldsymbol{V}_a + R_a \boldsymbol{I}_a + jX_q \boldsymbol{I}_a = 2.3270 \angle 41.4046° \text{ pu} \tag{5.50}$$

$$\boldsymbol{E}_q = \boldsymbol{E}_{qa} + j(X_d - X_q)\boldsymbol{I}_d = 2.40075 \angle 41.4046° \text{ pu} \tag{5.51}$$

X_d and X_q are the d-axis and q-axis synchronous reactances. Their values in pu are equal to L_d and L_q, respectively given in Table B.1. Having determined $\boldsymbol{E}_q$, we proceed to find the field current and voltage

$$I_F = \frac{\sqrt{3}E_q}{X_{AD}} = 2.505 \text{ pu} \tag{5.52}$$

$$V_F = R_F I_F = 0.00352 \text{ pu} \tag{5.53}$$

In the simulations, the time when the current in phase a crosses zero downwards has been chosen as the initial time. Therefore, the angles calculated above need to be adjusted accordingly. The initial mechanical angles are then easily calculated. The initial state variable values are listed in Table 5.1, where the electrical variables on the stator side are given in the dq rotor reference frame, using the Park transformation (3.35).

The load flow results are used to construct the limit cycle of the system. In this cycle, all the electrical variables except for the TCSC voltages are constant. The fact that most of the harmonics produced by the TCSC do not enter the line supports the assumption of sinusoidal

Table 5.1: Initial state variable values used for simulation

Elec.	[pu]	Mech.	[pu]
i_0	0.0	ω_1	1.0
i_d	−1.597258	ω_2	1.0
i_q	0.669900	ω_3	1.0
i_F	2.504958	ω_4	1.0
i_D	0.0	ω	1.0
i_Q	0.0	ω_5	1.0
i_G	0.0	θ_1	−1.871256
v_{C0}	0.0	θ_2	−1.882234
v_{Cd}	−0.081058	θ_3	−1.895517
v_{Cq}	−0.193268	θ_4	−1.935119
v_0	−0.018423	θ	−1.967920
v_{Ctcd}	−0.187629	θ_5	−1.973194
v_{Ctcq}	−0.447367		

line currents. For the TCSC voltages the relations presented in Section 2.4 are used to build the time response of v_{Ctca}, v_{Ctcb}, and v_{Ctcc}, and then by applying the Park transformation on them, the waveforms for v_{Ctc0}, v_{Ctcd}, and v_{Ctcq} are obtained. The mechanical speeds are all constant. The rotor positions change linearly with time, for example the waveform of θ_1 becomes $\theta_1(t) = t + \theta_1(0)$ rad.

Case1: Linear System Parameters

The $\mathbf{A}_n$ and $\mathbf{b}_n$ matrices for a time span including a negative pulse, and $\mathbf{A}_p$ and $\mathbf{b}_p$ matrices for a time span including a positive pulse, are obtained by following the procedure outlined above. Fig.5.5 shows the $\mathbf{b}$ vector elements for the first 13 variables in (5.27). The elements for the rest of the variables are very small and negligible.

The 11th element pertains to the zero sequence component of the TCSC voltage, v_{Ctc0}. This is the only significant zero-sequence component; the elements for i_0 and v_{C0} (1 and 8) are very small. Since the equations for i_0 and v_{C0} are independent from the rest of the equations, they can be omitted, without concern, to reduce the size of the state space to 23. The condition number [63] for the reduced-order system is decreased several orders of magnitude as compared to the full-order system. This is because the zero-sequence variables

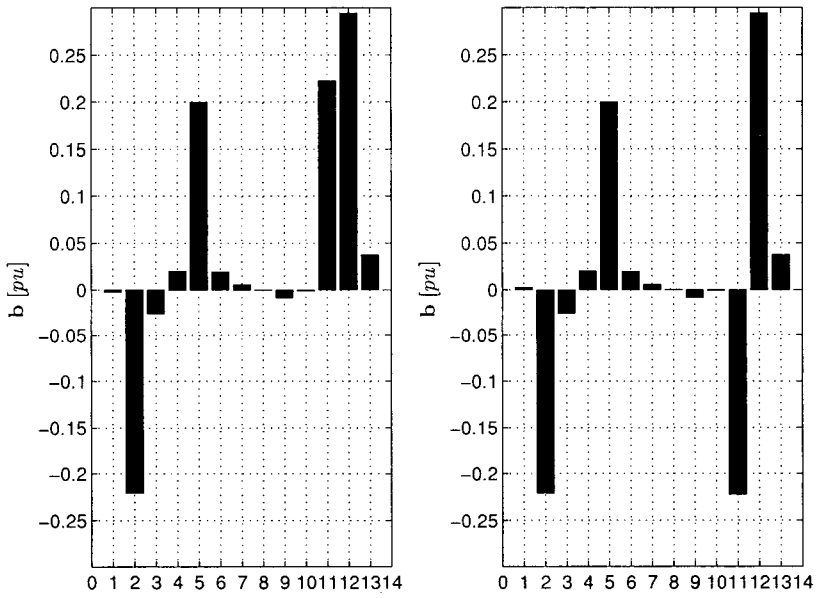

(a) Positive pulse (b) Negative pulse

Figure 5.5: The **b** vector coefficients for the positive and negative pulses

are weakly controllable. The impact of the zero-sequence voltage of the TCSC is studied more carefully before its omission, since it is not entirely decoupled from the rest of the variables. This is considered in the eigenvalue analysis in the next section.

Case1: Eigenvalue Analysis

According to Theorem 1 in Section 2.5, if we want to study the stability of the time-periodic system, we need to find either the matrix $\mathbf{A}_{eq}$ or the matrix $\mathbf{F}$. Since the TCSC compensated system returns to its original state after 1/60 s , the advance map that transfers a disturbance through this time is

$$\mathbf{F} = \mathbf{A}_n\mathbf{A}_p\mathbf{A}_n\mathbf{A}_p\mathbf{A}_n\mathbf{A}_p = (\mathbf{A}_n\mathbf{A}_p)^3 \tag{5.54}$$

Notice that the three-phase symmetry helps reduce the time step to one-third of the main period or 1/180 s. This is evident from (5.54) because multiplying a matrix by itself does not change its stability properties. If $\mathbf{A}_n\mathbf{A}_p$ has an eigenvalue inside the unit circle, $(\mathbf{A}_n\mathbf{A}_p)^3$ has a corresponding eigenvalue inside the unit circle and vice versa.

Furthermore, the only difference between the elements of $\mathbf{A}_n$ and $\mathbf{A}_p$ happens in the rows and columns pertaining to the zero sequence variables, i_0, v_{C0}, and v_{Ctc0}. Eliminating

these rows and columns from $\mathbf{A}_n$ and $\mathbf{A}_p$, results in the same reduced-order matrix which we denote by $\mathbf{A}$. The discretization time step for $\mathbf{A}$ is one-sixth of the main period.

The eigenvalues of $\mathbf{A}_n\mathbf{A}_p$ and the eigenvalues of $\mathbf{A}$ are listed in Table 5.2 and Table 5.3, respectively.

Table 5.2: Case 1: Eigenvalues of $\mathbf{A}_n\mathbf{A}_p$, $T = 2\pi/3$ [pu]

Discrete Eigenvalue	Absolute Value	Continuous Eigenvalue	Frequency [Hz]
$-0.48013313 \pm j0.20194118$	0.52087240	$-0.31142652 \pm j1.30990553$	78.59433170
$-0.23593926 \pm j0.33156072$	0.40693961	$-0.42928408 \pm j1.04529775$	62.71786472
$-0.08563509 \pm j0.99632559$	0.99999902	$-0.00000047 \pm j0.79093792$	47.45627536
$0.04260674 \pm j0.53793211$	0.53961680	$-0.29454615 \pm j0.71226133$	42.73567994
$0.42883831 \pm j0.90393112$	1.00049676	$0.00023712 \pm j0.53849704$	32.30982244
$0.62756285 \pm j0.77883923$	1.00021282	$0.00010160 \pm j0.42616070$	25.56964182
$0.76068177 \pm j0.64826641$	0.99944289	$-0.00026608 \pm j0.33698518$	20.21911059
$0.85183065 \pm j0.52475363$	1.00049079	$0.00023428 \pm j0.26361946$	15.81716734
$0.99801154 \pm j0.06081952$	0.99986302	$-0.00006541 \pm j0.02906110$	1.74366598
$0.81911446 + j0.00000000$	0.81911446	$-0.09526925 + j0.00000000$	0.00000000
$0.89282838 + j0.00000000$	0.89282838	$-0.05412584 + j0.00000000$	0.00000000
$0.97624711 + j0.00000000$	0.97624711	$-0.01147803 + j0.00000000$	0.00000000
$0.99749027 + j0.00000000$	0.99749027	$-0.00119981 + j0.00000000$	0.00000000
$0.99761641 + j0.00000000$	0.99761641	$-0.00113944 + j0.00000000$	0.00000000
$0.65383177 + j0.00000000$	0.65383177	$-0.20287728 + j0.00000000$	0.00000000
$0.00000000 + j0.00000000$	0.00000000	$-17.03649054 + j0.00000000$	0.00000000

In both tables there are eigenvalues that have very close frequencies to those in Table 3.1. Therefore, these modes are the subsynchronous modes of oscillation. The tables suggest the existence of unstable modes at 32.30 Hz, 25.56 Hz and 15.82 Hz, because the corresponding eigenvalues lie outside the unit circle.

In Table 5.2 the undampings of the 32.30 Hz and 15.82 Hz are very close and larger than the undamping of 25.56 Hz mode. The undamping of 32.30 Hz is slightly more than that of 15.82 Hz. In Table 5.3 the dominant pole is the 15.82 Hz.

Fig. 5.6 is the shaft torque of the generator-exciter when TCSC is blocked. A small disturbance is introduced in the field current to initiate the subsynchronous interaction. The unstable mode is TM2. Fig. 5.7 shows the torque on the generator-exciter shaft for

Table 5.3: Case 1: Eigenvalues of $\mathbf{A}$ (no zero-sequence variables), $T = \pi/3$ [pu]

Discrete Eigenvalue	Absolute Value	Continuous Eigenvalue	Frequency [Hz]
$-0.07219212 \pm j0.81497168$	0.81816290	$-0.19164847 \pm j1.58436971$	95.06218279
$0.44549746 \pm j0.67965550$	0.81264973	$-0.19810503 \pm j0.94593575$	56.75614481
$0.67615231 \pm j0.73676119$	0.99999950	$-0.00000048 \pm j0.79093793$	47.45627581
$0.84545001 \pm j0.53447024$	1.00022205	$0.00021202 \pm j0.53833247$	32.29994820
$0.90229163 \pm j0.43158311$	1.00019707	$0.00018817 \pm j0.42604450$	25.56266971
$0.93816944 \pm j0.34551758$	0.99977213	$-0.00021763 \pm j0.33697004$	20.21820249
$0.73338012 \pm j0.21818583$	0.76514800	$-0.25562130 \pm j0.27613530$	16.56811773
$0.96296059 \pm j0.27296636$	1.00090146	$0.00086044 \pm j0.26377030$	15.82621774
$0.99918502 \pm j0.03423854$	0.99977146	$-0.00021826 \pm j0.03270927$	1.96255627
$0.90888102 + j0.00000000$	0.90888102	$-0.09123502 + j0.00000000$	0.00000000
$0.94486812 + j0.00000000$	0.94486812	$-0.05415399 + j0.00000000$	0.00000000
$0.98861336 + j0.00000000$	0.98861336	$-0.01093582 + j0.00000000$	0.00000000
$0.99892704 + j0.00000000$	0.99892704	$-0.00102515 + j0.00000000$	0.00000000

the first 5 s when TCSC is set to work with 164° with firing synchronized with the line current. The same disturbance is applied to the field current, although since the TCSC is instantaneously unbalanced, the oscillations start even without additional disturbance. The simulation confirms that in this case TM1 is the dominant unstable mode. The result is also in general agreement with [27] where the dominant unstable mode is TM1, when the compensation level is about 70%[4].

Next we see what happens if we keep the compensation level constant, and change the firing angle of the TCSC. Fig. 5.8 shows how the eigenvalues move as the conduction angle, σ is increased from 0 to 40°. This is equivalent to decreasing the firing angle from 180° to 160°. The reduced-order matrix without the zero-sequence variables is used for the plot. The arrows show the direction of increasing conduction angle.

As is evident from the figure, increasing the conduction angle shifts the eigenvalues further into the unit circle. The eigenvalues of the mechanical modes are located very close to the unit circle and their movement is not seen in Fig. 5.8. Let us zoom into the location of these eigenvalues. Fig. 5.9 shows the pattern of movement of the eigenvalues of the mechanical modes. TM0 is the rigid body mode. The undamping of TM1, TM2, TM3 and TM4 initially

[4]It is not clear if the compensation level in [27] is calculated by (5.45).

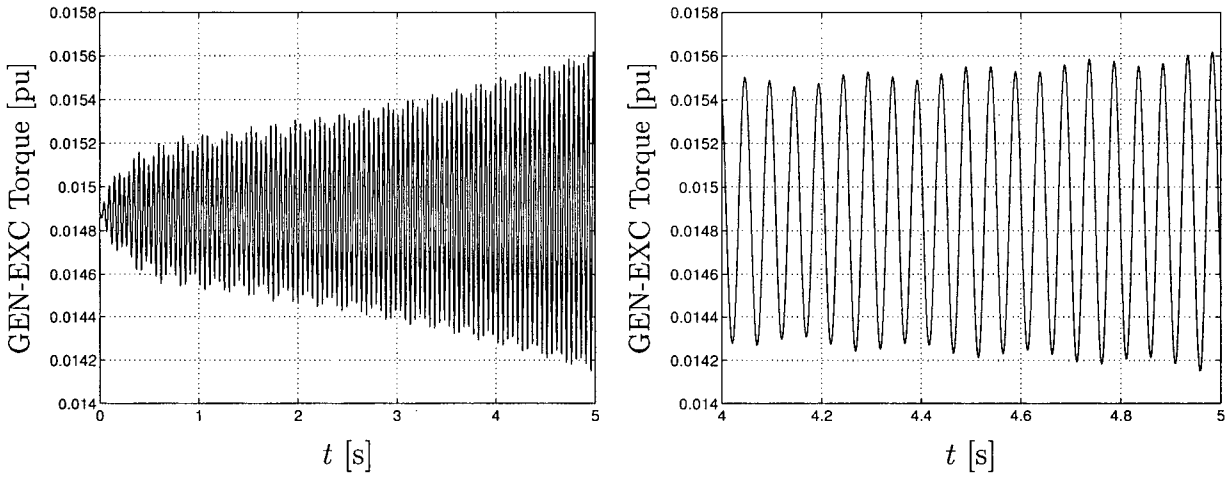

Figure 5.6: Generator-exciter torque, TCSC blocked, Dominant unstable mode TM2

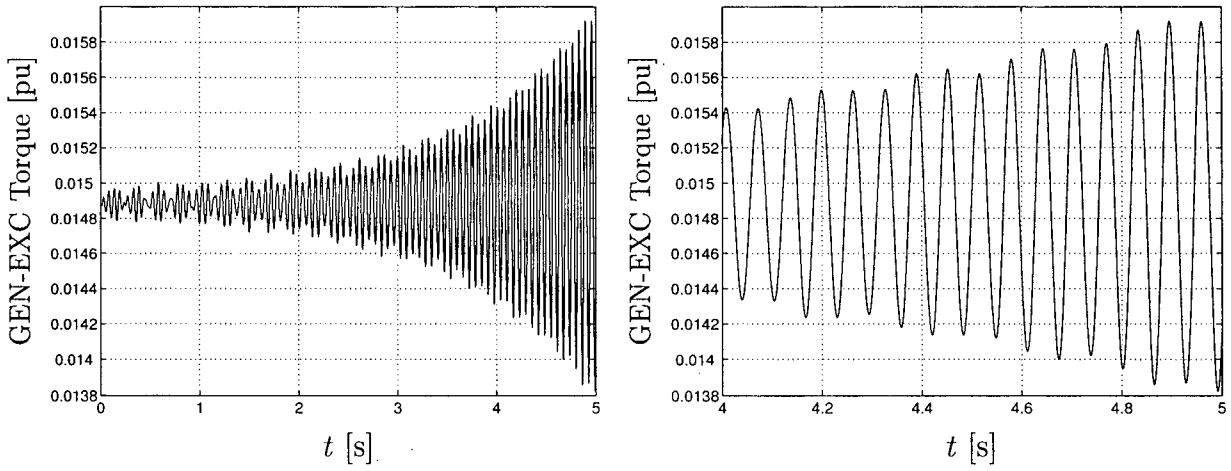

Figure 5.7: Generator-exciter torque, $\alpha = 164°$, dominant unstable mode TM1

increases, then these modes start moving towards the unit circle.

5.3.3 Case Study 2

In this case the total compensation level is set to 55.4% both in the blocked mode and when the TCSC is operating with $\alpha = 164°$. In the blocked mode, that is with fixed series compensation, TM3 with 25.55 Hz is the dominant unstable mode. This is evident from Fig. 5.10 where the speed response of the high-pressure turbine is shown to a small disturbance in the field current.

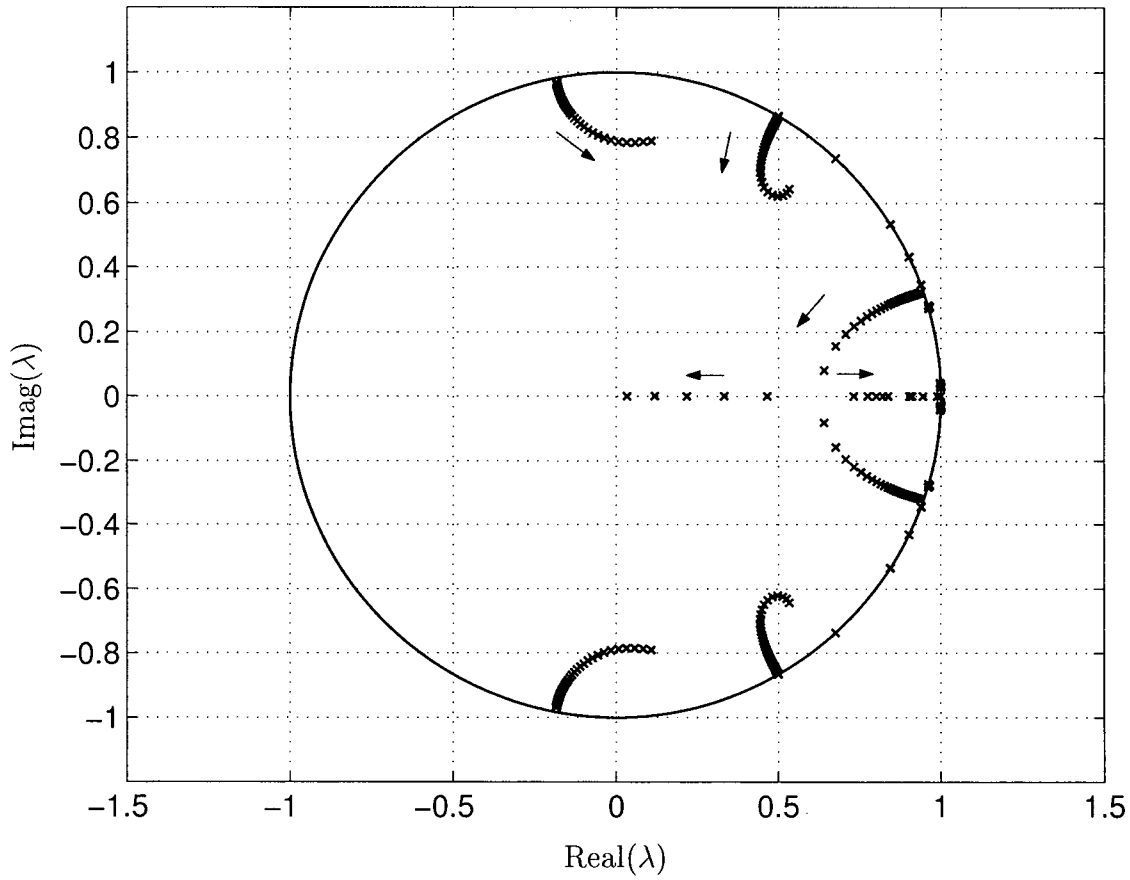

Figure 5.8: Movement of the eigenvalues of $\mathbf{A}$ in the z-plane with σ

To get the same compensation level when TCSC is set to work with $\alpha = 164°$, the parameters of the series compensation are chosen as $X_C = 0.180$ pu, $X_{Ctc} = 0.08505$ pu, and $\kappa = \sqrt{7}$.

The eigenvalues of the discretized model with and without the zero sequence variables are listed in Tables 5.4 and 5.5, respectively. The eigenvalues of $\mathbf{A}_n\mathbf{A}_p$ suggest instability at modes 32.27 Hz, 25.59 Hz and 15.88 Hz, with 32.27 Hz or TM4 being the dominant one. On the other hand, the eigenvalues of $\mathbf{A}$ in Table 5.5, while showing instability in the same modes, suggest the dominant mode to be TM3.

Fig. 5.11 shows the speed of the high-pressure turbine. The dominant unstable mode is TM3, which is consistent with the reduced-order model.

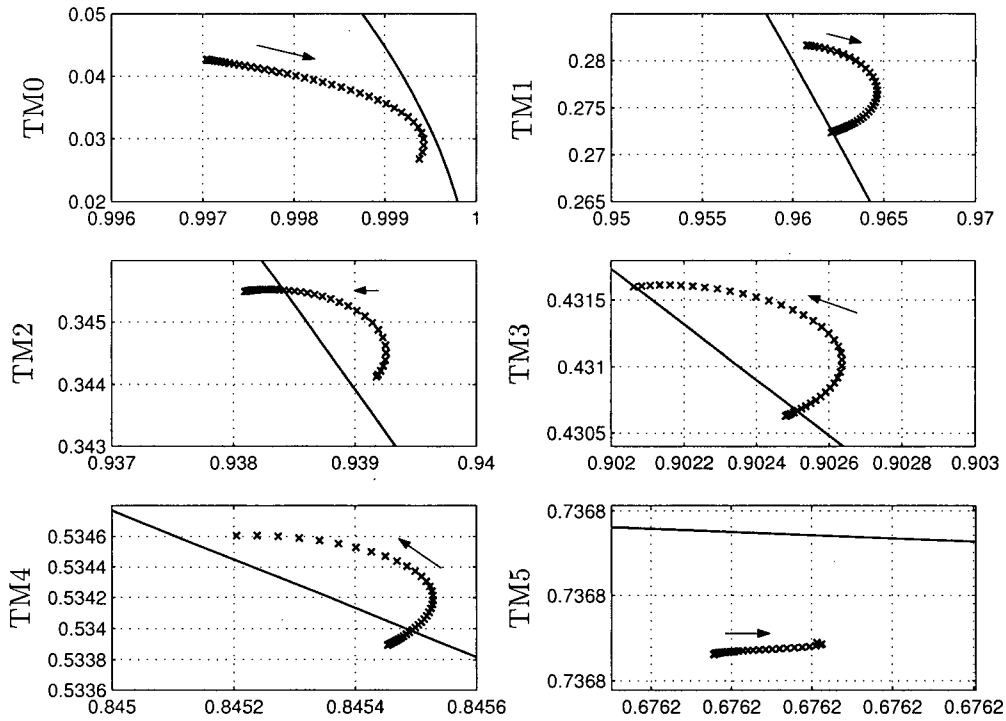

Figure 5.9: Movement of the eigenvalues related to TM0-TM5, with increasing σ

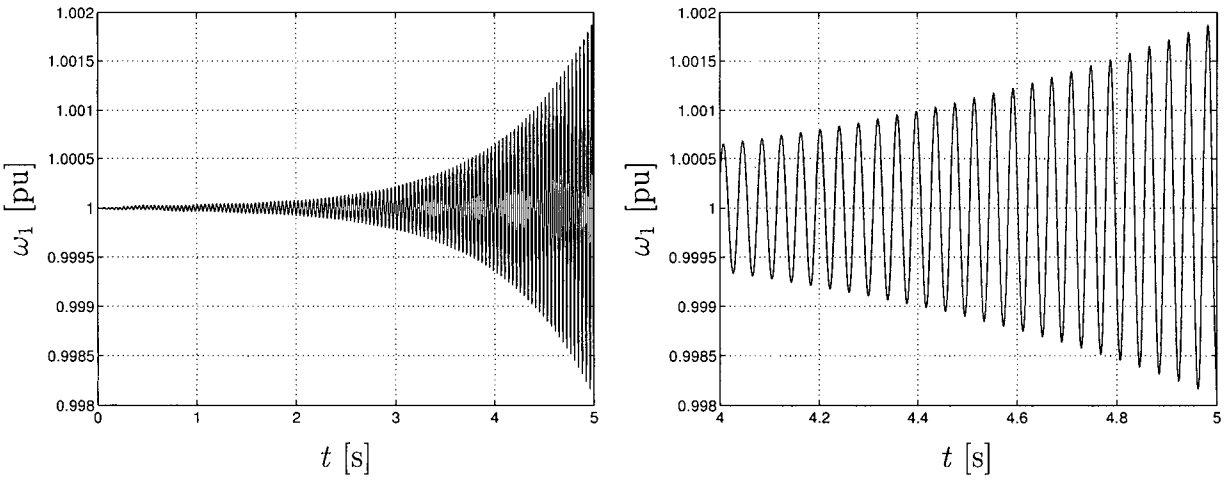

Figure 5.10: High-pressure turbine speed, TCSC blocked, Dominant unstable mode TM3

5.4 Conclusion

A linear discrete state space model for a TCSC compensated system is derived. The model is basically the linearized advance map or Poincaré map of the whole system.

Table 5.4: Case 2: Eigenvalues of $\mathbf{A}_n\mathbf{A}_p$, $T = 2\pi/3$ [pu]

Discrete Eigenvalue	Absolute Value	Continuous Eigenvalue	Frequency [Hz]
$-0.82753894 \pm j0.03000533$	0.82808274	$-0.09007002 \pm j1.48269542$	88.96172504
$-0.15248584 \pm j0.26619720$	0.30677822	$-0.56418686 \pm j0.99837826$	59.90269550
$-0.08563504 \pm j0.99632552$	0.99999895	$-0.00000050 \pm j0.79093790$	47.45627407
$0.43065530 \pm j0.90446907$	1.00176259	$0.00084083 \pm j0.53782450$	32.26947021
$0.44512583 \pm j0.69818451$	0.82800883	$-0.09011264 \pm j0.47900460$	28.74027586
$0.62769255 \pm j0.78023161$	1.00137870	$0.00065783 \pm j0.42652909$	25.59174536
$0.76058602 \pm j0.64851702$	0.99953260	$-0.00022322 \pm j0.33710596$	20.22635747
$0.85075216 \pm j0.52682684$	1.00066266	$0.00031629 \pm j0.26473161$	15.88389634
$0.99535442 \pm j0.06919809$	0.99775688	$-0.00107221 \pm j0.03314054$	1.98843230
$0.89301021 + j0.00000000$	0.89301021	$-0.05402861 + j0.00000000$	0.00000000
$0.99626227 + j0.00000000$	0.99626227	$-0.00178798 + j0.00000000$	0.00000000
$0.98009184 + j0.00000000$	0.98009184	$-0.00960134 + j0.00000000$	0.00000000
$0.99853667 + j0.00000000$	0.99853667	$-0.00069920 + j0.00000000$	0.00000000
$0.00000000 + j0.00000000$	0.00000000	$-16.84392458 + j0.00000000$	0.00000000
$0.20179971 + j0.00000000$	0.20179971	$-0.76417273 + j0.00000000$	0.00000000
$0.83222021 + j0.00000000$	0.83222021	$-0.08769033 + j0.00000000$	0.00000000

Table 5.5: Case 2: Eigenvalues of $\mathbf{A}$ (no zero-sequence variables), $T = \pi/3$ [pu]

Discrete Eigenvalue	Absolute Value	Continuous Eigenvalue	Frequency [Hz]
$-0.02562151 \pm j0.93351122$	0.93386276	$-0.06534181 \pm j1.52620280$	91.57216773
$0.39248558 \pm j0.60039444$	0.71729939	$-0.31728681 \pm j0.94711396$	56.82683748
$0.67615232 \pm j0.73676115$	0.99999948	$-0.00000050 \pm j0.79093790$	47.45627420
$0.84620693 \pm j0.53418856$	1.00071154	$0.00067922 \pm j0.53771931$	32.26315875
$0.81683493 \pm j0.42598168$	0.92123813	$-0.07833929 \pm j0.45903609$	27.54216546
$0.90270880 \pm j0.43233805$	1.00089928	$0.00085836 \pm j0.42652251$	25.59135088
$0.93811596 \pm j0.34567407$	0.99977603	$-0.00021390 \pm j0.33712796$	20.22767736
$0.96209553 \pm j0.27392794$	1.00033210	$0.00031708 \pm j0.26487865$	15.89271904
$0.99821796 \pm j0.03499962$	0.99883135	$-0.00111663 \pm j0.03346813$	2.00808785
$0.94498909 + j0.00000000$	0.94498909	$-0.05403173 + j0.00000000$	0.00000000
$0.99927142 + j0.00000000$	0.99927142	$-0.00069600 + j0.00000000$	0.00000000
$0.99000570 + j0.00000000$	0.99000570	$-0.00959187 + j0.00000000$	0.00000000
$0.91237852 + j0.00000000$	0.91237852	$-0.08756737 + j0.00000000$	0.00000000

The eigenvalues of the linear model are able to predict the stability of the subsynchronous modes. With the zero sequence variables omitted, the eigenvalue results are better able to predict the dominant unstable mode. This is confirmed by comparison with detailed

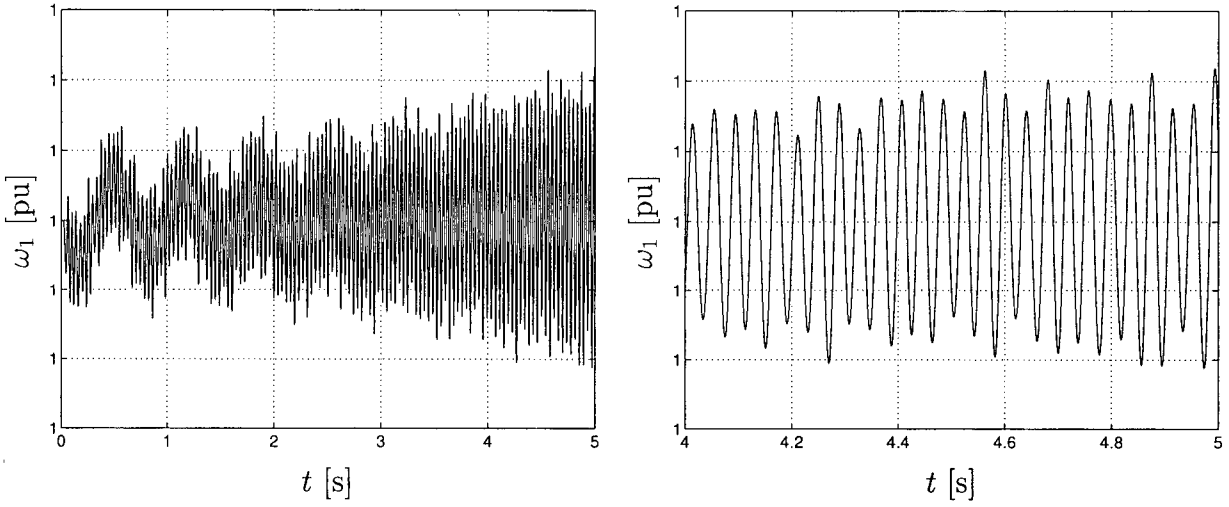

Figure 5.11: High-pressure turbine speed, $\alpha = 164°$, Dominant unstable mode TM3

nonlinear transient simulation. One possible reason is that in obtaining the linear system parameters, an approximate orbit has been used.

The model also takes into account the variations of the firing instants. Therefore it can be used to make small changes in the firing angles to increase the damping of the subsynchronous modes. This is the subject of the next chapter, where the model is used to adjust the gains of a feedback controller for damping subsynchronous oscillations.

Chapter 6

SSR Damping Controller for TCSC

The SSR mitigation property of the thyristor controlled series capacitor in open-loop operation has two reasons behind it:

1. Detuning: The reactance of TCSC, similar to that of a tuned LC filter, can become inductive at low frequencies.
2. Passive damping: Although TCSC does not have large resistive components, it can appear to be resistive at a subsynchronous frequency. This is due to a regenerative behaviour, which occurs at the switching frequency, resulting in a drain of energy out of the subsynchronous modes [64](see Chapter 4).

However, both of the above characteristics are subject to change, depending on the firing policy. In particular, TCSC shows a capacitive-resistive behaviour throughout the subsynchronous region when the firing is synchronized with the line current[62, 64]. Also, there is no guarantee that the virtual resistance provided by the TCSC is large enough to neutralize the negative damping of a subsynchronous mode. This was observed in the examples of the last chapter on the IEEE First Subsynchronous Resonance Benchmark Model, where the TCSC with open-loop firing was able to reduce the undamping and change the frequency of the dominant unstable mode, but the problem was not totally solved.

So, in order to make sure that the subsynchronous modes are well damped, a closed-loop control is necessary. The linear discrete model developed for a TCSC compensated system in the last chapter, given by (5.16) and (5.17), advances the system states to one-sixth of

the main period forward in time. Since dependence of the small signal variation of the state at the end of the time step is expressed not only in terms of the variation of the state at the beginning of the time step, but also in terms of the variation of the firing angle, the model can be used to adjust the gains of a feedback stabilizing controller.

In this chapter, a controller is designed to vary the firing angles near a steady-state value to add damping to subsynchronous modes in the First SSR Benchmark Model. The performance of two different discretization time steps are compared. In the end, a comparison is provided with other research work that has been done in this area.

6.1 Controller Design

The first case study of the previous chapter, where TM1 is the dominant unstable mode, is considered here for the design of a closed-loop firing scheme. Pole placement with state feedback is the design method.

A simplified block diagram of the closed-loop system is shown in Fig. 6.1.

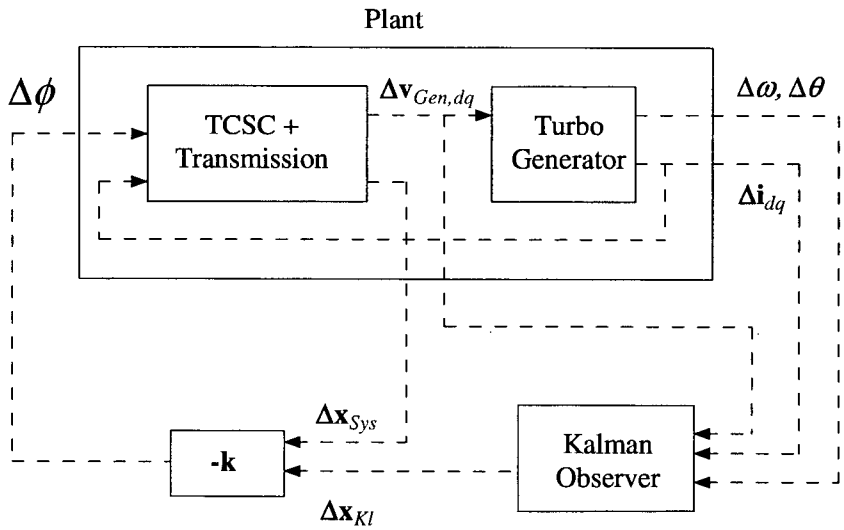

Figure 6.1: Simplified block diagram of the closed-loop system

The area enclosed in the rectangle, the "plant", is the system we have linearized and discretized in the last chapter. Inside the plant the turbo-generator is identified from the TCSC and transmission system in order to show the input to the Kalman observer which

exclusively observes the turbo-generator states. The output of the Kalman observer is termed $\Delta\mathbf{x}_{Kl}$. The vector of small signal changes in the fixed and the thyristor controlled capacitor voltages is denoted by $\Delta\mathbf{x}_{Sys} = [\Delta v_{Cd} \quad \Delta v_{Cq} \quad \Delta v_{Ctcd} \quad \Delta v_{Ctcq}]^t$. The change in the firing angle effected by the controller is $\Delta\phi$. The line currents and the generator terminal voltages in the d and q axes are denoted by $\Delta\mathbf{i}_{dq}$ and $\Delta\mathbf{v}_{Gen,dq}$, respectively. Finally, $\Delta\theta$ and $\Delta\omega$ are the generator rotor angle and speed.

To adjust the feedback gain vector $\mathbf{k}$ the reduced-order model with 22 states is used. This model generally results in smaller gains for the controller compared with the model where the zero sequence variables are retained.

Table 6.1 lists the eigenvalues before and after the controller is added. The open-loop eigenvalues are the same as those in Table 5.3. The eigenvalues with absolute values greater than 1 or very close to the unit circle are shifted radially inside the unit circle, with the rest of the eigenvalues unchanged. The feedback gain vector is given in (6.1).

$$\begin{aligned}\mathbf{k} = [\; & -0.586 \quad -0.424 \quad -0.543 \quad -0.553 \quad -0.351 \quad -0.352 \\ & 0.114 \quad -0.078 \quad 0.193 \quad 0.093 \\ & -9.270 \quad 13.246 \quad -16.196 \quad 15.716 \quad 14.606 \quad -0.661 \\ & 0.452 \quad 0.596 \quad 3.884 \quad 2.615 \quad -8.751 \quad 0.944]\end{aligned} \tag{6.1}$$

Table 6.2 shows the corresponding continuous-time modal dampings and frequencies of the open-loop and closed-loop systems. The conversion explained in Section 5.3.1 is used to obtain the continuous-time counterparts of the discrete eigenvalues. The modal dampings are the real parts of the continuous eigenvalues multiplied by $\omega_B = 2\pi 60$ rad/s. This is because in the state space model, time is in per unit based on $t_B = 1/\omega_B$ s.

For this example, it is assumed that the states Δi_d, Δi_q, Δv_{Cd}, Δv_{Cq}, Δv_{Ctcd}, Δv_{Ctcq}, $\Delta\omega$, $\Delta\theta$ are directly measured. The discrete Kalman estimator is designed for the generator separately, taking the terminal voltages of the generator, Δv_{Gend} and Δv_{Genq} as the inputs, and Δi_d, Δi_q, $\Delta\omega$ and $\Delta\theta$ as the outputs as shown in Fig. 6.1. The remaining states, that is the four rotor currents, the speeds and the angles of the other rotors are estimated. The input and measurement noise covariances in the description of the Kalman filter, $\mathbf{Q_w}$ and $\mathbf{R_v}$ (see Section 2.7.1), are used as design parameters. They are both set to unity.

Table 6.1: Shifting the discrete eigenvalues by feedback

mode	Eigenvalues of **A**	Absolute value	Eigenvalues of **A − bk**	Absolute Value
1, 2	$-0.07219212 \pm j0.81497168$	0.81816290	$-0.07219212 \pm j0.81497168$	0.81816290
3, 4	$0.44549746 \pm j0.67965550$	0.81264973	$0.44549746 \pm j0.67965550$	0.81264973
5, 6	$0.67615231 \pm j0.73676119$	0.99999950	$0.67598359 \pm j0.73657735$	0.99974997
7, 8	$0.84545001 \pm j0.53447024$	1.00022205	$0.84151725 \pm j0.53198405$	0.99556934
9, 10	$0.90229163 \pm j0.43158311$	1.00019707	$0.89856564 \pm j0.42980090$	0.99606678
11, 12	$0.93816944 \pm j0.34551758$	0.99977213	$0.93411586 \pm j0.34402469$	0.99545237
13, 14	$0.73338012 \pm j0.21818583$	0.76514800	$0.73338012 \pm j0.21818583$	0.76514800
15, 16	$0.96296059 \pm j0.27296636$	1.00090146	$0.94491063 \pm j0.26784982$	0.98214032
17, 18	$0.99918502 \pm j0.03423854$	0.99977146	$0.99485523 \pm j0.03409018$	0.99543913
19	$0.90888102 + j0.00000000$	0.90888102	$0.90888102 + j0.00000000$	0.90888102
20	$0.94486812 + j0.00000000$	0.94486812	$0.94486812 + j0.00000000$	0.94486812
21	$0.98861336 + j0.00000000$	0.98861336	$0.98861336 + j0.00000000$	0.98861336
22	$0.99892704 + j0.00000000$	0.99892704	$0.99892704 + j0.00000000$	0.99892704

Table 6.2: Comparison of open and closed loop dampings in continuous domain

mode	Modal Damping (open loop)	Modal Damping (closed loop)	Frequency [Hz]
1, 2	−72.24977265	−72.24977265	±95.06218
3, 4	−74.68383654	−74.68383654	±56.75614
5, 6	−0.00018004	−0.09002162	±47.45628
7, 8	0.07992911	−1.59858213	±32.29995
9, 10	0.07093759	−1.41875178	±25.56267
11, 12	−0.08204403	−1.64088070	±20.21820
13, 14	−96.36696020	−96.36696020	±16.56812
15, 16	0.32437953	−6.48759054	±15.82622
17, 18	−0.08228342	−1.64566831	±1.96256
19	−34.39479205	−34.39479205	0.00000
20	−20.41557182	−20.41557182	0.00000
21	−0.38647246	−0.38647246	0.00000
22	−4.12270810	−4.12270810	0.00000

Because of the switching action in the circuit, a 360 Hz frequency is present in the waveforms. The dynamic model derived here does not take this into account. If the estimator uses the same time step, 1/360 s as the model for the controller, *aliasing* occurs, and the 360 Hz appears as DC. To avoid this effect for the design of the Kalman filter, a time step of

1/2400 s is used to be able to capture the 360 Hz component. The output from the Kalman observer is passed through a notch filter, tuned for 360 Hz, before the variables are fed into the controller. The notch filter is formed by discretizing the following transfer function

$$H_{notch}(s) = \frac{s^2 + 0.5s + 36}{s^2 + 5s + 36} \tag{6.2}$$

Fig. 6.2 shows the Bode diagram of the filter in equation (6.2). The frequency axis is in Hz, so the frequency of 360 Hz corresponds to 6 pu in equation (6.2).

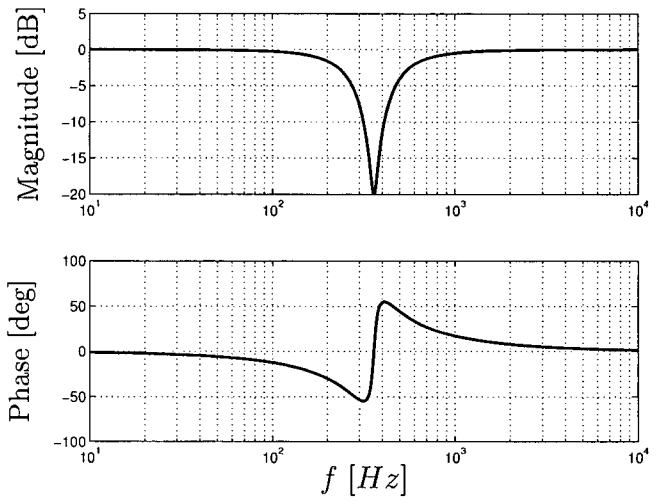

Figure 6.2: Bode diagram of the notch filter

Fig. 6.3 is the detailed block diagram of the nonlinear system, together with the controller and Kalman estimator. The continuous signals are shown with solid lines. The discrete signals are shown with broken lines. As mentioned above, the Kalman observer uses a faster sampling rate. This is indicated in the diagram by using dotted lines for faster signals versus dashed lines for the slower ones.

In Fig. 6.3, $\bar{\alpha}$ stands for the steady-state firing angle. v^*_{Gend}, v^*_{Genq} are the steady-state waveforms of the generator terminal voltage in the d and q axes, respectively. Also

$$\mathbf{x}^*_{Sys} = [v^*_{Cd} \;\; v^*_{Cq} \;\; v^*_{Ctcd} \;\; v^*_{Ctcq}]^t \tag{6.3}$$

$$\mathbf{y}^*_{Gen} = [i^*_d \;\; i^*_q \;\; \omega^* \;\; \theta^*]^t \tag{6.4}$$

are the steady-state waveforms of those variables. $v_{\infty d}$ and $v_{\infty q}$ are the infinite bus voltages. t_{q1}, t_{q2}, t_{q3} and t_{q4} are the turbine torques, and v_F is the field voltage.

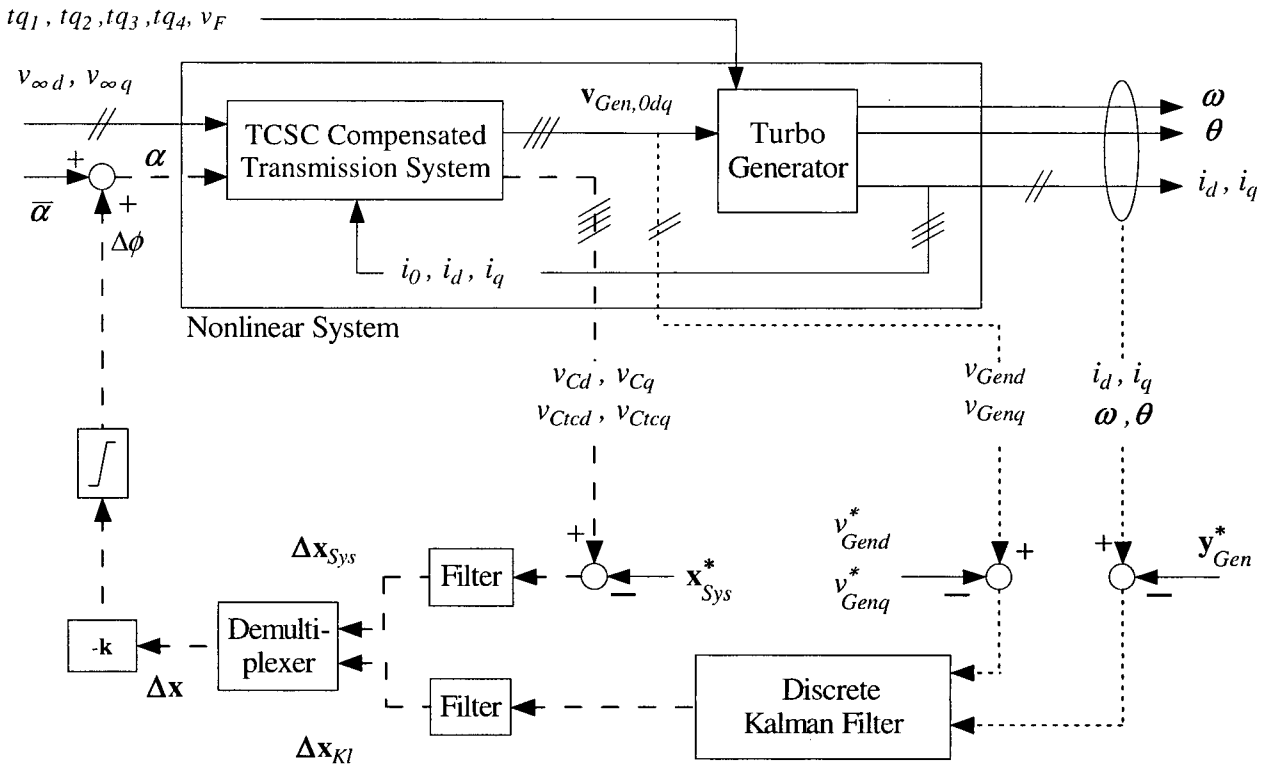

Figure 6.3: Block diagram of the system with the controller and Kalman observer

The variation in the state, $\Delta\mathbf{x}$ is formed by setting the elements of $\Delta\mathbf{x}_{Sys}$ and $\Delta\mathbf{x}_{Kl}$ in order, corresponding to (5.27) without the zero-sequence variables. A limiter is used after the gain block, to avoid firing angle deviations larger than 5°.

6.1.1 Simulation Results

The time-domain simulation verifies the results of the eigenvalue analysis. The detailed non-linear model is used for simulation. A three-phase fault to ground at busbar B (see Fig. 2.4) is simulated. Fig. 6.4 shows the speed deviation of the exciter rotor for 3 seconds without the controller. The simulation starts at steady state at the time when the phase a line current has a positive to negative zero crossing. The fault is applied at $t = 1/120$ s ($= \pi$ pu), and the fault clearing process starts 0.075 seconds later, with the circuit breaker in each phase interrupting the respective current flow in its zero crossing.

Then the controller is activated to make adjustments in the firing delay angles of the

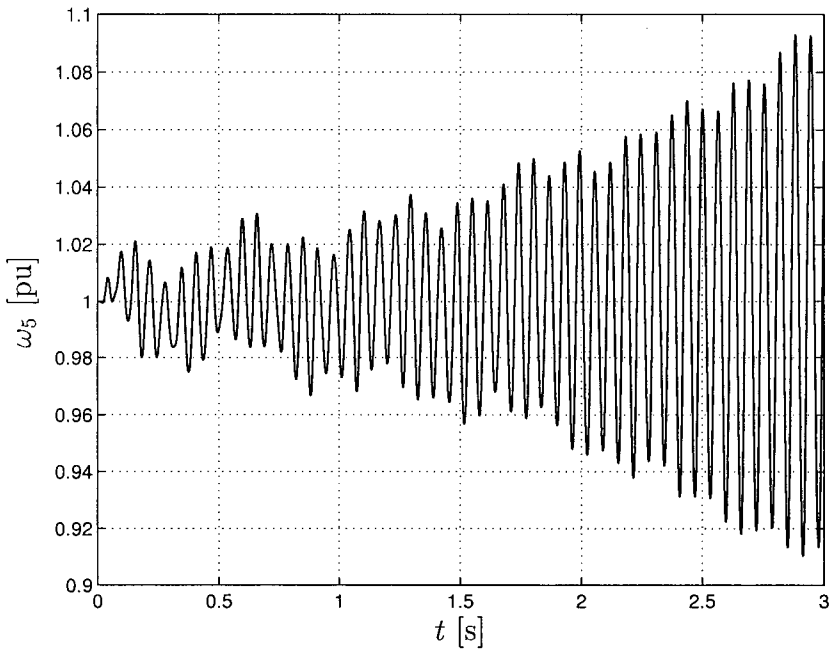

Figure 6.4: Exciter rotor speed deviation with open loop firing control

TCSC thyristors. The controller generates an output at each line current zero-crossing for the next immediate firing to follow. For example, the $\Delta\phi$ for the negative pulse in phase b is determined at the time of positive-to-negative zero-crossing in i_a, that for the positive pulse in phase a at the time of negative-to-positive zero-crossing in i_c, and so on (see Fig. 5.1).

The steady-state firing angles of the thyristors in each phase are synchronized with the line current zero-crossings in the same phase.

Fig. 6.5 shows that the 15.82 Hz mode is well damped even after a major disturbance. Note that the scale of Fig. 6.5 is different from that of Fig. 6.4.

Fig. 6.6 shows the variations of the firing angle about the steady-state value of 164° with the controller in action. The time domain simulations are conducted using MATLAB® ODE solvers for stiff problems.

There is a small 360 Hz component present in the waveforms at steady-state conditions, as shown for Δi_d in Fig. 6.7. This unmodelled dynamic behaviour is quite insignificant. However, it may get amplified through feedback gain, so a designer should be aware of it.

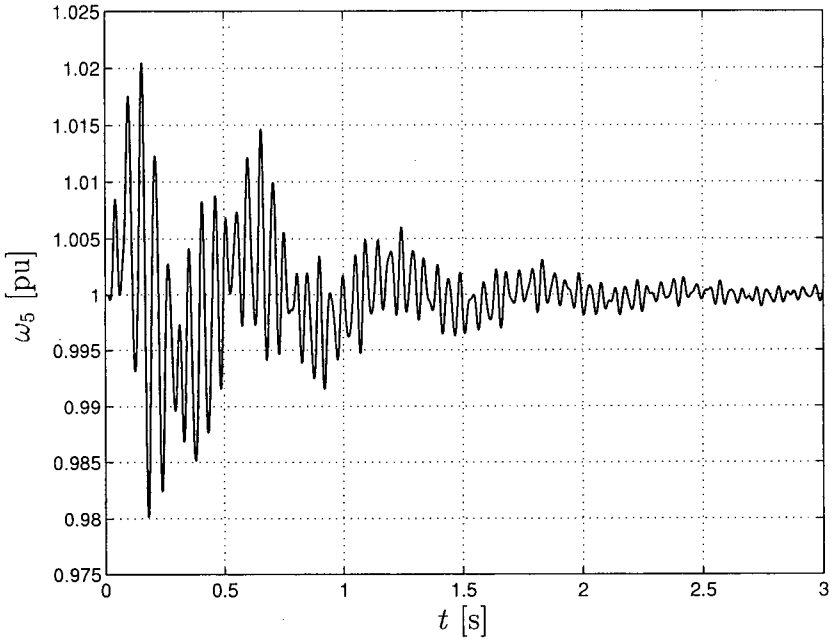

Figure 6.5: Exciter rotor speed deviation with closed loop firing control

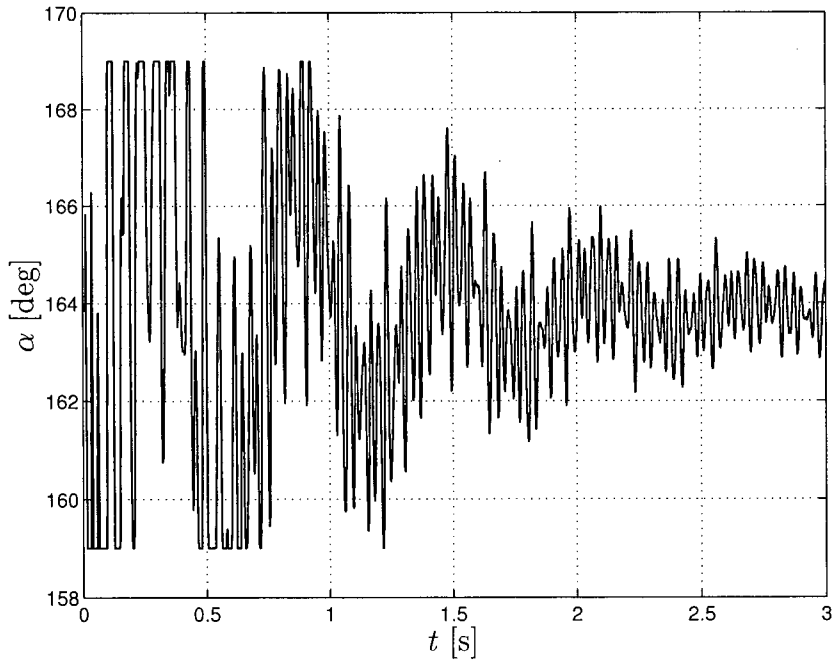

Figure 6.6: Control of the firing angle

6.1.2 Eigenvalue Sensitivity Analysis

The simulations in the previous section show that the controller is able to stabilize the system in the face of a major disturbance. Therefore, the approximations made in order to arrive at

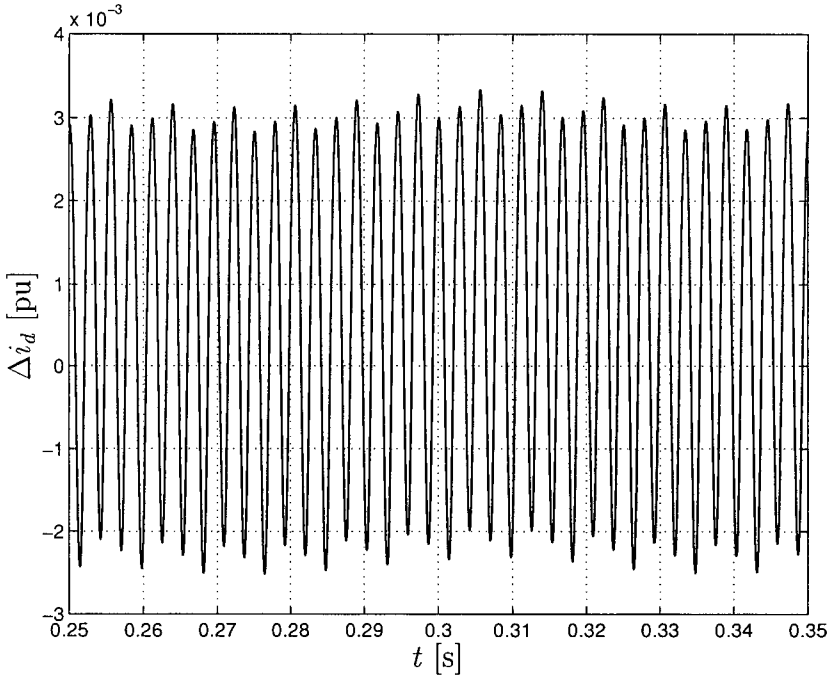

Figure 6.7: Variations of i_d during steady state

the linear model, namely using the ideal steady-state waveforms instead of the exact periodic orbit, and omitting the zero-sequence variables, are valid.

The *participation matrix* [65] is a measure of the sensitivity of the eigenvalues to the elements of the state matrix. In order to define this matrix, the concepts of right and left eigenvectors are needed. A discussion on these eigenvectors and the derivation of the participation matrix is provided in Appendix D. An advantage of the participation matrix is that it is independent of the scaling and units associated with the state variables.

The magnitudes of the participation factors of the state matrix of our case study related to the subsynchronous modes are listed in Table 6.3.

As an example, the value listed under TM4 and i_d, that is $2.0798e-3$, means

$$\left|\frac{\partial \lambda_7}{\partial a_{11}}\right| = \left|\frac{\partial \lambda_8}{\partial a_{11}}\right| = 0.0020798 \tag{6.5}$$

where λ_7 and λ_8 are the eigenvalues associated with the mode TM4, and a_{11} is the element in the first row and first column of $\mathbf{A}$.

From the numbers in the table, it is apparent that the subsynchronous eigenvalues are

Table 6.3: Participation factors related to subsynchronous modes

	TM1	TM2	TM3	TM4	TM5
i_d	$1.8548e-2$	$6.8422e-4$	$1.3507e-3$	$2.0798e-3$	$3.6009e-7$
i_q	$1.2656e-2$	$9.3998e-4$	$2.3662e-3$	$2.3617e-3$	$2.9709e-7$
i_F	$4.0454e-3$	$1.1970e-4$	$2.0466e-4$	$2.6758e-4$	$3.6242e-8$
i_D	$1.5918e-2$	$5.9032e-4$	$1.1589e-3$	$1.7893e-3$	$3.1044e-7$
i_Q	$7.2925e-3$	$5.3163e-4$	$1.3096e-3$	$1.2779e-3$	$1.5905e-7$
i_G	$2.2042e-3$	$1.5838e-4$	$3.8691e-4$	$3.7557e-4$	$4.6528e-8$
v_{Cd}	$6.4686e-4$	$5.7808e-5$	$1.8051e-4$	$2.3967e-4$	$7.7231e-8$
v_{Cq}	$2.8277e-4$	$2.1546e-5$	$5.6273e-5$	$6.4553e-5$	$2.2283e-8$
v_{Ctcd}	$9.2276e-4$	$9.9458e-5$	$3.4867e-4$	$4.6529e-4$	$7.3105e-8$
v_{Ctcq}	$1.3786e-3$	$1.3296e-4$	$4.1813e-4$	$5.0786e-4$	$7.9242e-8$
ω_1	$7.4008e-2$	$1.4995e-2$	$2.4309e-1$	$2.2754e-2$	$1.2821e-1$
ω_2	$6.9269e-2$	$8.6823e-3$	$4.7444e-2$	$1.0158e-4$	$3.4634e-1$
ω_3	$1.2848e-1$	$2.5653e-3$	$1.1963e-1$	$7.1366e-2$	$2.4527e-2$
ω_4	$1.6416e-2$	$1.8445e-2$	$2.0297e-2$	$2.9212e-1$	$8.7749e-4$
ω	$1.6148e-1$	$1.6144e-2$	$6.3354e-2$	$1.1169e-1$	$3.8572e-5$
ω_5	$4.8014e-2$	$4.3898e-1$	$5.7404e-3$	$1.6176e-3$	$6.8237e-8$
θ_1	$7.4009e-2$	$1.4995e-2$	$2.4309e-1$	$2.2754e-2$	$1.2821e-1$
θ_2	$6.9269e-2$	$8.6823e-3$	$4.7444e-2$	$1.0158e-4$	$3.4634e-1$
θ_3	$1.2848e-1$	$2.5654e-3$	$1.1963e-1$	$7.1366e-2$	$2.4527e-2$
θ_4	$1.6416e-2$	$1.8445e-2$	$2.0297e-2$	$2.9212e-1$	$8.7749e-4$
θ	$1.6378e-1$	$1.6344e-2$	$6.3936e-2$	$1.1235e-1$	$3.8643e-5$
θ_5	$4.8015e-2$	$4.3898e-1$	$5.7404e-3$	$1.6176e-3$	$6.8237e-8$

more sensitive to the rotor speeds and angles. This is expected because these modes are primarily related to the mechanical subsystem. Specifically, TM5 is very insensitive to the electrical states.

Note that the participation matrix gives the sensitivity of the eigenvalues with respect to the diagonal elements of $\mathbf{A}$. The sensitivity to the off-diagonal elements are also readily available using the right and left eigenvectors as explained in Appendix D.

6.2 Performance Comparison of Two Sampling Rates

The controller described in the previous section updates its output six times in one cycle of 60 Hz. Here we want to compare the performance of two different sampling rates. That is, we would like to see how the dampings of the subsynchronous modes are affected if the control action updates twice in one main period instead of 6 times. This means in one discretization time step 3 current pulses are included, and the same control action, $\Delta\phi$ is applied to them.

In order to obtain the linear model with the new sampling rate, notice that it contains three time spans of the model with the smaller time step, $T = \pi/3$ pu. Let us denote these time spans by $[0 \;\; \pi/3]$, $[\pi/3 \;\; 2\pi/3]$, and $[2\pi/3 \;\; \pi]$. Using the model derived for $T = \pi/3$ pu, the small signal change at the end of each of the time segments is

$$\Delta\mathbf{x}(\pi) = \mathbf{A}\Delta\mathbf{x}(\frac{2\pi}{3}) + \mathbf{b}\Delta\phi \tag{6.6}$$

$$\Delta\mathbf{x}(\frac{2\pi}{3}) = \mathbf{A}\Delta\mathbf{x}(\frac{\pi}{3}) + \mathbf{b}\Delta\phi \tag{6.7}$$

$$\Delta\mathbf{x}(\frac{\pi}{3}) = \mathbf{A}\Delta\mathbf{x}(0) + \mathbf{b}\Delta\phi \tag{6.8}$$

In writing (6.6)-(6.8), the same firing angle change has been applied to the pulses. Combining the above three yields the linear model that advances the system state to half a period later

$$\begin{aligned}\Delta\mathbf{x}(\pi) &= \mathbf{A}^3\Delta\mathbf{x}(0) + [\mathbf{A}^2\mathbf{b} + \mathbf{A}\mathbf{b} + \mathbf{b}]\Delta\phi \\ &\triangleq \mathbf{A}_3\Delta\mathbf{x}(0) + \mathbf{b}_3\Delta\phi\end{aligned} \tag{6.9}$$

To have a common base for comparison, we keep the same gains used for the damping controller with $T = \pi/3$ pu. Therefore, the closed-loop system in this case becomes $\mathbf{A}^3 - [\mathbf{A}^2\mathbf{b} + \mathbf{A}\mathbf{b} + \mathbf{b}]\mathbf{k}$. Let us compare the eigenvalues of this matrix with the eigenvalues of $\mathbf{A} - \mathbf{b}\mathbf{k}$ which is the closed loop system with sampling rate of $\pi/3$ pu. These are given in Table 6.4 and Table 6.5, respectively. Only the subsynchronous modes are listed in the tables.

The eigenvalues of the system with larger time step are slightly less damped. Fig. 6.8

Table 6.4: Eigenvalues of $\mathbf{A} - \mathbf{bk}$, $T = \pi/3$ [pu]

Discrete Eigenvalue	Absolute Value	Modal Damping	Frequency [Hz]
$0.67598359 \pm j0.73657735$	0.99974997	−0.09002162	47.4563
$0.84151725 \pm j0.53198405$	0.99556934	−1.59858213	32.2999
$0.89856564 \pm j0.42980090$	0.99606678	−1.41875178	25.5627
$0.93411586 \pm j0.34402469$	0.99545237	−1.64088070	20.2182
$0.94491063 \pm j0.26784982$	0.98214032	−6.48759054	15.8262
$0.99485523 \pm j0.03409018$	0.99543913	−1.64566831	1.9626

Table 6.5: Eigenvalues of $\mathbf{A}_3 - \mathbf{b}_3\mathbf{k}$, $T = \pi$ [pu]

Discrete Eigenvalue	Absolute Value	Modal Damping	Frequency [Hz]
$-0.79193606 \pm j0.60993025$	0.99958873	−0.04936226	47.4658
$-0.12655312 \pm j0.98110893$	0.98923729	−1.29852530	32.4500
$0.22232705 \pm j0.96403749$	0.98934200	−1.28582414	25.6712
$0.47932453 \pm j0.86232066$	0.98658447	−1.62075920	20.3108
$0.63104641 \pm j0.71034983$	0.95016653	−6.13416142	16.1278
$0.98106716 \pm j0.10161014$	0.98631506	−1.65353294	1.9710

shows the damping of the TM1 mode with two different sampling rates. The transient simulation confirms that the damping is less in case of slower control update.

It must be noted that this comparison shows the general trend with different sampling rates. If the control parameters are optimized by repeating the design cycle for each of the models, the controller performance can be improved in each case.

6.3 Comparison with Other Research Work

The work contained here, as in the case of [27, 32], is based on the Poincaré mapping techniques, elaborated in [21, 45, 51], and particularly relevant to this work, in [35].

References [27, 32] have derived stand-alone continuous LTI models for the TCSC itself. They first linearize the advance map of a single-phase TCSC by taking a time step equal to $T = \pi$ pu. This is shown in Appendix A. Then, the maps for the three phases are stacked together, and converted to the dq reference frame. Finally, the equations are converted from

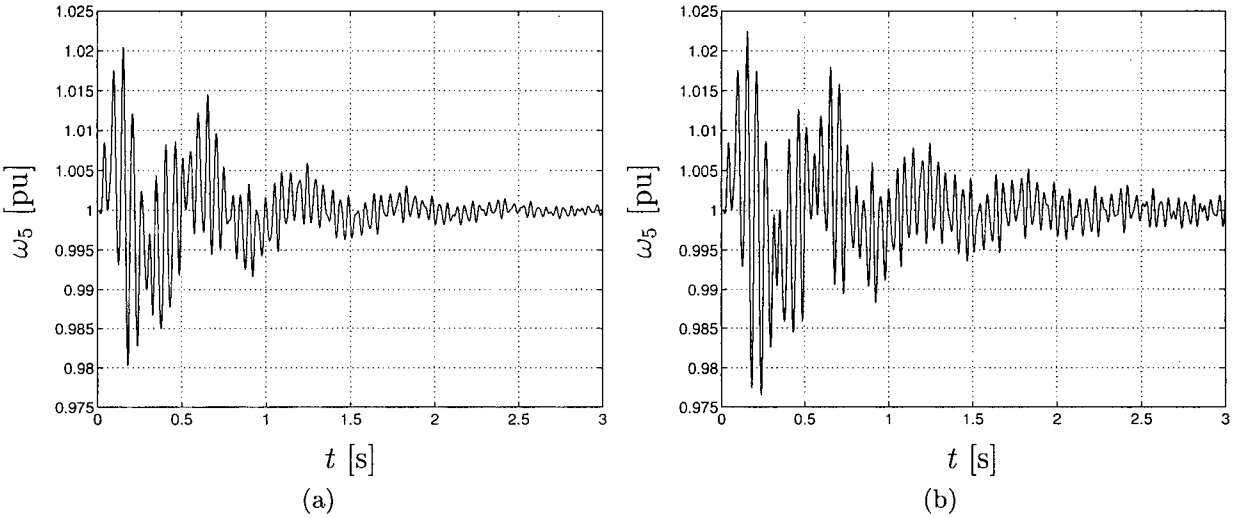

Figure 6.8: Damping of TM1 mode with (a) $T = \pi/3$ [pu] and (b) $T = \pi$ [pu]

discrete to continuous.

In the last section the damping of the subsynchronous modes with the sampling step of $T = \pi$ were found to be slightly less than the dampings obtained by $T = \pi/3$ pu. However, in [27, 32], the line currents are assumed to be the forcing functions and, therefore, independent quantities. This approach ignores the loading effect of the TCSC on the line currents, which has an adverse effect on the damping of subsynchronous oscillations. The models haven't been used to design damping controllers, and therefore, a rigorous comparison cannot be made.

Reference [66] develops a discrete model for a TCSC compensated transmission system by assuming the generator terminal voltages to be constant. Again, the model is not used for damping controller design.

Our development yields a discrete state space model for a TCSC compensated system, where the line currents are among the state variables. The model also includes the turbo-generator dynamics without the assumption of constant terminal voltages.

Furthermore, similar to [27, 32, 66] but more general, the dependence of small signal variations of the state variables on the deviation of the firing angles is taken into account.

Our model is basically an extension of the model developed in [35]. That model is geared towards eigenvalue analysis, for which only the **A**-matrix of the homogenous linearized system (see (5.10)) is needed. Therefore, firing angle deviations are neglected. Our main contribution to the model presented in [35] is the inclusion of firing angle deviations, through the calculation of the coefficients (**b**) of the forcing function in the form of

$$\Delta\mathbf{x}(n+1) = \mathbf{A}(n)\,\Delta\mathbf{x}(n) + \mathbf{b}(n)\,u(n) \tag{6.10}$$

where n is the discrete time corresponding to $t = n\Delta t$, with Δt being the discretization step, and u is the firing angle deviation. Sampling the state with a frequency higher than the frequency of the repetition of the waveforms will generally yield periodically varying **A** and **b** matrices, indicated by (n). The only difference between the parameters of the model developed for a region containing a positive pulse, and a region containing a negative pulse, was found to be in the zero-sequence variables.

There are publications that discuss SSR damping controller design for TCSC. The state space model used for controller design in [34] is obtained by approximating the steady-state reactance of the TCSC (Fig. 2.8), using an exponential function of the form $X_{TCSC} = X_C + K_\beta e^{-\alpha/\alpha_c}$, where K_β and α_c are chosen to fit the function into the capacitive region of Fig. 2.8. This model is converted to continuous-time, before interfacing it with the turbine-generator model, and then used to design a state feedback controller. The system analyzed there is the First Subsynchronous Resonance Benchmark Model. Self damping of 0.2 per unit and mutual damping of 0.3 per unit is added to each shaft section, while the dampings provided in the standard benchmark model [38], are in terms of modal dampings at no load.

In our work to be conservative, we have assumed the modal dampings to be the same under loaded conditions, and calculated the self dampings by use of the method provided in [18]. The mutual dampings are neglected. From a comparison of the plots, the damping that is observed in our simulations is more than the damping reported in [34].

Reference [67] introduces a method for designing a damping controller for TCSC by combining Fourier analysis with torque per unit method, which basically traces the effect of a small sinusoidal mechanical disturbance through the electrical network.

Reference [68] reports the design of a robust $\mathcal{H}_\infty$ controller for damping subsynchronous oscillations. The studied system consists of two sets of nonidentical turbine-generators connected to an infinite bus through a partly fixed, partly thyristor-controlled series compensated line. This is actually an extension of the IEEE Second Benchmark Model, system-2. A reduced-order continuous model of the system is used for the design, however the modelling details of TCSC are not discussed.

The work presented here is the usage of the sampled-data model of the whole system, obtained by linearization of the Poincaré map, for the design of an SSR stabilizing controller for TCSC [69].

6.4 Conclusion

An SSR damping controller is designed for the thyristor controlled series capacitor based on a discrete state space model derived from Poincaré mapping techniques. The IEEE First SSR Benchmark model with fixed capacitor-TCSC compensation is used as the case study. The discretization is done with a sampling frequency six times the synchronous frequency. It is shown that the controller can successfully stabilize the otherwise unstable 15.79 Hz mode.

Although the model is derived and verified for a special case, the method is general and can be applied to other configurations as well. Since the model is a state space linearization of the whole system, the dimension of the model grows rapidly with the number of machines included in the study. However, for the application of the controller design techniques, usually the most relevant elements in the system are modeled in detail, with the remaining elements replaced by simple models.

Chapter 7

General Steady State of Thyristor Controlled Series Capacitor

This chapter elaborates on the steady-state theory of thyristor controlled series capacitors. This steady state has always been calculated with the pulses equally distanced. This is not a necessity, however, for a TCSC to obtain steady state.

Here, a more general situation is recognized, and the relations capable of describing it are presented. The dynamical behaviour of TCSC with regard to subsynchronous oscillations is studied under the general steady state using the electromagnetic transients simulation.

7.1 Deviated Firing

A fundamental characteristic of TCSC in deriving its steady-state relations, is that the current of the thyristor-controlled branch is mainly confined to the LC loop and does not contaminate the line current with harmonics. Therefore, the assumption of a purely sinusoidal line current can be made. The assumption remains valid if the pulses for the positive and negative half cycles are not equidistant, but sent alternately φ degrees sooner and φ degrees later than the symmetrical case, here referred to as the *base case*.

To illustrate the idea, Fig.7.1 shows the line current, the capacitor voltage and the thyristor current pulses in one period of a single phase TCSC circuit. The base case current pulses

are also shown as dashed lines for comparison.

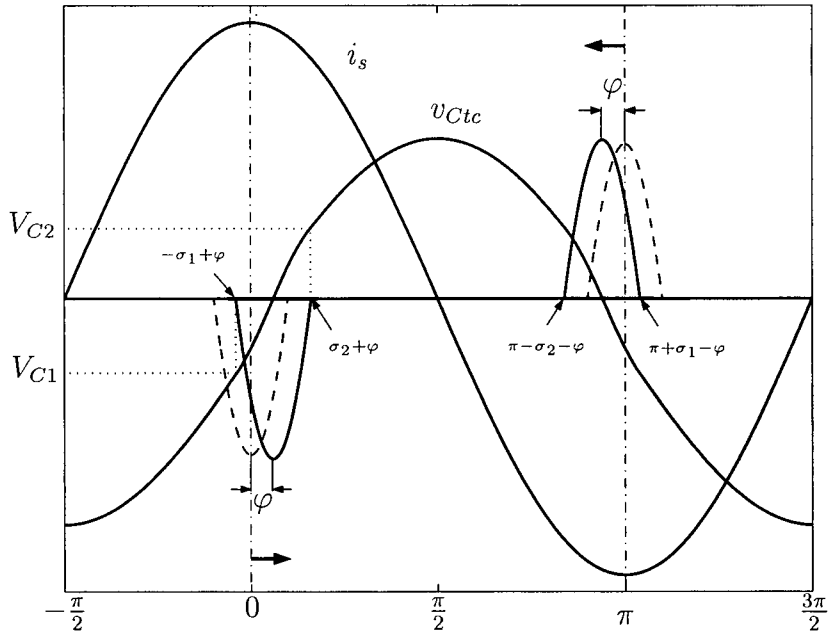

Figure 7.1: Symmetrical vs. deviated firing

When the pulse is shifted by the *deviation angle* φ from the base pulse, it is no longer symmetrical with respect to the axis passing through its maximum point. Therefore, σ_1 and σ_2 are used to indicate the pulse widths to its right and left of the maximum point. The situation is depicted in Fig. 7.2 with a bit of exaggeration. Note that the conduction angle is $\sigma = \sigma_1 + \sigma_2$.

It should be emphasized that because the switches used to implement TCSC are thyristors, the only controllability is over their turn-on times. So, splitting the conduction angle σ into σ_1 and σ_2, does not mean we have control over the turn-off times of the switches. The additional parameter is obtained by a firing policy which assigns two different firing angles to every two consecutive pulses. It is shown that the same compensation level at synchronous frequency can be achieved by different sets of conduction and deviation angles.

In the following, the analytical relations, with deviation angle taken into account, are presented. Next, the numerical procedure for using these relations is outlined, and the characteristic curves of the general and base case are compared. A discussion of the dynamical implications of introducing a new variable φ in the firing of thyristors is next presented,

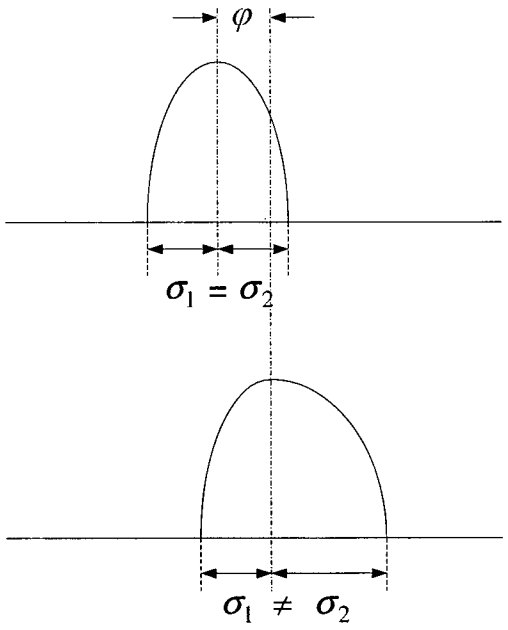

Figure 7.2: Symmetrical and unsymmetrical pulses

based on transient simulation.

7.2 Analytical Relations

Fig. 7.3 shows two consecutive unsymmetrical pulses in an exaggerated manner. It is assumed that the circuit has reached steady state. The line current, which is the same as in Fig. 7.1, is not shown for clarity. With the chosen time origin, $i_s(t) = \sqrt{2} I_s \cos \omega_s t$.

Suppose at the turn-on instant of the inductive branch to conduct the negative pulse, that is at $\omega_s t = -\sigma_1 + \varphi$, the capacitor voltage is V_{C1}. The current continues to flow until $\omega_s t = \sigma_2 + \varphi$, when the thyristor turns off. At this instant the capacitor voltage is denoted by V_{C2}. Note that unlike for the symmetrical case, $V_{C1} \neq -V_{C2}$. The voltage at the turn-on instant of a positive pulse is equal to the voltage at the turn-off instant of a negative pulse and vice versa.

In order to determine V_{C1} and V_{C2}, we need to solve the differential equation

$$\frac{d^2 v_{Ctc}}{dt^2} + \frac{1}{L_{tc} C_{tc}} v_{Ctc} = -\sqrt{2} I_s \frac{\omega_s}{C_{tc}} \sin \omega_s t \tag{7.1}$$

once for a negative pulse and once for a positive pulse. Using $X_{Ctc} = 1/\omega_s C_{tc}$, $X_{Ltc} = \omega_s L_{tc}$,

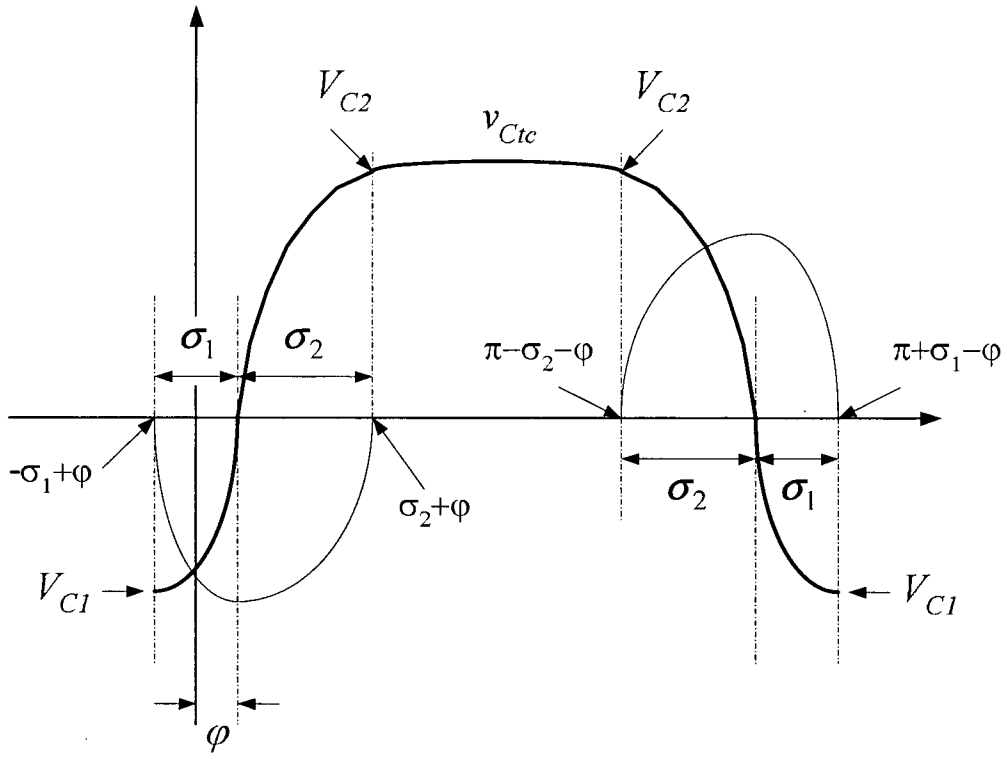

Figure 7.3: Calculating the steady state with unsymmetrical pulses

and $\kappa = \sqrt{X_{Ctc}/X_{Ltc}}$, equation (7.1) is written

$$\frac{d^2 v_{Ctc}}{d(\omega_s t)^2} + \kappa^2 v_{Ctc} = -\sqrt{2} I_s X_{Ctc} \sin \omega_s t \tag{7.2}$$

The initial conditions for the negative pulse are

$$v_{Ctc}(-\sigma_1 + \varphi) = V_{C1} \tag{7.3a}$$

$$\left.\frac{dv_{Ctc}}{d(\omega_s t)}\right|_{-\sigma_1+\varphi} = X_{Ctc} i_s(-\sigma_1 + \varphi) \tag{7.3b}$$

whereas for the positive pulse we have

$$v_{Ctc}(\pi - \sigma_2 - \varphi) = V_{C2} \tag{7.4a}$$

$$\left.\frac{dv_{Ctc}}{d(\omega_s t)}\right|_{\pi-\sigma_2-\varphi} = X_{Ctc} i_s(\pi - \sigma_2 - \varphi) \tag{7.4b}$$

The argument of the variables in (7.3) and (7.4) is expressed in terms of angle instead of time for convenience.

After solving the differential equations, the voltage at the final time $\omega_s t = \sigma_2 + \varphi$ of the negative pulse is set to V_{C2}, and that for the positive pulse to V_{C1}. Thus two algebraic equations are obtained whose simultaneous solution yields the unknowns V_{C1} and V_{C2}. In the following the final calculation results are presented.

V_{C1} and V_{C2} are given by

$$V_{C1} = \frac{\sqrt{2} I_s X_{Ctc}}{\kappa^2 - 1} \left[+ \kappa \cos(-\sigma_1 + \varphi) \frac{\cos \kappa(\sigma_1 + \sigma_2)}{\sin \kappa(\sigma_1 + \sigma_2)} - \kappa \frac{\cos(\sigma_2 + \varphi)}{\sin \kappa(\sigma_1 + \sigma_2)} - \sin(-\sigma_1 + \varphi) \right] \tag{7.5}$$

$$V_{C2} = \frac{\sqrt{2} I_s X_{Ctc}}{\kappa^2 - 1} \left[- \kappa \cos(\sigma_2 + \varphi) \frac{\cos \kappa(\sigma_1 + \sigma_2)}{\sin \kappa(\sigma_1 + \sigma_2)} + \kappa \frac{\cos(-\sigma_1 + \varphi)}{\sin \kappa(\sigma_1 + \sigma_2)} - \sin(\sigma_2 + \varphi) \right] \tag{7.6}$$

The voltage across the capacitor becomes

$$v_{Ctc}(t) = V_{C1} + \sqrt{2} I_s X_{Ctc} [\sin \omega_s t - \sin(-\sigma_1 + \varphi)] \qquad -\tfrac{\pi}{2} \le \omega_s t \le -\sigma_1 + \varphi \tag{7.7}$$

$$v_{Ctc}(t) = \frac{\sqrt{2} I_s X_{Ctc}}{\kappa^2 - 1} \left[\kappa \frac{\cos(-\sigma_1 + \varphi)}{\sin \kappa(\sigma_1 + \sigma_2)} \cos \kappa(\omega_s t - \varphi - \sigma_2) - \kappa \frac{\cos(\sigma_2 + \varphi)}{\sin \kappa(\sigma_1 + \sigma_2)} \cos \kappa(\omega_s t - \varphi + \sigma_1) - \sin \omega_s t \right]_{-\sigma_1 + \varphi \le \omega_s t \le \sigma_2 + \varphi} \tag{7.8}$$

$$v_{Ctc}(t) = V_{C2} + \sqrt{2} I_s X_{Ctc} [\sin \omega_s t - \sin(\sigma_2 + \varphi)] \qquad \sigma_2 + \varphi \le \omega_s t \le \tfrac{\pi}{2} \tag{7.9}$$

with $v_{Ctc}(t) = v_{Ctc}(\pi/\omega_s - t)$; for $\frac{\pi}{2} \le \omega_s t \le \frac{3\pi}{2}$, and $v_{Ctc}(t + 2\pi/\omega_s) = v_{Ctc}(t)$ elsewhere.

The current through the inductor is

$$i_{Ltc}(t) = \frac{\kappa \sqrt{2} I_s}{\kappa^2 - 1} \left[\frac{\cos(-\sigma_1 + \varphi)}{\sin \kappa(\sigma_1 + \sigma_2)} \sin \kappa(\omega_s t - \varphi - \sigma_2) - \frac{\cos(\sigma_2 + \varphi)}{\sin \kappa(\sigma_1 + \sigma_2)} \sin \kappa(\omega_s t - \varphi + \sigma_1) + \cos \omega_s t \right] \qquad -\sigma_1 + \varphi \le \theta \le \sigma_2 + \varphi \tag{7.10}$$

By setting the derivative of either the positive or the negative current pulse to zero at the maximum point, the relation between σ_1 and σ_2 is obtained as

$$\kappa\cos(-\sigma_1+\varphi)\cos\kappa\sigma_2 - \kappa\cos(\sigma_2+\varphi)\cos\kappa\sigma_1 - \sin\kappa(\sigma_1+\sigma_2)\sin\varphi = 0 \qquad (7.11)$$

Equation (7.11) shows that once φ and σ_1 (or σ_2) are set, then σ_2 (or σ_1) is determined as well and cannot be chosen freely.

The fundamental reactance of TCSC is obtained by calculating the first Fourier coefficient of the capacitor voltage and dividing it by the current magnitude.

$$\begin{aligned} X_{TCSC} = X_{Ctc} - \frac{\kappa^2\sigma}{\pi(\kappa^2-1)}X_{Ctc} + \frac{\kappa^2(\kappa^2+1)X_{Ctc}}{2\pi(\kappa^2-1)^2}\Big[\sin 2(-\sigma_1+\varphi) - \sin 2(\sigma_2+\varphi)\Big] - \\ \frac{2\kappa^3 X_{Ctc}}{\pi(\kappa^2-1)^2\sin\kappa\sigma}\Big[\cos\kappa\sigma\cos^2(-\sigma_1+\varphi) + \\ \cos\kappa\sigma\cos^2(\sigma_2+\varphi) - 2\cos(-\sigma_1+\varphi)\cos(\sigma_2+\varphi)\Big] \end{aligned} \qquad (7.12)$$

In (7.12), $\sigma = \sigma_1 + \sigma_2$. A nonzero φ results in a net DC voltage across the capacitor in each phase with the value

$$\begin{aligned} V_{DC} = \frac{\sqrt{2}I_s X_{Ctc}}{\pi}\big[\cos(\sigma_2+\varphi) - \cos(-\sigma_1+\varphi)\big] + \\ \big(\frac{1}{2} - \frac{\sigma_1-\varphi}{\pi}\big)\big[V_{C1} - \sqrt{2}I_s X_{Ctc}\sin(-\sigma_1+\varphi)\big] + \\ \big(\frac{1}{2} - \frac{\sigma_2+\varphi}{\pi}\big)\big[V_{C2} - \sqrt{2}I_s X_{Ctc}\sin(\sigma_2+\varphi)\big] \end{aligned} \qquad (7.13)$$

Note that if $\varphi = 0$, then $\sigma_1 = \sigma_2 = \sigma/2$ and the above relations simplify to the familiar ones for the symmetric firing given in Chapter 2, and repeated here, with β replaced by $\sigma/2$ for ease of comparison.

$$V_{C1} = -V_{C2} = \frac{\sqrt{2}I_s X_{Ctc}}{\kappa^2-1}\big[\sin\frac{\sigma}{2} - \kappa\cos\frac{\sigma}{2}\tan\frac{\kappa\sigma}{2}\big] \qquad (7.14)$$

$$\begin{aligned} X_{TCSC} = X_{Ctc} - \frac{\kappa^2\sigma}{\pi(\kappa^2-1)}X_{Ctc} - \frac{\kappa^2(\kappa^2+1)X_{Ctc}}{\pi(\kappa^2-1)^2}\sin\sigma \\ + \frac{4\kappa^3 X_{Ctc}}{\pi(\kappa^2-1)^2}\cos^2\frac{\sigma}{2}\tan\frac{\kappa\sigma}{2} \end{aligned} \qquad (7.15)$$

7.3 Computational Issues

The relations for the steady-state behaviour of TCSC become more complicated by introducing the deviation angle φ. Specifically, instead of one conduction angle σ, two angles σ_1 and σ_2 appear in the equations. However, once these two are determined, the problem is as straightforward as the one without φ.

One theoretical limit for φ is obtained by noting that, as the magnitude of φ is increased, a point is reached where every two adjacent pulses (in one phase) exactly touch each other. Since the pulses cannot overlap, we must have $\frac{-\pi}{2} < \varphi < \frac{\pi}{2}$.

Corresponding to a certain deviation angle there is a maximum conduction angle that is achievable. Each curve in Fig. 7.4 is obtained for one deviation angle. For $\varphi > 0$ ($\varphi < 0$), the value of $\sigma_2(\sigma_1)$ is assigned and gradually increased, while the value of $\sigma_1(\sigma_2)$ is numerically calculated using (7.11), until the line of $\sigma_1 + \sigma_2 = 180°$ is hit.

For large deviation angles the calculated value shows a sudden jump, such that $\sigma_1 + \sigma_2$ goes beyond the 180° line. This is the case for $\pm 20°$ and $\pm 30°$ in Fig. 7.4, where the plotting is carried out only up to the discontinuity. In the lower part of the figure, where the curves meet, TCSC is in the capacitive mode and in the upper part, where they diverge, it is in the inductive mode. In the following, two types of problems are discussed.

Given: the conduction angle σ

If the conduction angle $\sigma = \sigma_1 + \sigma_2$ is given, then (7.11) is reduced to

$$\kappa \cos(\sigma_2 - \sigma + \varphi) \cos \kappa\sigma_2 - \kappa \cos(\sigma_2 + \varphi) \cos \kappa(\sigma_2 - \sigma) - \sin \kappa\sigma \sin \varphi = 0 \qquad (7.16)$$

MATLAB®'s *fsolve* routine with the initial guess of $\sigma/2$ rapidly converges to the solution for σ_2. It is easy to verify that if $\{\sigma_1, \sigma_2, \varphi\}$ constitutes a solution, then $\{\sigma_2, \sigma_1, -\varphi\}$ is also a solution. Substitution in (7.12) shows that these two sets give the same compensation level. So the curves of TCSC reactance vs. conduction angle, parameterized by the deviation angle, coincide for $\pm\varphi$. As an example, we plot the reactance curves for the Kayenta [45]

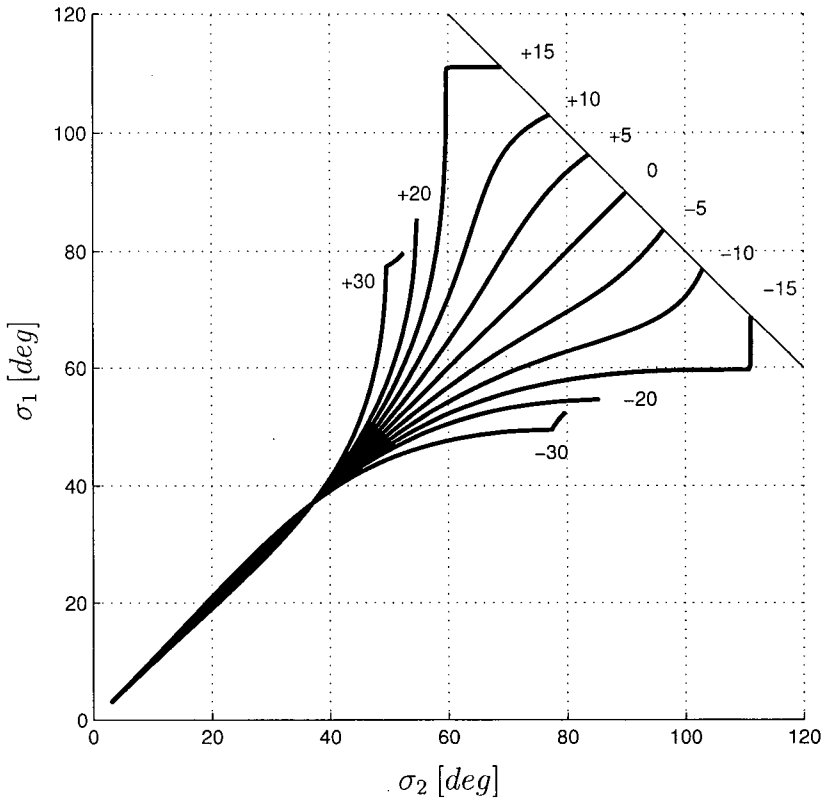

Figure 7.4: σ_1 vs. σ_2 for different deviation angles

TCSC with $C_{tc} = 176.84$ μF and $L_{tc} = 6.74$ mH in Fig. 7.5. The solid line is the curve for $\varphi = \pm 20°$ and the dashed line is that of the base case.

Given: the reactance X_{TCSC}

If a given compensation level, corresponding to a symmetrical firing angle α, is sought, together with a certain deviation angle, then (7.11) and (7.12) must be solved simultaneously to determine σ_1 and σ_2. The initial guess of $\pi - \alpha$ for both angles is good for a rapid convergence.

Table 7.1 lists four possible ways of achieving the same compensation level with the Kayenta TCSC where φ is varied from 0° to 15°.

It is evident from Fig. 7.5 and Table 7.1 that the fundamental reactance of TCSC, especially in the capacitive region, is very insensitive to the changes of the deviation angle.

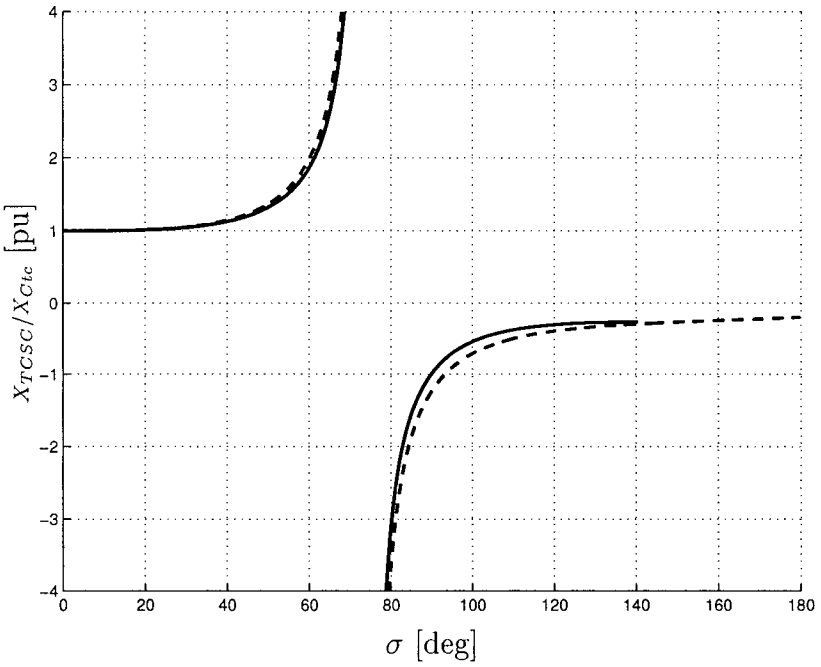

Figure 7.5: Fundamental reactance vs. conduction angle

Table 7.1: Comparison of deviation angles, $X_{TCSC}/X_{Ctc} = 1.65$

σ	σ_1	σ_2	φ
56	28	28	0
56.079	27.949	28.130	5
56.316	27.976	28.340	10
56.713	28.081	28.633	15

7.4 A Dynamical Study

Several studies [11, 37, 70, 71, 72] have shown the advantages of TCSC for the series compensation of transmission lines. In addition to the ability of controlling the power flow in a line, TCSC increases the dynamical stability of the system. It is especially effective in mitigating the subsynchronous resonance.

In the last section it was shown that by changing the deviation angle, TCSC can be set to work in different steady states, while providing the same compensation level. This is an open loop firing control. While it is informative per se to know that TCSC shows such behaviour, it would be even more worthwhile to study the dynamical characteristics with

this type of control, to see if there is any advantage to be gained by it.

In fact, the analysis contained in this chapter was motivated by an observation made while working on the damping controller design for a TCSC tested on the IEEE First Subsynchronous Resonance Benchmark Model [38].

It must be emphasized that the controller in Chapter 6 is a closed-loop controller that works based on equidistant firing. A discrete linear state space model of the system in the rotor reference frame (see Section 5.3) is used to design the controller gains.

When the zero sequence of the TCSC was included in the state variables, although the controller was able to damp the oscillations, the variations of the firing angle around the steady-state value would not decrease beyond a certain value. This is contrary to the common expectation that, as the magnitude of the disturbance decreases, the control action will also decrease.

A closer examination of the firing angle variations revealed that in the steady state the pulses are alternately shifted back and forth in time almost by the same amount. Therefore, the question arose whether this is the reason why the oscillations are damped, or whether this is just a harmless effect arising as a result of the control action.

Let us take a look at the steady-state $0dq$ voltage components of a three-phase TCSC with equidistant firing (Fig. 7.6).

The average of the zero sequence component is 0, however, it oscillates significantly around it. A linear state feedback controller checks for the difference between the instantaneous value of all the states with their steady-state values, and based on the differences, produces a control action (here a deviation in the firing angle). A naive comparison of the zero sequence variable with 0 makes the controller put out an action to bring the difference to zero. Since the zero sequence of TCSC is weakly controllable, a large action is needed to make a small change in it. The zero sequence voltage is also weakly coupled to the other states, so while the controller makes a significant change in its output value, other variables hardly change. Normally all the zero sequence variables are eliminated to arrive at a reduced order system before the design of the controller.

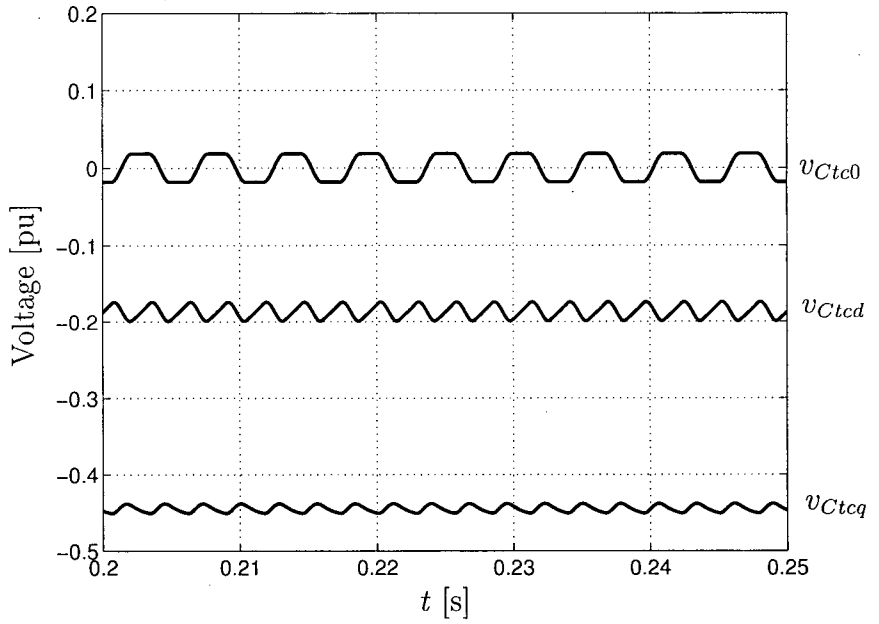

Figure 7.6: $0dq$ waveforms of a TCSC voltage with equidistant firing

Fig. 7.7 shows the $0dq$ voltage components of the same TCSC with deviated firing. The compensation level is the same in both figures. This is evident by noticing that the d and q components have the same average level. The zero sequence component however, is shifted down.

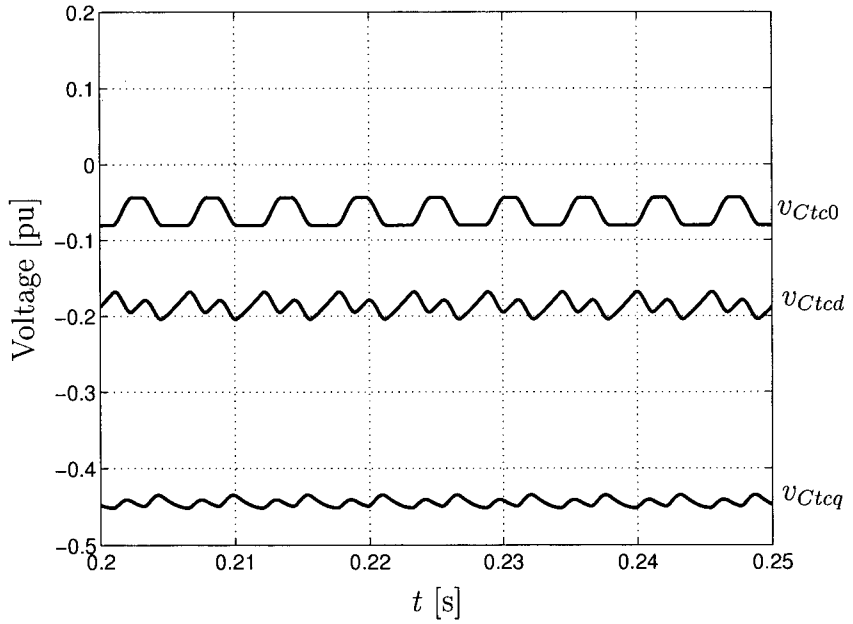

Figure 7.7: $0dq$ waveforms of a TCSC voltage with deviated firing

To complete this section, we compare the mechanical behaviour of the shaft in two cases: once with equidistant firing and the other with deviated firing. Note that these are both open-loop firing strategies. The IEEE First Benchmark Model is used for the study. Fig. 7.8 shows the current waveforms and the torque on the generator-exciter shaft section with 162° equidistant firing. The parameters of the system are given in Appendix B.1. No fault is simulated. The shaft torque is gradually increasing. Fig. 7.9 shows the currents and the same shaft torque when a deviation angle of 15° is used and the compensation level is kept the same. The shaft torque increase is faster in this case. Simulations at other operating points with different deviation angles show that the dynamic characteristics with regards to subsynchronous resonance are either not much different or worse for the deviated firing.

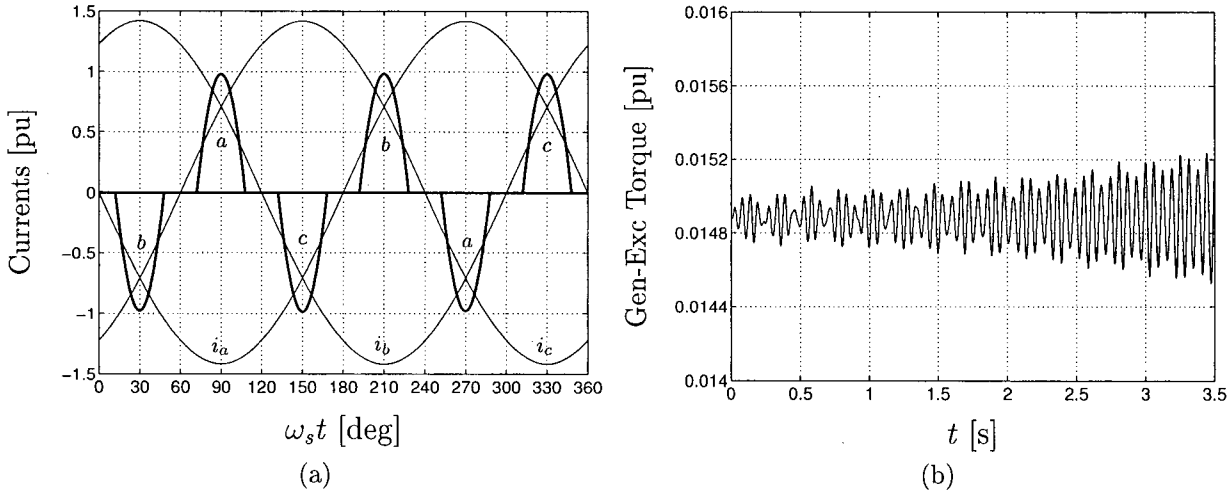

Figure 7.8: Equidistant firing

7.5 Conclusion

A new variable is introduced for the open-loop firing control of the TCSC. There are theoretically infinitely many combinations of σ and φ, which give rise to the same compensation level. However, it was observed that the steady state and the dynamic characteristics of the device are practically indifferent to small deviation angles.

When subsynchronous interaction is present, large deviation angles may cause a shaft torque to increase faster than with equidistant firing. Therefore, we conclude that this type

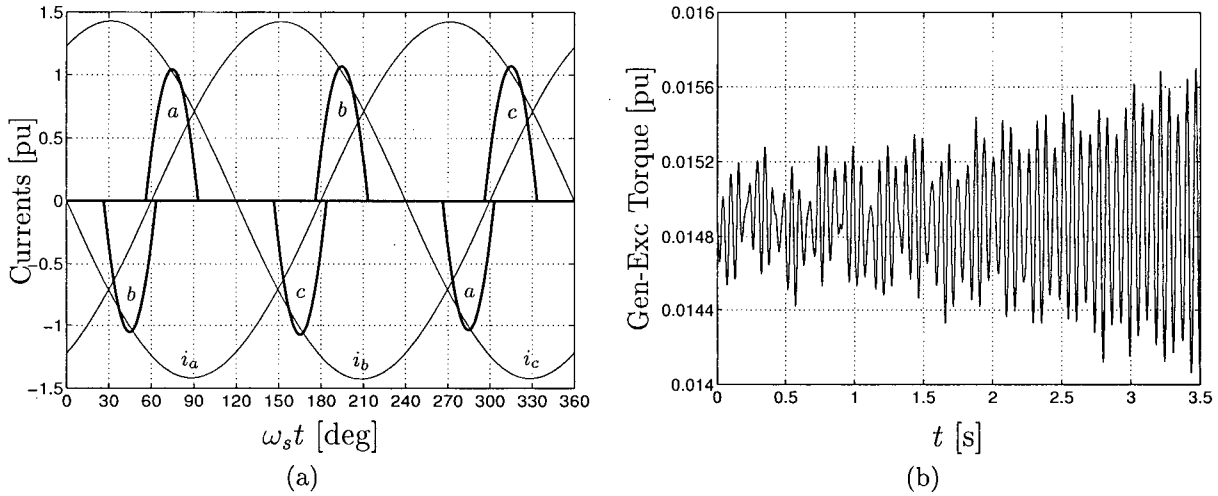

Figure 7.9: Deviated firing, $\varphi = 15°$

of firing is not very useful to address the problem of subsynchronous oscillations. The fact that a DC voltage appears across the TCSC as a result, can limit the level of deviation more than the theoretical values derived here.

Chapter 8

Conclusion and Future Work

The present chapter summarizes the results of the study elaborated in the previous chapters, and makes suggestions to continue the research.

8.1 Conclusion

In this thesis, the problem of mechanical subsynchronous oscillations is studied in the presence of thyristor controlled series capacitors.

The passive damping of TCSC at subsynchronous frequencies is thoroughly investigated. This behaviour has been observed both on network analyzers and in simulations, however the explanation that it happens as a result of energy being absorbed at a subsynchronous frequency and injected into the switching frequency is a contribution of the present work. In order to show this point, the resistance of a TCSC in periodic operation was calculated first by power considerations and next by the discrete Fourier analysis of the waveforms, and found to be the same.

The global view is that in TCSC, because of its nonlinearity, the frequency response at different frequencies are correlated. The phase shift between the voltage and the current at a subsynchronous frequency, is between 0 and 90°. This leads to the conclusion that energy is being dissipated at that frequency. However, in the synchronous frequency another effect

is taking place at the same time. The phase shift between the current and voltage at the synchronous frequency is slightly higher than 90°. This phase shift is much less than the one happening at the subsynchronous frequency, which is the reason why it went unnoticed when the passive damping was initially observed.

TCSC damping and detuning effects help toward mitigating subsynchronous resonance. However, these effects are variable, and dependent on the synchronization scheme and the operating point of the TCSC. Larger conduction angles are more effective in damping subsynchronous oscillations.

The common practice is to use TCSC as part of a total series compensation. The larger the portion of TCSC in the compensation, the more it affects the dynamics of the system.

The system studied in this thesis is the First IEEE SSR Benchmark Model with a fixed capacitor, TCSC compensated line. It was observed that TCSC does not stabilize all the subsynchronous modes in open loop operation. This is consistent with the results reported in [27], and [35]. Therefore, in order to make certain that subsynchronous oscillations get damped properly, closed-loop control of the firing angle of the TCSC is necessary.

Sampled-data models, based on the Poincaré mapping concept, are able to represent the system dynamics well enough for the effective design of feedback controller gains. This is shown by deriving the model for the study system.

Two approximations were applied in deriving the model:

1. The periodic orbit of the system is approximated by the load flow solution. To do the load flow, TCSC is replaced by its fundamental reactance at 60 Hz. After the line current is determined, for the TCSC capacitor voltage and inductor current the ideal steady state waveforms given in Section 2.4 are used. The model was transformed into the rotor $0dq$ reference frame.

2. After the model is obtained the zero-sequence variables are omitted. This includes the zero-sequence component of the line current, the fixed capacitor voltage, and the TCSC voltage.

The eigenanalysis was performed both with and without the zero-sequence variables, and the results were compared with detailed transient simulation. The conclusion was that while both systems identify the unstable subsynchronous modes of oscillation, the system without

the zero-sequence variables is more successful in predicting the dominant unstable mode.

Next, the reduced-order model was used to adjust the gains of a feedback controller that shifts the unstable subsynchronous modes inside the unit circle, thus stabilizing the system. The eigenvalue analysis was confirmed by transient simulation where a three-phase short circuit was used to initiate the interaction between the mechanical and electrical subsystems. The system with the closed-loop firing controller was able to recover after the fault removal, while the open-loop system became unstable.

In the last chapter, a new open-loop firing strategy is introduced where the pulses are alternately shifted back and forth in time by the same amount. The underlying assumption of sinusoidal line current is left untouched. Detailed analytical relations are calculated for the new firing. When firing is done with a non-zero *deviation angle*, a DC voltage appears across TCSC. Transient simulation studies show that large deviation angles aggravate the subsynchronous oscillation problem.

8.2 Suggestions for Future Work

As long as the magnitudes of the disturbances are small, it is reasonable to analyze the passive damping at each subsynchronus frequency separately. However, one has to keep in mind that TCSC is highly nonlinear. The study of the resistive behaviour of TCSC can be extended by applying more than one subsynchronous current at the same time to see if the phase shifts in the subsynchronous currents are correlated in some way.

Since the model developed in Chapter 5 is able to characterize the behaviour of the system, more advanced control techniques such as robust control, can be investigated to improve the controller performance.

The observer, designed for the turbo-generator, needs samples from the generator rotor angle and speed deviations. This poses a limitation on the installation location of the TCSC to be near the generator site. In order to possibly eliminate this limitation, an investigation is needed to see if the system can be modelled in such a way that the feedback signal does not rely on the generator variables.

As the next step, a system in which subsynchronous interactions happen between two or more machines can be linearized and studied for the damping of oscillations with the method of this thesis. A systematic order reduction is necessary to reduce the dimension of the linear model beyond what is obtainable by omitting the zero-sequence variables.

Bibliography

[1] N. Hingorani, "Flexible AC transmission," *IEEE Spectrum*, pp. 40–45, Apr. 1993.

[2] T. Miller, *Reactive Power Control in Electric Systems*, 1st ed. John Wiley, 1982.

[3] IEEE Committee Report, "Reader's guide to subsynchronous resonance," *IEEE Trans. Power Syst.*, vol. 7, no. 1, pp. 150–157, Feb. 1992.

[4] K. Padiyar, *Analysis of Subsynchronous Resonance in Power Systems*, 1st ed. Kluwer Academic Publishers, 1999.

[5] J. Butler and C. Concordia, "Series capacitor application problems," *AIEE Transactions*, vol. 56, pp. 975–988, Aug. 1937.

[6] C. Concordia and G. Carter, "Negative damping of electrical machinary," *AIEE Transactions*, vol. 60, pp. 116–119, Mar. 1941.

[7] H. Rustebakke and C. Concordia, "Self-excited oscillations in a transmission system using series capacitors," *IEEE Trans. Power App. Syst.*, vol. 89, no. 7, pp. 1504–1512, Sept./Oct. 1970.

[8] C. Bowler, D. Ewart, and C. Concordia, "Self excited torsional frequency oscillations with series capacitors," *IEEE Trans. Power App. Syst.*, vol. 92, no. 5, pp. 1688–1695, Sept./Oct. 1973.

[9] P. Anderson and R. Farmer, *Series Compensation of Power Systems*, 1st ed. California: PBLSH!, 1996.

[10] H. Mulheim/Ruhr and T. Kulig, "Influence of measured damping at torsional vibrations of large turbo-generators," *VDI-Reports*, no. 320, pp. 77–85, 1978.

[11] R. Piwko, C. Wegner, S. Kiney, and J. Eden, "Subsynchronous resonance performance tests of the slatt thyristor-controlled series capacitor," *IEEE Trans. Power Delivery*, vol. 11, no. 2, pp. 1112–1119, Apr. 1996.

[12] M. I. Alimansky, "The application and performance of series capacitors," *General Electric Review*, vol. 33, pp. 616–625, Nov. 1930.

[13] IEEE Committee Report, "A bibliography for the study of subsynchronous resonance between rotating machines and power systems," *IEEE Trans. Power App. Syst.*, vol. 95, no. 1, pp. 216–218, Jan./Feb. 1976.

[14] ——, "First supplement to a bibliography for the study of subsynchronous resonance between rotating machines and power systems," *IEEE Trans. Power App. Syst.*, vol. 98, no. 6, pp. 1872–1875, Nov./Dec. 1979.

[15] ——, "Second supplement to a bibliography for the study of subsynchronous resonance between rotating machines and power systems," *IEEE Trans. Power App. Syst.*, vol. 104, no. 2, pp. 321–327, Feb. 1985.

[16] ——, "Third supplement to a bibliography for the study of subsynchronous resonance between rotating machines and power systems," *IEEE Trans. Power Syst.*, vol. 6, no. 2, pp. 830–834, May 1991.

[17] ——, "Forth supplement to a bibliography for the study of subsynchronous resonance between rotating machines and power systems," *IEEE Trans. Power Syst.*, vol. 12, no. 3, pp. 1276–1282, Aug. 1997.

[18] P. Anderson, B. Agrawal, and J. V. Ness, *Subsynchronous Resonance in Power Systems*, 1st ed. New York: IEEE Press, 1990.

[19] M. B. Hughes, R. W. Leonard, and T. G. Martinich, "Measurement of power system subsynchronous driving point impedance and comparison with computer simulations," *IEEE Trans. Power App. Syst.*, vol. 103, pp. 619–630, 1984.

[20] C. Chen, *Linear System Theory and Design*, 2nd ed. HRW, 1984.

[21] R. Rajaraman, "Damping of subsynchronous resonance and nonlinear dynamics in thyristor switching circuits," Ph.D. dissertation, University of Wisconsin-Madison, May 1996.

[22] S. G. Helbing and G. Karady, "Investigations of an advanced form of series compensation," *IEEE Trans. Power Delivery*, vol. 9, no. 2, pp. 939–947, Apr. 1994.

[23] W. Shouyuan, Z. Xiaoxin, and L. Yajian, "Design and simulation on tcsc analog model and controller," *Proceedings. POWERCON '98',International Conference on Power System Technology*, vol. 1, pp. 430–435, 1998.

[24] E. Larson, K. Clark, J. S.A. Miske, and J. Urbanek, "Characteristics and rating considerations of thyristor controlled series compensation," *IEEE Trans. Power Delivery*, vol. 9, no. 2, pp. 992–1000, Apr. 1994.

[25] R. Hedin, S. Weiss, D. Torgerson, and L. Eilts, "SSR characteristics of alternative types of series compensation schemes," *IEEE Trans. Power Syst.*, vol. 10, no. 2, pp. 845–852, May 1995.

[26] R. A. Hedin, V. Henn, A. H. Montoya, D. R. Torgerson, and S. Weiss, "Advanced series compensation ASC: Transient network analyzer studies compared with digital simulation studies," in *EPRI TR-101784, Proceedins: FACTS Conference 2*, Dec. 1992.

[27] B. Perkins and M. Iravani, "Dynamic modeling of a TCSC with application to SSR analysis," *IEEE Trans. Power Syst.*, vol. 12, no. 4, pp. 1619–1625, Nov. 1997.

[28] K. Stahlkopf and M. Wilhelm, "Tighter control for busier systems," *IEEE Spectrum*, pp. 48–52, Apr. 1997.

[29] N. G. Hingorani and K. Stahlkopf, "High-power electronics," *Scientific American*, pp. 78–85, Nov. 1993.

[30] A. A. Edris, A. S. B. Mehraban, M. Rahman, L. Gyugyi, S. Arabi, and T. R. Rietman, "Controlling the flow of real and reactive power," *IEEE Computer Applications in Power*, pp. 20–25, Jan. 1998.

[31] IEEE Committee Report, "Proposed terms and definitions for flexible AC transmission system(FACTS)," *IEEE Trans. Power Delivery*, vol. 12, no. 4, pp. 1848–1853, Oct. 1997.

[32] H. Othman and L. Angquist, "Analytical modeling of thyristor controlled series capacitors for SSR studies," *IEEE Trans. Power Syst.*, vol. 11, no. 1, pp. 119–127, Feb. 1996.

[33] P. Mattavelli, A. Stankovic, and G. Verghese, "SSR analysis with dynamic phasor model of thyristor controlled series capacitor," *IEEE Trans. Power Syst.*, vol. 14, no. 1, pp. 200–208, Feb. 1999.

[34] A. Ghosh, S. Kumar, and S. Sachchidanand, "Subsynchronous resonance analysis using a discrete time model of thyristor controlled series compensator," *Electrical Power and Energy Systems*, no. 21, pp. 571–578, 1999.

[35] R. Rajaraman, I. Dobson, R. Lasseter, and Y. Shern, "Computing the damping of subsynchronous oscillations due to a thyristor controlled series capacitor," *IEEE Trans. Power Delivery*, vol. 11, no. 2, pp. 1120–1127, July 1996.

[36] R. Rajaraman and I. Dobson, "Damping estimates of subsynchronous and power swing oscillations in power systems with thyristor switching devices," *IEEE Trans. Power Syst.*, vol. 11, no. 4, pp. 1926–1930, Nov. 1996.

[37] W. Zhu, R. Spee, R. Mohler, G. Alexander, W. Mittelstadt, and D. Maratukulam, "An EMTP study of ssr mitigation using the thyristor controlled series capacitor," *IEEE Trans. Power Delivery*, vol. 10, no. 3, pp. 1479–1485, July 1995.

[38] IEEE Committee Report, "First benchmark model for computer simulation of subsynchronous resonance," *IEEE Trans. Power App. Syst.*, vol. 96, no. 5, pp. 1565–1572, Sept./Oct. 1977.

[39] ——, "Second benchmark model for computer simulation of subsynchronous resonance," *IEEE Trans. Power App. Syst.*, vol. 104, no. 5, pp. 1057–1066, May 1985.

[40] P. Mattavelli, G. Verghese, and A. Stankovic, "A thyristor controlled series compensation model for power system stability analysis," *IEEE Trans. Power Syst.*, vol. 12, no. 3, pp. 1259–1267, Aug. 1997.

[41] S. Jalali, R. Hedin, M. Pereira, and K. Sadek, "A stability model for the advanced series compensator(ASC)," *IEEE Trans. Power Delivery*, vol. 11, no. 2, pp. 1128–1137, Apr. 1996.

[42] Z. Xueqiang and C. Chen, "Circuit analysis of a thyristor controlled series compensation," in *IEEE Power Engineering Society Winter Meeting*, 1999, pp. 1067–1072.

[43] J. Paserba, N. Miller, E. Larson, and R. Piwko, "A thyristor controlled series compensation model for power system stability analysis," *IEEE Trans. Power Delivery*, vol. 10, no. 3, pp. 1471–1478, July 1995.

[44] B. Perkins and M. Iravani, "Dynamic modeling of high power static switching circuits in the dq-frame," *IEEE Trans. Power Syst.*, vol. 14, no. 2, pp. 678–684, May 1999.

[45] S. Jalali, R. Lasseter, and I. Dobson, "Dynamic response of a thyristor controlled switched capacitor," *IEEE Trans. Power Delivery*, vol. 9, no. 3, pp. 1609–1615, July 1994.

[46] J. Hauer, W. Mittelstadt, and R. Piwko, "Modulation and SSR tests performed on the bpa 500 kv thyristor controlled series capacitor unit at slatt substation," *IEEE Trans. Power Syst.*, vol. 11, no. 2, pp. 801–806, May 1996.

[47] J. Urbanek, R. Piwko, E. Larson, B. Damsky, B. Furumasu, and W. Mittlestadt, "Thyristor controlled series compensation prototype installation at the slatt 500 kv substation," *IEEE Trans. Power Delivery*, vol. 8, no. 3, pp. 1460–1469, July 1993.

[48] M. Noroozian and G. Andersson, "Power flow control by use of controllable series components," *IEEE Trans. Power Delivery*, vol. 8, no. 3, pp. 1420–1429, July 1993.

[49] E. A. Leonidaki, N. D. Hatziargyriou, B. C. Papadias, and G. J. Georgantzis, "Investigation of power system harmonics and SSR phenomena related to thyristor controlled

series capacitors," in *Proc. IEEE/PES* 8^{th} *International Conference on Harmonics and Quality of Power (ICHQP'98)*, Athens, Greece, Oct. 1998, pp. 848–852.

[50] J. Guckenheimer and P. Holmes, *Nonlinear Oscillations, Dynamical Systems, and Bifurcations of Vector Fields*, 2nd ed. New York: Springer-Verlag, 1983.

[51] I. Dobson, "Stability of ideal thyristor and diode switching circuits," *IEEE Trans. Circuits Syst. I*, vol. 42, pp. 517–529, Sept. 1995.

[52] T. Chen and B. Francis, *Optimal Sampled-data Control Systems*, 2nd ed. London: Springer-Verlag, 1996.

[53] J. Dorsey, *Continuous and Discrete Control Systems.* McGraw-Hill, 2002.

[54] Y. Bar-Shalom and T. E. Fortmann, *Tracking and Data Association.* San Diego, California: Academic Press, Inc., 1988.

[55] K. Ogata, *Discrete-time Control Systems*, 1st ed. NJ: Prentice-Hall, Inc, 1987.

[56] The MathWorks, Inc. (2002) *MATLAB* version 6.5.0. [Online]. Available: http://www.mathworks.com/

[57] H. Dommel, *EMTP Theory Book*, 2nd ed. Vancouver, British Columbia: MicroTran Power System Analysis Corporation, 1996.

[58] J. B. Marion and S. T. Thornton, *Classical Dynamics of Particles & Systems*, 3rd ed. Harcourt Brace Jovanovich, 1988.

[59] P. C. Krause, O. Wasynczuk, and S. D. Sudhoff, *Analysis of Electric Machinery.* IEEE Press, 1995.

[60] P. Anderson and A. Fouad, *Power System Control and Stability*, 1st ed. The Iowa State University Press, 1977.

[61] K. Kabiri, H. W. Dommel, and S. Henschel, "A simplified system for subsynchronous resonance studies," in *Proc. International Conference on Power System Transients (IPST'2001)*, vol. 1, Rio de Janeiro, Brazil, June 2001, pp. 234–239.

[62] A. Daneshpooy and A. M. Gole, "Frequency response of the thyristor controlled series capacitor," *IEEE Trans. Power Delivery*, vol. 16, pp. 53–58, Jan. 2001.

[63] S. Skogestad and I. Postlethwaite, *Multivariable Feedback Control*, 1st ed. West Sussex, England: John Wiley & Sons Ltd, 1996.

[64] K. Kabiri, S. Henschel, and H. W. Dommel, "Resistive behavior of thyristor controlled series capacitors at subsynchronous frequencies," *IEEE Trans. Power Delivery*, vol. 19, pp. 374–379, Jan. 2004.

[65] P. Kundur, *Power System Stability and Control*, 1st ed. McGraw-Hill, Inc., 1994.

[66] A. Ghosh and G. Ledwich, "Modelling and control of thyristor-controlled series compensators," *IEE Proc.-Gener. Transm. Distrib.*, vol. 142, no. 3, pp. 297–304, May 1995.

[67] N. Kakimoto and A. Phongphanphanee, "Subsynchronous resonance damping control of thyristor-controlled series capacitor," *IEEE Trans. Power Delivery*, vol. 18, pp. 1051–1059, July 2003.

[68] L. Wang and C. W. Huang, "Suppression of subsynchronous resonance using robust H^{∞} TCSC damping controllers," in *IEEE Power Engineering Society Winter Meeting*, 1999, pp. 610–615.

[69] K. Kabiri, S. Henschel, J. R. Martí, and H. W. Dommel, "A discrete state space model for SSR stabilizing controller design for TCSC compensated systems," *IEEE Trans. Power Delivery*, accepted for publication.

[70] S. Nyati, C. A. Wegner, R. W. Delmerico, R. J. Piwko, D. H. Baker, and A. Edris, "Effectiveness of thyristor controlled series capacitor in enhancing power system dynamics: an analog simulator study," *IEEE Trans. Power Delivery*, vol. 9, pp. 1018–1026, 1994.

[71] T. S. Luor, Y. Y. Hsu, T. Y. Guo, J. T. Lin, and C. Y. Huang, "Application of thyristor-controlled series compensators to enhance oscillatory stability and transmission capability of a longitudinal power system," *IEEE Trans. Power Syst.*, vol. 14, pp. 179–185, Feb. 1999.

[72] D. J. Trudnowski, M. K. Donnelly, and J. F. Hauler, "Estimating damping effectiveness of BPA's thyristor controlled series capacitor by applying time and frequency domain methods to measured response," *IEEE Trans. Power Syst.*, vol. 11, no. 2, pp. 761–766, Apr. 1996.

Appendix A

Linear Discrete Model of Single-Phase TCSC

Here, the linear Poincaré map is derived for a single-phase TCSC by assuming the line current to be the forcing function. Consider the steady-state waveforms of a TCSC in Fig. A.1.

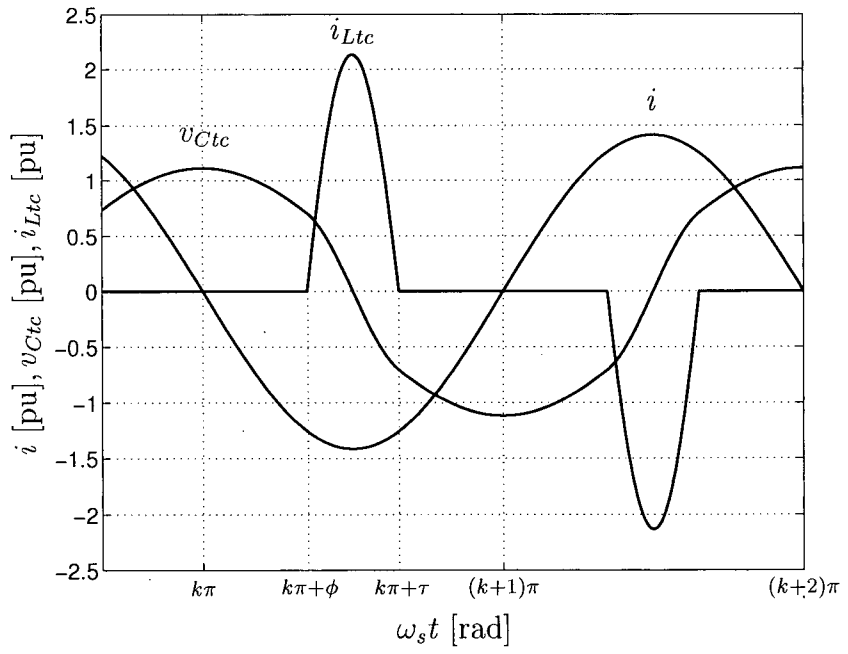

Figure A.1: Calculating the Poincaré map for a single-phase TCSC

The time origin has been selected such that $k\pi$ is a point where the capacitor voltage

becomes maximum. In the following discussion, the argument of the waveforms is sometimes expressed in terms of the angle instead of time for ease of reference. So an angle of $k\pi$ rad corresponds to a time of $k\pi/\omega_s$ s, with ω_s being the synchronous speed.

The map we are seeking to find, advances $v_{Ctc}(k\pi)$ to half a period later $v_{Ctc}(k\pi+\pi)$. The waveforms repeat with a period of 2π rad. However, because of the half-wave symmetry, we need only consider the changes up to π rad.

When either thyristor conducts, the circuit has the dynamics [27]

$$\dot{\mathbf{x}} = \frac{d\mathbf{x}}{dt} = \mathbf{A}\mathbf{x}(t) + \mathbf{b}i(t) \quad \mathbf{A} = \begin{bmatrix} 0 & -\frac{1}{C_{tc}} \\ \frac{1}{L_{tc}} & 0 \end{bmatrix} \quad \mathbf{b} = \begin{bmatrix} \frac{1}{C_{tc}} \\ 0 \end{bmatrix} \tag{A.1}$$

with the state vector $\mathbf{x} = [v_{Ctc} \;\; i_{Ltc}]^t$ and input i. In the non-conduction mode, $i_{Ltc} = \mathbf{c}\mathbf{x} = [1 \;\; 0]\mathbf{x} = 0$, and the dynamic equations are transformed into

$$\dot{v}_{Ctc} = \frac{dv_{Ctc}}{dt} = \mathbf{p_j}\mathbf{A}\mathbf{q_j}v_{Ctc} + \mathbf{P}\mathbf{b}i(t) = 0v_{Ctc} + \frac{1}{C_{tc}}i \tag{A.2}$$

where $\mathbf{p_j} = [1 \;\; 0]$ and $\mathbf{q_j} = \mathbf{p_j}^t$. Following the procedure detailed in [51], the advance map from $v_{Ctc}(k\pi)$ to $v_{Ctc}(k\pi+\pi)$ is found by integrating the system equations in any interval when the switch remains either on or off, and by mapping the changes forward in time using $\mathbf{p_j}$, and $\mathbf{q_j}$.

1. Interval $[k\pi \quad k\pi+\phi]$

   The thyristor is off in this interval, so we have

   $$v_{Ctc}(k\pi+\phi) = v_{Ctc}(k\pi) + \frac{1}{\omega_s C_{tc}} \int_{k\pi}^{k\pi+\phi} i(\eta)d\eta \tag{A.3}$$

   where the integration variable is $\eta = \omega_s t$.

2. Interval $[k\pi+\phi \quad k\pi+\tau]$

   The thyristor is on, so there are two state variables, v_{Ctc} and i_{Ltc}. The solution of the dynamical equation (A.1) yields

   $$\mathbf{x}(k\pi+\tau) = e^{\mathbf{A}(\tau-\phi)}\mathbf{x}(k\pi+\phi) + \frac{1}{\omega_s C_{tc}} \int_{k\pi+\phi}^{k\pi+\tau} e^{\mathbf{A}(k\pi+\tau-\eta)}\mathbf{q_j}i(\eta)d\eta \tag{A.4}$$

We notice that $\tau - \phi = \sigma$, where σ is the conduction angle. Also with the matrix $\mathbf{A}$ given in (A.1) we have

$$e^{\mathbf{A}\sigma} = \begin{bmatrix} \cos\kappa\sigma & -\sqrt{\frac{L_{tc}}{C_{tc}}}\sin\kappa\sigma \\ \sqrt{\frac{C_{tc}}{L_{tc}}}\sin\kappa\sigma & \cos\kappa\sigma \end{bmatrix} \tag{A.5}$$

where $\kappa = \omega_N/\omega_s$ is the ratio of the TCSC natural frequency to the synchronous frequency.

3. Interval $[k\pi + \tau \quad k\pi + \pi]$

In this interval, the thyristors are off and similar to the first interval we have

$$v_{Ctc}(k\pi + \pi) = v_{Ctc}(k\pi + \tau) + \frac{1}{\omega_s C_{tc}} \int_{k\pi+\tau}^{k\pi+\pi} i(\eta)d\eta \tag{A.6}$$

With the maps of all the intervals at hand, we notice that at $k\pi + \tau$

$$v_{Ctc}(k\pi + \tau) = \mathbf{p_j}\mathbf{x}(k\pi + \tau) \tag{A.7}$$

If $v_{Ctc}(k\pi + \tau)$ in (A.6) is substituted according to (A.7), then

$$v_{Ctc}(k\pi + \pi) = \mathbf{p_j}\mathbf{x}(k\pi + \tau) + \frac{1}{\omega_s C_{tc}} \int_{k\pi+\tau}^{k\pi+\pi} i(\eta)d\eta \tag{A.8}$$

Now $\mathbf{x}(k\pi + \tau)$ in (A.8) is substituted according to (A.4)

$$v_{Ctc}(k\pi + \pi) = \mathbf{p_j}e^{\mathbf{A}\sigma}\mathbf{x}(k\pi + \phi) + \frac{1}{\omega_s C_{tc}} \int_{k\pi+\phi}^{k\pi+\tau} \mathbf{p_j}e^{\mathbf{A}(k\pi+\tau-\eta)}\mathbf{q_j}i(\eta)d\eta + \frac{1}{\omega_s C_{tc}} \int_{k\pi+\tau}^{k\pi+\pi} i(\eta)d\eta \tag{A.9}$$

At $k\pi + \phi$ we have

$$\mathbf{x}(k\pi + \phi) = \mathbf{q_j}v_{Ctc}(k\pi + \phi) \tag{A.10}$$

By replacing $\mathbf{x}(k\pi + \phi)$ in (A.9), and using (A.3) to replace $v_{Ctc}(k\pi + \phi)$ in turn, we get

$$v_{Ctc}(k\pi + \pi) = \mathbf{p_j}e^{\mathbf{A}\sigma}\mathbf{q_j}v_{Ctc}(k\pi) + \frac{1}{\omega_s C_{tc}}\mathbf{p_j}e^{\mathbf{A}\sigma}\mathbf{q_j} \int_{k\pi}^{k\pi+\phi} i(\eta)d\eta + \frac{1}{\omega_s C_{tc}} \int_{k\pi+\phi}^{k\pi+\tau} \mathbf{p_j}e^{\mathbf{A}(k\pi+\tau-\eta)}\mathbf{q_j}i(\eta)d\eta + \frac{1}{\omega_s C_{tc}} \int_{k\pi+\tau}^{k\pi+\pi} i(\eta)d\eta \tag{A.11}$$

Using (A.5), the advance map from $k\pi$ to $k\pi+\pi$ looks like

$$v_{Ctc}(k\pi+\pi)=\cos\kappa\sigma v_{Ctc}(k\pi)+\frac{1}{\omega_s C_{tc}}\cos\kappa\sigma\int_{k\pi}^{k\pi+\phi} i(\eta)d\eta+$$
$$\frac{1}{\omega_s C_{tc}}\int_{k\pi+\phi}^{k\pi+\tau}\cos[\kappa(k\pi+\tau-\eta)]i(\eta)d\eta+\frac{1}{\omega_s C_{tc}}\int_{k\pi+\tau}^{k\pi+\pi} i(\eta)d\eta \quad (A.12)$$

The advance map is a function of $v_{Ctc}(k\pi)$, ϕ, τ, and a *functional* of $i(t)$, that is, it depends on all the values of the function $i(t)$; $\omega_s t\in[k\pi \;\; k\pi+\pi]$. This is shown as follows

$$v_{Ctc}(k\pi+\pi)=f(v_{Ctc}(k\pi),\phi,\tau,i(\cdot)) \quad (A.13)$$

The linearized discrete model of the TCSC is obtained by calculating the linear variation of (A.13) around a steady-state periodic orbit based at $(v^*_{Ctc}(k\pi),\bar{\phi},\bar{\tau},i^*(\cdot))$, where overbar denotes a steady-state value and asterisk denotes a steady-state waveform. If we denote the small signal change by 'Δ', then

$$\Delta v_{Ctc}(k\pi+\pi)=\left.\frac{\partial f}{\partial v_{Ctc}(k\pi)}\right|_*\Delta v_{Ctc}(k\pi)+\left.\frac{\partial f}{\partial\phi}\right|_*\Delta\phi+\left.\frac{\partial f}{\partial\tau}\right|_*\Delta\tau+ \quad (A.14)$$
$$\Delta f(v^*_{Ctc}(k\pi),\bar{\phi},\bar{\tau},\Delta i(\cdot))$$

After detailed calculations

$$\Delta v_{Ctc}(k\pi+\pi)=\cos\kappa\bar{\sigma}\Delta v_{Ctc}(k\pi)+(-1)^k\alpha_\phi\Delta\phi+\frac{1}{\omega_s C_{tc}}\cos\kappa\bar{\sigma}\int_{k\pi}^{k\pi+\bar{\phi}}\Delta i(\eta)d\eta+$$
$$\frac{1}{\omega_s C_{tc}}\int_{k\pi+\bar{\phi}}^{k\pi+\bar{\tau}}\cos[\kappa(k\pi+\bar{\tau}-\eta)]\Delta i(\eta)d\eta+\frac{1}{\omega_s C_{tc}}\int_{k\pi+\bar{\tau}}^{k\pi+\pi}\Delta i(\eta)d\eta \quad (A.15)$$

with

$$\alpha_\phi=\frac{\sqrt{2}I_s}{\omega_s C_{tc}}\frac{\kappa}{\kappa^2-1}\sin\kappa\bar{\sigma}(\kappa\cos\frac{\bar{\sigma}}{2}\tan\frac{\kappa\bar{\sigma}}{2}-\sin\frac{\bar{\sigma}}{2}) \quad (A.16)$$

Notice that $\Delta v_{Ctc}(k\pi+\pi)$ is independent of the change in the turn-off angle τ. The same result is reported in [45]. If the disturbance current, $\Delta i(\eta)$ in (A.15), is substituted with

$$\Delta i(\eta)=\Delta i_d\cos\eta-\Delta i_q\sin\eta \quad (A.17)$$

and the integration performed with the assumption that Δi_d and Δi_q remain unchanged (zero-order hold assumption), then the relations given in the appendix of [27] will be reached.

Appendix B

First IEEE Subsynchronous Resonance Benchmark Model

B.1 System Parameters

The generator reactances and resistances in Fig. 3.11, Fig. 3.12, and Fig. 3.13 are listed in Table B.1. These parameters are in per unit, based on the stator quantities [60]

S_B = stator rated rms apparent power per phase = 892.4/3 MVA
V_B = stator rated rms line-to-neutral voltage = $500/\sqrt{3}$ kV
ω_B = generator rated angular speed = $2\pi 60$ rad/s

Table B.1: Generator parameters

L_0	L_d	L_{AD}	L_F	L_D	L_q	L_{AQ}	L_G	L_Q
0.135	1.79	1.66	1.722	1.665	1.71	1.58	1.906	1.675

R_0	R_a	R_F	R_D	R_G	R_Q
100	0	0.53/377	1.54/377	5.3/377	3.1/377

Table B.2 lists the parameters of the turbo-generator shaft system which consists of four turbines, the generator, and the exciter as shown in Fig. 2.4. The high-pressure turbine is assigned number 1, with the other rotors denoted by ascending numbers. The generator rotor is not numbered, but is indicated by G for the spring constants between the generator rotor and its adjacent rotors.

Table B.2: Shaft assembly parameters

H_1	H_2	H_3	H_4	H	H_5
0.092897	0.155589	0.858670	0.884215	0.868495	0.0342165

K_{12}	K_{23}	K_{34}	K_{4G}	K_{G5}
19.303	34.929	52.038	70.858	2.822

md_1	md_2	md_3	md_4	md_5
0.05	0.11	0.028	0.028	0

The inertia constant, H, measured in units of second, is related to the moment of inertia, J, by

$$H \triangleq \frac{1}{2}\frac{J\omega_m^2}{S_{B3}} \tag{B.1}$$

where S_{B3} is the rated three-phase MVA of the system, and ω_m is the mechanical angular speed. The values of inertia constant in Table B.2 are given for $\omega_m = \omega_B$. The spring constants are indicated in pu torque/rad with the base torque defined by $t_{qB} = S_{B3}/\omega_B$. The mechanical dampings are given in terms of no-load modal damping decrements, md, with the unit of 1/s. Note that the numbers assigned to damping decrements refer to the mechanical modes TM1-TM5. The frequencies of these modes for the isolated shaft system are given in Table 3.1 in Chapter 3.

The positive-sequence and zero-sequence reactance and resistance of the line, the transformer, and the infinite bus (see Fig. 2.4) are given in Table B.3.

Table B.3: Line, transformer & infinite bus reactances

X_{Line1}	X_{Line0}	R_{Line1}	R_{Line0}	X_{Tran1}	X_{Tran0}	$X_{\infty 1}$	$X_{\infty 0}$
0.50	1.56	0.02	0.50	0.14	0.14	0.06	0.06

The series compensation parameters used for controller design in Chapter 6 are given in Table B.4. In the eigenvalue analysis of Chapter 5, where the parameters of the series compensation are varied to study the effect on the stability of subsynchronous modes, the parameter values are duly indicated.

In Table B.4 the values of the fixed and thyristor controlled capacitors have been chosen to give a total reactance of 0.371 pu in the blocked mode. The value of the inductance in the thyristor branch is calculated from $L_{tc} = 1/\kappa^2 C_{tc}$. A small resistance is introduced in series

Table B.4: Series compensation parameters

C	C_{tc}	κ	$\bar{\alpha}$	$\Delta\phi_{max}$	R_{tc}
1/0.121	4	3	164°	5°	$3.57 \cdot 10^{-4}$ $=(0.1/Z_B)$

with the inductance to eliminate the transient response when the TCSC is in the bypassed mode.

The generator power output, power factor and terminal voltage are 0.9 pu, 0.9, and 1.0 pu, respectively. The reactance of the fault is $X_{Fault} = 0.04$ pu.

B.2 Summary of State Equations

The modelling of the system follows closely that of [35]. The per-unit system of [60] is used for the differential equations. All variables, including time, are in per unit. The base time is $t_B = 1/\omega_B$ s. The stator equations are referred to the rotor side, using the Park transformation (3.35). Fig. B.1 is a one-line diagram of the external circuit in which the series compensation is partly fixed and partly thyristor-controlled.

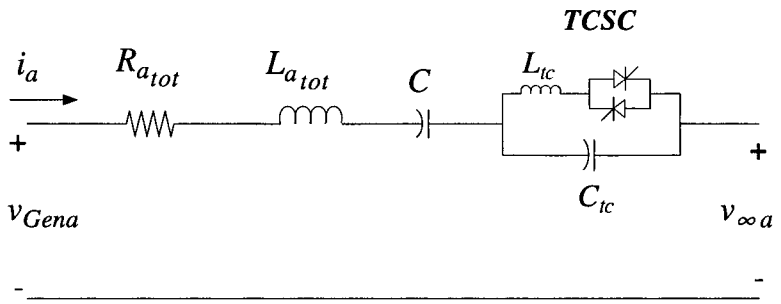

Figure B.1: One-line diagram of the First SSR Benchmark Model with TCSC

$R_{a_{tot}}$ and $L_{a_{tot}}$ are the total series resistance, and the total series inductance of the line, the transformer, and the infinite bus.

The equations of the system with TCSC are obtained by substituting Fig. 3.10 in Section 3.3 with Fig. B.1, writing the equations of the external circuit, and combining them with the generator equations. In the following, the dynamical equations of the system are summarized.

B.2.1 Current Equations

$$\begin{bmatrix} \dot{\mathbf{i}}_{0dq} \\ \dot{\mathbf{i}}_{FDQG} \end{bmatrix} = \hat{\mathbf{L}}^{-1}(\omega\hat{\mathbf{N}} - \hat{\mathbf{R}}) \begin{bmatrix} \mathbf{i}_{0dq} \\ \mathbf{i}_{FDQG} \end{bmatrix} - \hat{\mathbf{L}}^{-1} \begin{bmatrix} \mathbf{v}_{C,0dq} \\ \mathbf{0}_{4\times1} \end{bmatrix} - \hat{\mathbf{L}}^{-1} \begin{bmatrix} \mathbf{v}_{Ctc,0dq} \\ \mathbf{0}_{4\times1} \end{bmatrix} - \hat{\mathbf{L}}^{-1} \begin{bmatrix} \mathbf{v}_{\infty,0dq} \\ -\mathbf{v}_{FDQG} \end{bmatrix} \tag{B.2}$$

where $\mathbf{i}_{0dq} = [i_0\ i_d\ i_q]^t$ is the vector of stator currents, $\mathbf{i}_{FDQG} = [i_F\ i_D\ i_Q\ i_G]^t$ is the vector of rotor currents, $\mathbf{v}_{C,0dq} = [v_{C0}\ v_{Cd}\ v_{Cq}]^t$ is the vector of the fixed capacitor voltages, and $\mathbf{v}_{Ctc,0dq} = [v_{Ctc0}\ v_{Ctcd}\ v_{Ctcq}]^t$ is the vector of the TCSC voltages. The meaning of other parameters is as follows

$$\hat{\mathbf{L}} = \begin{bmatrix} \mathbf{L}_{0dq} + \mathbf{PLQ} & \mathbf{L}_{SR} \\ \mathbf{L}_{SR}^t & \mathbf{L}_R \end{bmatrix} \tag{B.3}$$

$$\hat{\mathbf{N}} = \begin{bmatrix} \mathbf{M}(\mathbf{L}_{0dq} + \mathbf{PLQ}) & \mathbf{M}\mathbf{L}_{SR} \\ \mathbf{0}_{4\times3} & \mathbf{0}_{4\times4} \end{bmatrix} \tag{B.4}$$

$$\hat{\mathbf{R}} = \begin{bmatrix} \mathbf{R}_{0dq} + \mathbf{PRQ} & \mathbf{0}_{3\times4} \\ \mathbf{0}_{4\times3} & \mathbf{R}_{FDQG} \end{bmatrix} \tag{B.5}$$

$$\mathbf{L}_{0dq} = \mathbf{diag}(L_0,\ L_d,\ L_q) \tag{B.6}$$

$$\mathbf{L}_{SR} = \begin{bmatrix} 0 & 0 & 0 & 0 \\ L_{AD} & L_{AD} & 0 & 0 \\ 0 & 0 & L_{AQ} & L_{AQ} \end{bmatrix} \tag{B.7}$$

$$\mathbf{L}_R = \begin{bmatrix} L_F & L_{AD} & 0 & 0 \\ L_{AD} & L_D & 0 & 0 \\ 0 & 0 & L_Q & L_{AQ} \\ 0 & 0 & L_{AQ} & L_G \end{bmatrix} \tag{B.8}$$

$$\mathbf{M} = \begin{bmatrix} 0 & 0 & 0 \\ 0 & 0 & -1 \\ 0 & 1 & 0 \end{bmatrix} \tag{B.9}$$

$$\mathbf{R}_{0dq} = \mathbf{diag}(\, R_0,\ R_a,\ R_a\,) \tag{B.10}$$

$$\mathbf{R}_{FDQG} = \mathbf{diag}(\, R_F,\ R_D,\ R_Q,\ R_G\,) \tag{B.11}$$

$$\mathbf{v}_{\infty,0dq} = \begin{bmatrix} 0 \\ -\sqrt{3}V_\infty \sin(\theta - t - \frac{\pi}{2} - \alpha_\infty) \\ \sqrt{3}V_\infty \cos(\theta - t - \frac{\pi}{2} - \alpha_\infty) \end{bmatrix} \tag{B.12}$$

$$\mathbf{v}_{FDQG} = [\, V_F \ \ 0 \ \ 0 \ \ 0\,]^t \tag{B.13}$$

PLQ and **PRQ** represent the total series reactance and resistance of the line, the transformer and the infinite bus respectively.

$$\begin{aligned} \mathbf{PLQ} &= \mathbf{diag}(\, X_{0_{tot}},\ X_{1_{tot}},\ X_{1_{tot}}\,) \\ &= \mathbf{diag}(\, 1.76,\ 0.7,\ 0.7\,) \end{aligned} \tag{B.14}$$

$$\mathbf{PRQ} = \mathbf{diag}(R_{Line0},\ R_{Line1},\ R_{Line1}) \tag{B.15}$$

B.2.2 Fixed Capacitor Equations

$$\dot{\mathbf{v}}_{C,0dq} = \frac{1}{C}\mathbf{i}_{0dq} + \omega\mathbf{M}\mathbf{v}_{C,0dq} \tag{B.16}$$

B.2.3 TCSC Equations

These equations change with time as the thyristors turn on and off. If all the thyristors are off we have

$$\dot{\mathbf{v}}_{Ctc,0dq} = \frac{1}{C_{tc}}\mathbf{i}_{0dq} + \omega\mathbf{M}\mathbf{v}_{Ctc,0dq} \tag{B.17}$$

With the thyristor in phase a on, the current in the corresponding branch is added to the state variables

$$\dot{\mathbf{v}}_{Ctc,0dq} = \frac{1}{C_{tc}}\mathbf{i}_{0dq} + \omega\mathbf{M}\mathbf{v}_{Ctc,0dq} - \frac{1}{C_{tc}}\mathbf{P}(\theta)\begin{bmatrix}1\\0\\0\end{bmatrix} i_{aLtc} \tag{B.18}$$

$$\dot{i}_{aLtc} = \frac{1}{L_{tc}}[1 \ \ 0 \ \ 0]\mathbf{Q}(\theta)\mathbf{v}_{Ctc,0dq} \tag{B.19}$$

where $\mathbf{P}(\theta)$ and $\mathbf{Q}(\theta)$ are the Park transformation matrices. Any combination of switches can be similarly handled. For example, if the thyristors in phases a and c are on, we have

$$\dot{\mathbf{v}}_{Ctc,0dq} = \frac{1}{C_{tc}}\mathbf{i}_{0dq} + \omega\mathbf{M}\mathbf{v}_{Ctc,0dq} - \frac{1}{C_{tc}}\mathbf{P}(\theta)\begin{bmatrix}1 & 0\\ 0 & 0\\ 0 & 1\end{bmatrix}\begin{bmatrix}i_{aLtc}\\ i_{cLtc}\end{bmatrix} \tag{B.20}$$

$$\begin{bmatrix}\dot{i}_{aLtc}\\ \dot{i}_{cLtc}\end{bmatrix} = \frac{1}{L_{tc}}\begin{bmatrix}1 & 0 & 0\\ 0 & 0 & 1\end{bmatrix}\mathbf{Q}(\theta)\mathbf{v}_{Ctc,0dq} \tag{B.21}$$

B.2.4 Mechanical Equations

If the base quantities for the moment of inertia, the damping, and the spring constant are chosen as

$$J_B = \frac{S_{B3}}{\omega_B^3} \tag{B.22}$$

$$D_B = \frac{S_{B3}}{\omega_B^2} \tag{B.23}$$

$$K_B = \frac{S_{B3}}{\omega_B} = t_{qB} \tag{B.24}$$

then the form of mechanical equations in per unit and in actual units is the same. Note that time is in per unit as well. Usually inertia constant, H, is used instead of moment of inertia, where J in per unit equals $2\omega_B H$. Inertia constant, H, is measured in units of second. The mechanical equations in terms of H are

$$\dot{\boldsymbol{\omega}} = -\frac{1}{2\omega_B}\mathbf{H}^{-1}\mathbf{K}\boldsymbol{\theta} - \frac{1}{2\omega_B}\mathbf{H}^{-1}\mathbf{D}\boldsymbol{\omega} + \frac{1}{2\omega_B}\mathbf{H}^{-1}\mathbf{t_q} \tag{B.25}$$

$$\dot{\boldsymbol{\theta}} = \boldsymbol{\omega} \tag{B.26}$$

with

$$\boldsymbol{\omega} = \begin{bmatrix}\omega_1 & \omega_2 & \omega_3 & \omega_4 & \omega & \omega_5\end{bmatrix}^t \tag{B.27}$$

$$\boldsymbol{\theta} = \begin{bmatrix}\theta_1 & \theta_2 & \theta_3 & \theta_4 & \theta & \theta_5\end{bmatrix}^t \tag{B.28}$$

$$\mathbf{H} = \mathbf{diag}(H_1,\ H_2,\ H_3,\ H_4,\ H,\ H_5) \tag{B.29}$$

$$\mathbf{K} = \begin{bmatrix} K_{12} & -K_{12} & 0 & 0 & 0 & 0 \\ -K_{12} & K_{12}+K_{23} & -K_{23} & 0 & 0 & 0 \\ 0 & -K_{23} & K_{23}+K_{34} & -K_{34} & 0 & 0 \\ 0 & 0 & -K_{34} & K_{34}+K_{45} & -K_{45} & 0 \\ 0 & 0 & 0 & -K_{4G} & K_{4G}+K_{G5} & -K_{G5} \\ 0 & 0 & 0 & 0 & -K_{G5} & K_{G5} \end{bmatrix} \tag{B.30}$$

$$\mathbf{D} = \mathbf{diag}(D_1,\ D_2,\ D_3,\ D_4,\ D,\ D_5) \tag{B.31}$$

The mutual damping between adjacent masses is neglected. The damping coefficients to the reference are calculated from the modal dampings using the approximate method of Section 3.3.1 [18].

$$\mathbf{t_q} = [t_{q1}\ \ t_{q2}\ \ t_{q3}\ \ t_{q4}\ \ -t_{qe}\ \ t_{q5}]^t \tag{B.32}$$

$$t_{qe} = \frac{1}{3}[(L_d i_d + L_{AD} i_D + L_{AD} i_F) i_q - (L_q i_q + L_{AQ} i_Q + L_{AQ} i_G) i_d] \tag{B.33}$$

Appendix C

Derivation of Equation (5.15)

To derive (5.15), the value of $\partial \mathbf{x}/\partial \mathbf{x}_{t_0}$ and $\partial \mathbf{x}/\partial t_0$ given by (5.13) and (5.14)

$$\frac{\partial \mathbf{x}}{\partial \mathbf{x}_{t_0}} = \mathbb{1} + \int_{t_0}^{t} \frac{\partial \mathbf{g}}{\partial \mathbf{x}} \frac{\partial \mathbf{x}}{\partial \mathbf{x}_{t_0}} d\eta \tag{5.13}$$

$$\frac{\partial \mathbf{x}}{\partial t_0} = -\mathbf{g}(\mathbf{x}_{t_0}, t_0) + \int_{t_0}^{t} \frac{\partial \mathbf{g}}{\partial \mathbf{x}} \frac{\partial \mathbf{x}}{\partial t_0} d\eta \tag{5.14}$$

are substituted into their own right-hand side. After one substitution, (5.13) becomes

$$\begin{aligned} \frac{\partial \mathbf{x}}{\partial \mathbf{x}_{t_0}} &= \mathbb{1} + \int_{\eta=t_0}^{t} \frac{\partial \mathbf{g}}{\partial \mathbf{x}} \left(\mathbb{1} + \int_{\xi=t_0}^{\eta} \frac{\partial \mathbf{g}}{\partial \mathbf{x}} \frac{\partial \mathbf{x}}{\partial \mathbf{x}_{t_0}} d\xi \right) d\eta \\ &= \mathbb{1} + \int_{t_0}^{t} \frac{\partial \mathbf{g}}{\partial \mathbf{x}} d\eta + \int_{\eta=t_0}^{t} \frac{\partial \mathbf{g}}{\partial \mathbf{x}} \int_{\xi=t_0}^{\eta} \frac{\partial \mathbf{g}}{\partial \mathbf{x}} \frac{\partial \mathbf{x}}{\partial \mathbf{x}_{t_0}} d\xi d\eta \end{aligned} \tag{C.1}$$

The substitution of (5.13) into (C.1) yields

$$\begin{aligned} \frac{\partial \mathbf{x}}{\partial \mathbf{x}_{t_0}} = \mathbb{1} + \int_{t_0}^{t} \frac{\partial \mathbf{g}}{\partial \mathbf{x}} d\eta + \int_{\eta=t_0}^{t} \frac{\partial \mathbf{g}}{\partial \mathbf{x}} \int_{\xi=t_0}^{\eta} \frac{\partial \mathbf{g}}{\partial \mathbf{x}} d\xi d\eta + \\ \int_{\eta=t_0}^{t} \frac{\partial \mathbf{g}}{\partial \mathbf{x}} \int_{\xi=t_0}^{\eta} \frac{\partial \mathbf{g}}{\partial \mathbf{x}} \frac{\partial \mathbf{x}}{\partial \mathbf{x}_{t_0}} d\xi d\eta \end{aligned} \tag{C.2}$$

The procedure can be continued indefinitely. Let us now examine (5.14). After one

substitution of (5.14) into itself we get

$$\begin{aligned}\frac{\partial \mathbf{x}}{\partial t_0} &= -\mathbf{g}(\mathbf{x}_{t_0}, t_0) + \int_{\eta=t_0}^{t} \frac{\partial \mathbf{g}}{\partial \mathbf{x}} \Big(-\mathbf{g}(\mathbf{x}_{t_0}, t_0) + \int_{\xi=t_0}^{t} \frac{\partial \mathbf{g}}{\partial \mathbf{x}} \frac{\partial \mathbf{x}}{\partial t_0} d\eta \Big) d\eta \\ &= -\mathbf{g}(\mathbf{x}_{t_0}, t_0) - \Big(\int_{t_0}^{t} \frac{\partial \mathbf{g}}{\partial \mathbf{x}} d\eta \Big) \mathbf{g}(\mathbf{x}_{t_0}, t_0) + \int_{\eta=t_0}^{t} \frac{\partial \mathbf{g}}{\partial \mathbf{x}} \int_{\xi=t_0}^{\eta} \frac{\partial \mathbf{g}}{\partial \mathbf{x}} \frac{\partial \mathbf{x}}{\partial t_0} d\xi d\eta \\ &= -\Big(\mathbb{1} + \int_{t_0}^{t} \frac{\partial \mathbf{g}}{\partial \mathbf{x}} d\eta \Big) \mathbf{g}(\mathbf{x}_{t_0}, t_0) + \int_{\eta=t_0}^{t} \frac{\partial \mathbf{g}}{\partial \mathbf{x}} \int_{\xi=t_0}^{\eta} \frac{\partial \mathbf{g}}{\partial \mathbf{x}} \frac{\partial \mathbf{x}}{\partial t_0} d\xi d\eta \end{aligned} \tag{C.3}$$

The substitution of (5.14) into (C.3) results in

$$\begin{aligned}\frac{\partial \mathbf{x}}{\partial t_0} = -\Big(\mathbb{1} + \int_{t_0}^{t} \frac{\partial \mathbf{g}}{\partial \mathbf{x}} d\eta + \int_{\eta=t_0}^{t} \frac{\partial \mathbf{g}}{\partial \mathbf{x}} \int_{\xi=t_0}^{\eta} \frac{\partial \mathbf{g}}{\partial \mathbf{x}} d\xi d\eta \Big) \mathbf{g}(\mathbf{x}_{t_0}, t_0) + \\ \int_{\eta=t_0}^{t} \frac{\partial \mathbf{g}}{\partial \mathbf{x}} \int_{\xi=t_0}^{\eta} \frac{\partial \mathbf{g}}{\partial \mathbf{x}} \frac{\partial \mathbf{x}}{\partial t_0} d\xi d\eta \end{aligned} \tag{C.4}$$

Comparing (C.2) and (C.4) already shows the similarity between the relations as they evolve. By continuing the substitution more and more similar terms are branched off the last integrals on the right-hand side, and added to the series. Assuming that

$$\int_{\eta=t_0}^{t} \frac{\partial \mathbf{g}}{\partial \mathbf{x}} \int_{\xi=t_0}^{\eta} \frac{\partial \mathbf{g}}{\partial \mathbf{x}} \int_{\xi=t_0}^{\rho} \frac{\partial \mathbf{g}}{\partial \mathbf{x}} \cdots d\rho d\xi d\eta \tag{C.5}$$

tends to zero (which is a sufficient condition for the series to converge), the last integrals become zero in the limit, and we get

$$\frac{\partial \mathbf{x}}{\partial t_0} = -\frac{\partial \mathbf{x}}{\partial \mathbf{x}_{t_0}} \mathbf{g}(\mathbf{x}_{t_0}, t_0) \tag{C.6}$$

Appendix D

Participation Matrix

First we review the definition of the left and right eigenvectors [65]. For any eigenvalue λ_i, the column vector $\mathbf{v}_i$ which satisfies

$$\mathbf{A}\mathbf{v}_i = \lambda_i \mathbf{v}_i \tag{D.1}$$

is called the right eigenvector of $\mathbf{A}$ associated with the eigenvalue λ_i.

Similarly, the row vector $\mathbf{w}_i$ which satisfies

$$\mathbf{w}_i\mathbf{A} = \lambda_i \mathbf{w}_i \tag{D.2}$$

is called the left eigenvector associated with the eigenvalue λ_i.

The left and right eigenvectors corresponding to different eigenvalues are orthogonal. In other words, if λ_i is not equal to λ_j,

$$\mathbf{w}_j\mathbf{v}_i = 0 \tag{D.3}$$

On the other hand, for the left and right eigenvectors of the same eigenvalue we have $\mathbf{w}_i\mathbf{v}_i = k_i$, where k_i is a non-zero constant. It is common practice to normalize the vectors so that

$$\mathbf{w}_i\mathbf{v}_i = 1 \tag{D.4}$$

To determine the sensitivity of the eigenvalues to the elements of the state matrix, we differentiate (D.1) with respect to a_{lj} (the element of $\mathbf{A}$ in the lth row and jth column).

$$\frac{\partial \mathbf{A}}{\partial a_{lj}}\mathbf{v}_i + \mathbf{A}\frac{\partial \mathbf{v}_i}{\partial a_{lj}} = \frac{\partial \lambda_i}{\partial a_{lj}}\mathbf{v}_i + \lambda_i \frac{\partial \mathbf{v}_i}{\partial a_{lj}} \tag{D.5}$$

Premultiplying by $\mathbf{w}_i$, and noting that $\mathbf{w}_i\mathbf{v}_i = 1$ and $\mathbf{w}_i(\mathbf{A} - \lambda_i \mathbb{1}) = \mathbf{0}$, the above equation simplifies to

$$\mathbf{w}_i \frac{\partial \mathbf{A}}{\partial a_{lj}}\mathbf{v}_i = \frac{\partial \lambda_i}{\partial a_{lj}} \tag{D.6}$$

All elements of $\partial \mathbf{A}/\partial a_{lj}$ are zero, except for the element in the lth row and jth column which is equal to 1. Hence

$$\frac{\partial \lambda_i}{\partial a_{lj}} = w_{il} v_{ji} \tag{D.7}$$

Thus the sensitivity of the eigenvalue λ_i to the element a_{lj} of the state matrix is equal to the product of the left eigenvector element w_{il} and the right eigenvector element v_{ji}.

The *participation matrix* is defined as [65]

$$\mathbf{\Gamma} = [\boldsymbol{\gamma}_1 \;\; \boldsymbol{\gamma}_2 \;\; \cdots \;\; \boldsymbol{\gamma}_{n_x}] \tag{D.8}$$

with

$$\boldsymbol{\gamma}_i = \begin{bmatrix} \gamma_{1i} \\ \gamma_{2i} \\ \vdots \\ \gamma_{n_x i} \end{bmatrix} = \begin{bmatrix} v_{1i} w_{i1} \\ v_{2i} w_{i2} \\ \vdots \\ v_{n_x i} w_{i n_x} \end{bmatrix} \tag{D.9}$$

The element $\gamma_{ki} = v_{ki} w_{ik}$ is termed the *participation factor*. It is a measure of the relative participation of the kth state variable in the ith mode, and vice versa. The participation factor γ_{ki} is actually equal to the sensitivity of the eigenvalue λ_i to the diagonal element a_{kk} of the state matrix. Note that because normalized eigenvectors are used to obtain the participation matrix, the sum of the participation factors associated with any mode ($\sum_{i=1}^{n_x} \gamma_{ki}$) or with any state variable ($\sum_{k=1}^{n_x} \gamma_{ki}$) is equal to 1.